

# Ice growth processes in two bulk microphysics schemes compared to radar observations

Master's Thesis of

Markus Karrer

2nd of May 2018

at the Institute of Meteorology and Climate Research -  
Troposphere Research (IMK-TRO)

Reviewer: Prof. Dr. Corinna Hoose  
Second reviewer: Dr. Aiko Voigt



---

Ich versichere wahrheitsgemäß, die Arbeit selbstständig angefertigt, alle benutzten Hilfsmittel vollständig und genau angegeben und alles kenntlich gemacht zu haben, was aus Arbeiten anderer unverändert oder mit Änderungen entnommen wurde sowie die Satzung des KIT zur Sicherung guter wissenschaftlicher Praxis in der jeweils gültigen Fassung beachtet zu haben.

**Karlsruhe, den 2. Mai 2018**

.....  
(Markus Karrer)



# Abstract

Despite continuous progress in representing cloud microphysical processes in numerical models, cloud microphysics schemes remain a large source of uncertainty in weather and climate models. In this work, two bulk microphysics schemes are investigated, the Seifert and Beheng two-moment (SB) scheme and the recently developed predicted particle properties (P3) scheme. The work focuses on ice growth processes and highlights how these contribute significantly to the shortcomings of the two schemes. A cloud-resolving model is used to perform case studies of two days with synoptically driven cloud systems. To compare the schemes with cloud radar observations, a forward operator is used. This made it necessary to develop, test and apply a version of this forward operator adapted to the P3-scheme. In terms of the cloud structure, both schemes perform well. In contrast, there are larger mismatches between the forward-operated and the observed radar reflectivity, but no scheme is found to clearly outperform the other. In the two case studies, the SB-scheme has higher reflectivity values than the P3-scheme at heights a few kilometers above the cloud base. This deviation appears to result from the formulation of aggregation (adhesion of ice particles after collision). Both schemes miss to couple aggregation to the subgrid-scale turbulence, and use a temperature dependency that does not account for a maximum of the sticking efficiency at temperatures about  $-15^{\circ}\text{C}$ , which was found in previous studies. However, it is shown that an improved formulation of aggregation would lead to substantially improved precipitation forecast and that the treatment of supersaturation strongly impacts the precipitation field.

Furthermore, the potential of using the multiple radar frequencies to link fingerprints of growth processes, as seen in the forward operated reflectivity, with fingerprints of the same processes, as seen in observations, is analyzed. The continuous representation of riming processes in the P3-scheme could be used for the detection of these processes in the triple-frequency space, but the signatures of changes in the ice particle density do not match well with previous observational studies. Inaccurate assumptions in the microphysics scheme and the scattering calculations cause this disagreement. Pure ice-cloud processes, however, are distinguishable if the combined change of the dual-wavelength ratio and the reflectivity is analyzed. An increase in the mean size of the particle distribution can be caused by a decrease in the number concentration or an increase in the mass mixing ratio. The first is characterized by a slower increase of reflectivity with the dual wavelength ratio compared to the latter. In this way it is possible to separate, e.g., the depositional growth and aggregation by their forward operated reflectivity at two different frequencies. This analysis method promises to lead to new insights on ice growth processes and their representation in models.



# Zusammenfassung

Trotz anhaltendem Fortschritt in der Entwicklung von Mikrophysik-Schemata ist ein großer Anteil der Unsicherheit von numerischen Wettermodellen immer noch diesen zuzuschreiben. In dieser Arbeit werden die Defizite zweier Mikrophysik-Schemata untersucht und Eiswachstumsprozesse, die signifikant zu diesen Defiziten beitragen, hervorgehoben. Die untersuchten Schemata sind das Seifert und Beheng Zweimomentenschema (SB) und das kürzlich entwickelte "predicted particle properties" (P3) Schema. Ein wolkenauflösendes Modell wird benutzt, um Fallstudien zweier Tage durchzuführen. Um den Modelloutput mit Wolkenradaren zu vergleichen, wird ein Vorwärtsoperator verwendet, für den eine Adaption des P3-Schemas im Rahmen dieser Arbeit entwickelt, getestet und in den Fallstudien angewendet wird. Die Modellläufe mit beiden Schemata liefern gute Ergebnisse bezüglich der Wolkenstruktur, jedoch treten größere Unterschiede zwischen modellierter und beobachteter Reflektivität auf. Keines der beiden Schemata liefert eindeutig bessere Ergebnisse. In niedrigen Höhen treten mit dem SB-Schema höhere Reflektivitäten auf. Die Ursache dafür liegt vermutlich in der Implementierung der Aggregation: beide Schemata koppeln die Aggregation nicht an die subgridskalige Turbulenz und verwenden eine Parametrisierung der Hafteffizienz, die ein Maximum bei ungefähr  $-15\text{ °C}$  nicht berücksichtigt. Es wird weiterhin gezeigt, dass eine verbesserte Formulierung der Aggregation (Aneinanderhaften mehrerer Eiskristalle nach Kollision) zu einer wesentlichen Verbesserung der Niederschlagsvorhersage führen kann. Die Sättigungsadjustierung ist ein weiterer bedeutender Einflussfaktor auf das Niederschlagsfeld.

Weiterhin werden die Möglichkeiten analysiert, mit der kombinierten Analyse von mehreren Radarfrequenzen einzelne Wachstumsprozesse zu identifizieren und vergleichen. Dabei wird insbesondere untersucht, inwiefern die kontinuierliche Repräsentierung von Verreifungsprozessen im P3-Schema eine Detektion dieser Prozesse ermöglicht. Die Signaturen einer Veränderung der Dichte der Eispartikel stimmen allerdings schlecht mit den Ergebnissen früherer Studien überein. Für diese Diskrepanz sind unzutreffende Annahmen in sowohl dem Mikrophysik-Schema als auch den Streuberechnungen verantwortlich. Reine Eiswachstumsprozesse können jedoch durch eine kombinierte Analyse des "dual wavelength ratio" und einer Reflektivität unterschieden werden. Wachstumsprozesse können die mittlere Größe einer Partikelgrößenverteilung entweder durch eine Verringerung der Anzahlkonzentration oder einen Anstieg des Massenmischungsverhältnisses erhöhen. Bei ersterem weist die Signatur des Prozesses einen geringeren Anstieg der Reflektivität mit dem "dual wavelength ratio" auf als bei letzterem. In dieser Weise lässt sich im Signal der modellierten Reflektivitäten, z.B. das Depositionswachstum von der Aggregation unterscheiden. Dies legt nahe, dass die hier entwickelte Methode zu einem besseren Verständnis von Eiswachstumsprozessen und ihren Parametrisierungen in numerischen Modellen beitragen kann.



# Contents

<b>Abstract</b>	<b>iii</b>
<b>Zusammenfassung</b>	<b>v</b>
<b>1. Introduction</b>	<b>1</b>
<b>2. Theoretical Framework</b>	<b>5</b>
2.1. ICON-LEM . . . . .	5
2.1.1. Grid . . . . .	5
2.1.2. Prognostic equations . . . . .	6
2.1.3. Performance of the model in comparison with observations . . . . .	7
2.2. Hydrometeor size distribution in measurements and models . . . . .	8
2.3. Ice phase processes . . . . .	9
2.3.1. Ice nucleation/freezing . . . . .	9
2.3.2. Depositional growth/sublimation . . . . .	10
2.3.3. Aggregation . . . . .	11
2.3.4. Riming . . . . .	11
2.3.5. Differential sedimentation . . . . .	13
2.3.6. Relative importance and separation of microphysical processes . . . . .	13
2.4. Microphysics schemes . . . . .	14
2.4.1. Bulk microphysics schemes . . . . .	14
2.4.2. The Predicted Particle Properties (P3) scheme . . . . .	15
2.4.3. The Seifert and Beheng (SB) two-moment scheme . . . . .	22
2.4.4. Treatment of supersaturation . . . . .	24
2.5. Remote sensing of clouds by Radars . . . . .	24
2.5.1. Basics of radar meteorology . . . . .	25
2.5.2. Mie-scattering . . . . .	26
2.5.3. Rayleigh-scattering . . . . .	26
2.5.4. Self-Similar Rayleigh-Gans scattering . . . . .	26
2.5.5. Attenuation by gases and hydrometeors . . . . .	27
2.5.6. Passive and Active Microwave TRAnsfer model (PAMTRA) . . . . .	28
2.5.7. Multi-frequency analysis . . . . .	30
<b>3. Adaption of PAMTRA to P3</b>	<b>33</b>
<b>4. Case studies and model setup</b>	<b>37</b>
4.1. Case study 1: 26th April 2013 . . . . .	37
4.2. Case study 2: 24th November 2015 . . . . .	37
4.3. Domain . . . . .	38

4.4. Initialization and boundary data . . . . .	39
4.5. Overview of the model runs . . . . .	39
<b>5. Results and discussion</b>	<b>41</b>
5.1. Model-observation comparison in the time-height space . . . . .	41
5.1.1. 26th April 2013 . . . . .	41
5.1.2. 24th November 2015 . . . . .	49
5.2. Fall streaks . . . . .	55
5.3. Pure ice-cloud growth-processes in the November case . . . . .	57
5.4. Sensitivity runs concerning pure ice-cloud processes in the November case	59
5.5. Precipitation fields . . . . .	64
5.6. Using multi-frequency space to distinguish fingerprints of growth processes	71
5.6.1. Triple-frequency space . . . . .	71
5.6.2. $Z_e$ -DWR space . . . . .	74
<b>6. Conclusion/Outlook</b>	<b>81</b>
<b>Bibliography</b>	<b>85</b>
<b>A. Appendix</b>	<b>89</b>
A.1. PAMTRA input variables . . . . .	89
A.1.1. 24th November 2015 . . . . .	89
A.2. Inhomogeneities in the hydrometeor fields . . . . .	92
A.3. Contribution of the unrimed SB ice categories to $Z_e$ in the November case . . . . .	92
A.4. $v_{sed,Z}$ , $D_{mean}$ and DWR as a function of the normalized mixing ratio $q_{norm}$ . . . . .	93
A.5. List of Symbols and Acronyms . . . . .	94

# List of Figures

2.1.	Accumulated precipitation field of the 26th April 2013 from observations, ICON and COSMO model run on a domain covering the whole of Germany . . . . .	7
2.2.	Schematic overview of ice phase processes in mixed phase clouds. . .	10
2.3.	Sticking efficiency $E_i$ as implemented in the P3- or the SB-scheme . .	12
2.4.	Example of a size distribution of the ice category including different regions of mass-diameter relationship . . . . .	20
2.5.	Comparison of the size distribution shape of unrimed categories within the P3 and SB-scheme . . . . .	23
2.6.	Normalized backscattering cross section $\sigma_b$ for an ensemble of scatterer	28
2.7.	Flowchart of the forward operator PAMTRA . . . . .	29
2.8.	Schematic illustration of the regions of different particle types in the triple-frequency space . . . . .	31
4.1.	Corrected reflectance from MODIS on TERRA for the case studies. .	38
5.1.	Input variables to PAMTRA of the <i>April P3 control</i> run. . . . .	42
5.2.	Input variables to PAMTRA of the <i>April SB control</i> run. . . . .	43
5.3.	Time-height plot of observed and forward operated $Z_e$ (April case) . .	45
5.4.	CFADs of observed and forward operated $Z_e$ (April case) . . . . .	47
5.5.	Time-height plots of variables linked to hydrometeor velocity (April case)	48
5.6.	Time-height plot of observed and forward operated $Z_e$ (November case)	51
5.7.	CFADs of observed and forward operated $Z_e$ (November case) . . . . .	52
5.8.	Variables linked to hydrometeor velocity (November case) . . . . .	54
5.9.	Normalized mixing ratio ( $q_{norm}$ ) of the November case . . . . .	56
5.10.	Changes in $q_{norm}$ through different processes (November case) . . . . .	60
5.11.	$v_{sed,Z}$ of the P3 ice category in the <i>P3 control</i> run and different sensitivity runs (November case) . . . . .	61
5.12.	$v_{sed,Z}$ of the SB snow category of the <i>SB control</i> run and different sensitivity runs (November case) . . . . .	62
5.13.	Difference of CFADs of observed and forward operated $Z_e$ of the November case including sensitivity runs (10-16h) . . . . .	63
5.14.	Precipitation field from the RADOLAN dataset . . . . .	64
5.15.	Precipitation field of the <i>P3 control</i> run. . . . .	65
5.16.	Precipitation field of the <i>SB control</i> run . . . . .	66
5.17.	Precipitation field of the P3 sensitivity runs. . . . .	68
5.18.	Precipitation field of the SB sensitivity runs. . . . .	69
5.19.	Horizontal and vertical wind speed for different model runs and domains.	70

5.20. SB and P3 categories in the triple-frequency space . . . . .	74
5.21. Idealized analysis in the $Z_e$ -DWR space . . . . .	76
5.22. P3 November case in the $Z_e$ -DWR space . . . . .	79
5.23. Observations of the November case in the $Z_e$ -DWR space . . . . .	80
A.1. Input variables to PAMTRA of the <i>November P3 control</i> run. . . . .	89
A.2. Input variables to PAMTRA of the <i>November P3 satad</i> run. . . . .	90
A.3. Prognostic variables of the SB-scheme for the November case. . . . .	91
A.4. Vertical slice of the three-dimensional field of $q_i$ and $N_i$ of the <i>Nov. P3 control run</i> . . . . .	92
A.5. Contribution to $Z_e$ by the SB ice category and snow category . . . . .	92
A.6. Reflectivity weighted sedimentation velocity, mean diameter and dual-wavelength ratio as a function of the normalized mixing ratio . . . . .	93

# List of Tables

2.1. Terms in the basic equations of ICON . . . . .	6
2.2. Mass-diameter relationship parameter and thresholds in the size distribution of the P3-scheme . . . . .	18
2.3. Area-diameter relationship parameters in the P3-scheme . . . . .	18
2.4. List of ice phase process rates in the P3-scheme . . . . .	21
2.5. Size distribution and mass-diameter relationship parameters in the SB-scheme . . . . .	23
3.1. Sensitivity of the reflectivity and the dual wavelength ratio to prescribed parameters in different categories. . . . .	36
4.1. List of performed model runs . . . . .	40
5.1. Example of a fall streak calculation . . . . .	57
A.1. List of Symbols . . . . .	94
A.2. List of Acronyms . . . . .	97



# 1. Introduction

Microphysical processes in clouds remain one of the main sources of uncertainty in weather prediction and climate modeling (Boucher et al., 2013). Although there have been great advances in numerical models in the last decades (Bauer et al., 2015), the lack of knowledge of cloud microphysics processes and their representation in models still hampers larger predictive skills e.g. in regard to precipitation.

Outside the tropical ocean, precipitation is dominated by cold rain, which forms via processes involving the ice phase of water (Mülmenstädt et al., 2015). This highlights the importance of ice microphysical processes in regard to precipitation, which is not only crucial for the climate system as part of the hydrological cycle but also influences the lifetime and thereby the radiative effects of clouds. Processes involved in the growth of ice particles are of particular importance for the formation of precipitation as the size of the particles influences the sedimentation velocity (Lamb and Verlinde, 2011).

Radar measurements are widely used to study the formation of precipitation. Radars use different frequencies of the emitted beam and are operated both ground based (with a wide range of frequencies) and on satellites (e.g. in the upcoming Earth Clouds, Aerosols and Radiation Explorer (EarthCARE) mission; Illingworth et al., 2015), with higher frequencies compared to most of the ground based radars. The potential of radars in studying the formation of precipitation lies in the fact, that they can investigate cloud properties vertically resolved over the whole troposphere and are sensitive to large particles.

Microphysical processes in clouds have to be parameterized in each kind of numerical model. While numerical weather prediction (NWP) models have to parameterize also cloud-scale motions (due to their coarse horizontal grid), Large Eddy Simulations (LES) with a spatial resolution in the order of 100 m can resolve a significant part of the turbulence and thereby also cloud-scale motions at these scales (e.g. Heinze et al., 2016). Due to the computational costs of these high-resolution runs, LES can not be performed on a global scale, but are used to evaluate and improve climate and NWP models. Furthermore, the high degree of detail in the atmospheric dynamics, resolved by LES, eases the coupling between cloud-scale motions and microphysics schemes. Thus, analysis of microphysical processes are performed preferably with LES rather than NWP models.

The Seifert and Beheng two-moment (SB; Seifert and Beheng, 2006a) scheme simulates multiple processes in clouds and uses the traditional approach of partitioning the ice phase into four categories (cloud ice, snow, graupel and hail). Recently model

development paved the way to represent the ice phase in a more continuous way regarding riming processes in bulk schemes e.g. the predicted particle properties (P3) scheme (Milbrandt and Morrison, 2013; Morrison and Milbrandt, 2015) and using the superdroplet method (Brdar and Seifert, 2018). According to Morrison and Milbrandt (2015), this allows one to avoid the artificial conversions between different categories (e.g., snow and graupel) and to treat microphysics in a more physical manner. An additional advantage of the P3-scheme is the reduced computational cost, thanks to fewer prognostic variables in comparison to microphysics schemes with a similar degree of detail (e.g. the SB-scheme). The lower computation cost is especially important for climate models, and hence Dietlicher et al. (2018) implemented the P3-scheme into ECHAM (European Centre for Medium-Range Weather Forecasts - Hamburg; Roeckner et al., 2003).

While it is inherently difficult to compare the output of numerical models with observational measurements (e.g. cloud radars), forward operators are an important tool to provide a high degree of comparability. Forward operators such as the Passive and Active Microwave TRAnSfer model (PAMTRA; Maahn, 2015) can simulate e.g. radar moments or the full radar spectra and take also complex issues, like the scattering properties of large non-spherical particles at high frequencies into account (Tyynelä et al., 2011; Hogan and Westbrook, 2014).

Dual-frequency measurements have been used already by Matrosov (1992) to determine the parameters of the snow size distribution and achieve a more precise estimate of the snowfall rate. In recent years, this approach has been extended by the use of a third frequency. The resulting triple-frequency space has been explored by numerical studies (Leinonen et al., 2011; Kneifel et al., 2011) and observations (Kneifel et al., 2015). These studies found characteristic differences in the triple-frequency space between the different shapes and bulk densities of the hydrometeors. Growth processes like aggregation and riming change these properties of the hydrometeors and thereby their position in the triple-frequency space considerably. Thus a detection of these processes by the triple-frequency view is possible.

In this study, the ICOSahedral Nonhydrostatic model (ICON; Zängl et al., 2015) in its large eddy mode (ICON-LEM; Dipankar et al., 2015) is used to perform case studies on a circular domain with a diameter of up to 220 km and horizontal resolutions in the order of several 100 m. ICON-LEM is run with either the SB- or the P3-scheme and the model output is forward operated with PAMTRA, in order to evaluate the simulations against cloud radars. For this, an adaption of the P3-scheme to PAMTRA had to be developed in the course of this thesis. Rather than a comprehensive analysis, the target of this analysis is to spot deficiencies in the microphysics schemes and detect those processes that underlie the deficiencies. The focus therein lies on growth processes, due to their relevance for precipitation. Consequently, also the differences in the precipitation field, between the schemes and the impact of individual process formulations within the schemes on the precipitation field are studied.

---

Beyond the evaluation of the schemes, the potential of detecting fingerprints in the forward operated signal by using multi-frequency approaches is investigated. Detecting fingerprints in the forward operated signal of a model could foster synergy effects between LES and cloud radar observations and provide a future testbed for improving parametrizations of microphysical processes.

The chapters are organized as follows: Chapter 2 presents the underlying principles of atmospheric models, cloud physics and cloud radar observations and thereby lies a theoretical basis for the subsequent chapters. The adaption of PAMTRA to the P3-scheme is sketched in Chapter 3. The model setup is described in Chapter 4. The results of this work are discussed in Chapter 5. Finally, Chapter 6 provides the conclusion and outlook of this thesis.



## 2. Theoretical Framework

In the first part of this chapter the numerical model ICON in its large eddy version (ICON-LEM) is described. Section 2.3 gives an overview of microphysical processes in clouds which can be treated in multiple ways through microphysics schemes. In this study ICON-LEM is used with two different schemes. ICON-LEM is run with using either the SB-scheme or the P3-scheme as a microphysics scheme. Those schemes are described in Section 2.4. Furthermore, Section 2.5 discusses the basics of remote sensing of clouds by radars. At the end of the chapter the principles and capabilities of multi-frequency analysis are introduced.

### 2.1. ICON-LEM

In this study ICON-LEM was used to perform case studies of the past (so called hindcasts) with different setups in the microphysics schemes. There are different configurations of ICON. One of them is ICON numerical weather prediction mode (ICON-NWP) (Zängl et al., 2015) which is used for the weather forecast by the German Weather Service (DWD). These forecasts are performed on a relative coarse resolution. ICON-LEM is used in this study because it is designed for model runs with a high spatial resolution (down to 100 m grid spacing) which were performed during this study. ICON was developed in cooperation between the DWD and the Max Planck Institute for Meteorology (MPI-M), extended towards large eddy simulations (ICON-LEM; Dipankar et al., 2015) and evaluated against observations (Heinze et al., 2016) within the High Definition Clouds and Precipitation for advancing Climate Prediction (HD(CP)<sup>2</sup>) project.

ICON-LEM (and other LEMs) is able to resolve cloud-scale motions, which is a big advancement over general circulation models like ICON-NWP. LEM simulations are more computationally expensive than NWP simulations and therefore usually limited to small domains. Nevertheless, simulations on a domain covering the whole of Germany have recently been performed (Heinze et al., 2016).

In this section, the grids (Section 2.1.1), the governing equations (Section 2.1.2) and the performance (Section 2.1.3) of ICON-LEM is discussed.

#### 2.1.1. Grid

ICON uses an unstructured triangular grid. The global grid of ICON is derived from a convex icosahedron. As a result, the earth is approximated by 20 equal sized triangular cells without grid refinement. By successive refinement of the global grid finer grids can be generated. Triangular grids have an advantage over latitude-longitude grids

Table 2.1.: Terms in the basic equations of ICON (see Equations 2.1 - 2.4)

symbol	description
$\Pi$	Exner function
$\zeta$	vertical vorticity component
$c_{pd}$	specific heat capacity of dry air at constant pressure
$c_{vd}$	specific heat capacity of dry air at constant volume
$f$	Coriolis parameter
$F(v_n)$	source term for horizontal momentum
$g$	gravitational acceleration
$K_h$	horizontal part of the kinetic energy
$Q$	diabatic heat source terms
$R_d$	gas constant of dry air
$v_t$	horizontal wind speed tangential to the triangle edge

which results from the fact that there is no convergence of meridians towards the poles. As a result, polar filtering is not necessary which must be used in regular latitude-longitude grids to overcome time step restrictions (Zängl et al., 2015).

Considering vertical discretization ICON uses Smooth LEvel VERTICAL (SLEVE) coordinates in the form described in Leuenberger et al. (2010). This approach is applicable to nonhydrostatic models and takes the topography into account.

### 2.1.2. Prognostic equations

The basic equations which underlie all configurations of the model (e.g. ICON-LEM) can be found in Zängl et al. (2015) and are quoted here:

$$\frac{\partial v_n}{\partial t} + \frac{\partial K_h}{\partial n} + (\zeta + f) v_t + w \frac{\partial v_n}{\partial z} = -c_{pd} \Theta_v \frac{\partial \pi}{\partial n} + F(v_n) \quad (2.1)$$

$$\frac{\partial w}{\partial t} + v_h \cdot \nabla w + w \frac{\partial w}{\partial z} = -c_{pd} \Theta_v \frac{\partial \pi}{\partial n} - g \quad (2.2)$$

$$\frac{\partial \rho}{\partial t} + \nabla \cdot (v \rho) = 0 \quad (2.3)$$

$$\frac{\partial(\rho \Theta_v)}{\partial t} + \nabla \cdot (v \rho \Theta_v) = Q \quad (2.4)$$

Equations 2.1 to 2.4 constitute the dynamical core of the model. Through these equations the temporal evolution of the prognostic variables are defined. The prognostic variables are the horizontal wind speed  $v_n$  normal to the triangle edge, the vertical wind speed  $w$ , the air density  $\rho$  and the potential temperature  $\Theta_v$ . Other terms occurring in the Equations 2.1 - 2.4 are listed in Table 2.1. The source (and loss) rates  $S$  of additional prognostic variables are treated within the physics schemes (e.g. certain moments of the particle size distribution). As described in Equation 2.5

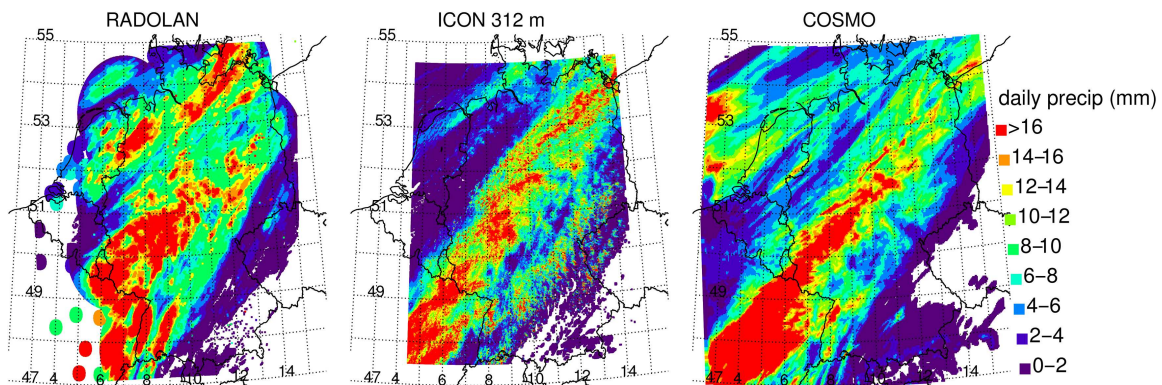


Figure 2.1.: Accumulated precipitation field of the 26th April 2013 from observations, ICON (312 m spatial resolution) and COSMO (2.8 km spatial resolution) model runs on a domain covering the whole of Germany (taken from Heinze et al. (2016))

these variables  $x_i$  also underlie three-dimensional advection.

$$\frac{\partial x_i}{\partial t} + \nabla \cdot (v x_i) = S \quad (2.5)$$

In the LEM version of ICON additionally a three dimensional turbulence scheme is implemented (Dipankar et al., 2015). Furthermore, several parametrizations used in ICON-NWP are not necessary (or not valid) in the application area of ICON-LEM high-resolution runs and are either turned off or replaced.

### 2.1.3. Performance of the model in comparison with observations

In Heinze et al. (2016) comparisons between model and observations have been made on the basis of four simulated days in spring 2013. This investigation relies on both ground based measurements and satellite retrievals. This study has, amongst other objectives, also the target to compare ICON-LEM and its microphysics schemes with observations. In that sense, this study follows up on parts of the analysis of Heinze et al. (2016), which is the reason why the relevant findings of Heinze et al. (2016) are summarized in the following.

Heinze et al. (2016) stated that the performance of ICON-LEM is nearly as good as the performance of the Consortium for Small-scale Modeling (COSMO) model in most aspects of weather prediction (see e.g. the precipitation field in Figure 2.1). This is a high benchmark, because COSMO is well established and widely used for weather prediction in Europe. Nevertheless, the evaluation of ICON-LEM reveals significant deviations of the model from observations. Here, only the biases concerning precipitation and the hydrometeor distribution in the time-height space are summarized. These are of special importance because this study further investigates these properties by the use of an alternative microphysics scheme (the P3-scheme) and an additional case study (see Chapter 4).

In order to estimate the performance of ICON-LEM concerning the prediction of precipitation, Heinze et al. (2016) investigated both the geographical distribution of hydrometeors and precipitation and the hydrometeor distribution in the time-height space. They found that ICON-LEM underestimates the frequency of occurrence of low-intensity rain while it overestimates the frequency of occurrence of high-intensity rain events. The Intensity Scale skill score (Casati et al., 2004) enables one to analyze the skill of predicting the precipitation field as a function of precipitation rate and spatial scale of the error. Using this skill score, Heinze et al. (2016) found the first positive skill score for intense precipitation above  $32 \text{ mm day}^{-1}$  at a spatial scale of 19.2 km for the accumulated precipitation field of the 24th April 2013 (see also Figure 2.1). A positive skill score at a certain spatial scale implies that the forecast predicts the precipitation better (when coarse grained to the resolution of this spatial scale) than a random forecast. As a result, ICON is not capable of predicting intense precipitation correctly at these small spatial scales. However, higher skill scores are found at lower intensities and larger spatial scales.

In order to investigate the hydrometeor distribution in the time-height space they used the forward operator Efficient Modular Volume RADar Operator (EMVORADO; Zeng et al., 2016) for comparison with a polarimetric scanning X-Band radar and PAMTRA for comparison with a vertically pointing Ka-Band Radar. The comparison of the forward operated differential reflectivity ( $ZDR$ ) with the scanning radar suggests an overestimation of the rain drop size. The comparison of the forward operated reflectivity with the vertically pointing radar shows an overestimation of up to 10 dB.

Overall they concluded that there is potential to revise the microphysics scheme in some aspects of the ice phase.

## 2.2. Hydrometeor size distribution in measurements and models

The assumptions about hydrometeor size distributions have an important impact on both, processes simulated in bulk microphysics schemes and forward operated quantities and are therefore of great interest for this study. Most of the size distributions used in cloud microphysics schemes can be described by the modified gamma distribution (see Equation 2.6) or its simplifications (Petty and Huang, 2011).

$$N(D) = N_0 D^\mu \exp(-\lambda D^\gamma) \quad (2.6)$$

The parameters of this modified gamma distribution are the intercept parameter  $N_0$ , the slope parameter  $\lambda$ , the shape parameter  $\mu$  and the broadness parameter  $\gamma$ .  $D$  represents the maximum particle dimension and  $N(D)$  the number concentration of particles of size  $D$ . Setting  $\gamma = 1$  leads to a three-parameter gamma distribution and setting  $\gamma = 1$  and  $\mu = 0$  to an exponential distribution. Examples for the full four-parameter gamma distributions (as used in the SB-scheme) and three-parameter gamma distribution (as used in the SB-scheme) are depicted in the Figures 2.4 and 2.5. Petty and Huang (2011) stated that the exponential and the three-parameter

gamma distributions are mostly used in cloud models, while the four-parameter gamma distribution is mostly used for haze, fog and cloud droplet. Milbrandt and Yau (2005) emphasized the importance of  $\mu$  for the rate of size sorting of precipitating particles and instantaneous growth rates.

Brandes et al. (2007) showed by the use of video-distrometers that for precipitating particles an empirical relationship between  $\mu$  and  $\lambda$  can be found. As a result, the strong assumption of a fixed  $\mu$  for a given particle category might not be necessary in a two-moment-scheme. Analyzing spiral descents Heymsfield (2003) came to a similar conclusion as Brandes et al. (2007). The  $\mu$ - $\lambda$  relationship from this study is used in the P3-scheme (see Section 2.4.2.3). Later Heymsfield et al. (2013) fitted the size distribution of ice cloud particles measured in-situ by aircraft flights and found nearly exponential distributions.

## 2.3. Ice phase processes

Before we are able to discuss the treatment of cloud microphysical processes by bulk schemes in Section 2.4, the selected microphysical processes themselves are summarized in this section (Figure 2.2 provides a schematic overview over these processes). The selection is based on the importance of the processes in pure ice and mixed phase stratiform clouds, which can lead to the formation of precipitation. Initially ice particles form through various nucleation or freezing processes (see Section 2.3.1) near the cloud top. Subsequently, the ice particles grow in the absence of liquid hydrometeors through depositional growth (see Section 2.3.2) and aggregation and in the presence of liquid hydrometeor through riming (see Section 2.3.4). These growth processes are crucial for the formation of precipitation because they lead to considerable higher sedimentation velocities.

### 2.3.1. Ice nucleation/freezing

The formation of ice phase either from the vapor or the liquid phase requires to overcome the barrier of the Gibbs free energy  $\Delta G$ . As a result, water droplets do not freeze instantaneously at 0 °C but at temperatures of about -38 °C in the absence of aerosols. If aerosols are absent, also deposition nucleation (phase transition from vapor to ice) requires large supersaturation which is not present in the atmosphere. Aerosols which make freezing of liquid hydrometeors at temperatures above -38 °C and deposition nucleation possible are called ice nuclei (IN).

Hoose and Möhler (2012) reviewed multiple laboratory experiments and identified temperature-supersaturation regions where ice nucleation via different IN-types and freezing mechanisms are observed. Possible freezing mechanisms are contact freezing (freezing resulting from the collision of a water droplet and an IN), immersion freezing (freezing of a droplet with an immersed IN), condensation freezing (subsequent freezing of water which condenses at the IN at temperatures below 0 °C) and deposition nucleation (phase transition of vapor to ice at the surface of an IN).

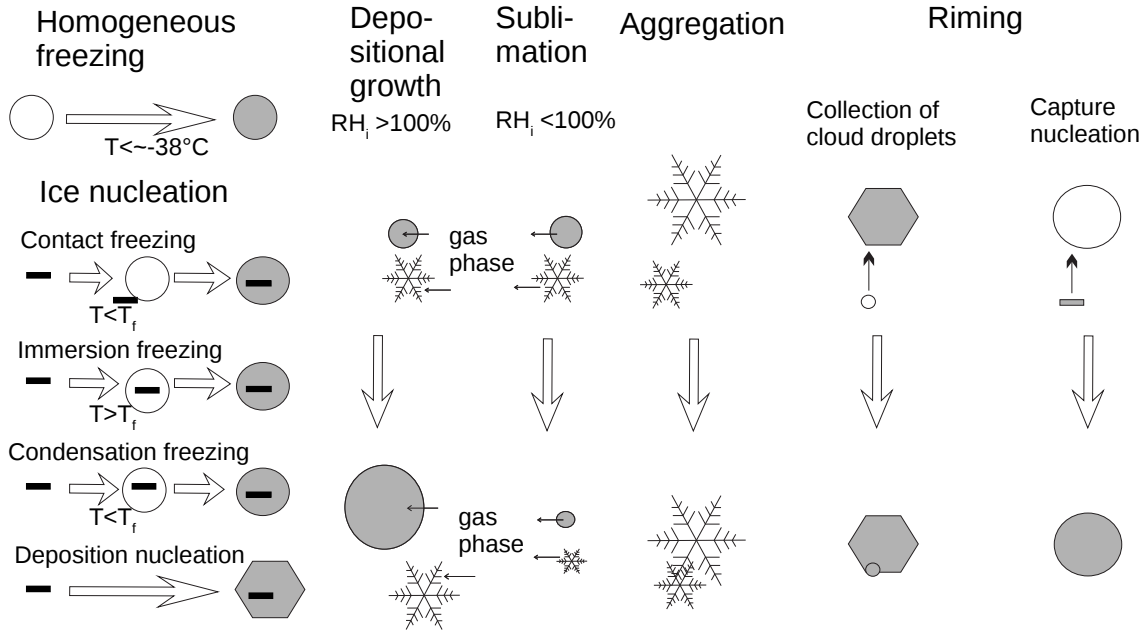


Figure 2.2.: Schematic overview of ice phase processes in mixed phase clouds. Particles with a white and grey facecolor represent liquid hydrometeors and ice phase hydrometeors, respectively. Aerosols are indicated by black rectangles.  $T_f$  stands for the freezing temperature (partially adapted from Lamb and Verlinde (2011)).

### 2.3.2. Depositional growth/sublimation

Depositional growth occurs when the flux of the water vapor towards the ice particle is positive. This positive flux occurs if the relative humidity over ice  $RH_i$  is larger than 100%. In case of  $RH_i < 100\%$  the ice particles sublime.

The rate by which the mass of an individual particle  $m$  changes by depositional growth or sublimation is given by Equation 2.7:

$$\left(\frac{dm}{dt}\right)_{depos,sublim} = 4\pi C(D) \rho_i G_i s_i \quad (2.7)$$

Where  $s_i$  is the supersaturation over ice defined as  $s_i = ((RH_i - 100\%)/100\%)$ ,  $C$  the capacitance of the ice particle, which is proportional to the size  $D$  of the ice particle but is also related to its shape.  $G_i$  is a factor depending on the air temperature  $T$  and other atmospheric and thermodynamic values as described in Equation 8.41 in Lamb and Verlinde (2011).

If the ice particles get large enough, aggregation is more likely to happen. As a result, depositional growth and aggregation (which is discussed in the next section) are strongly linked and often occur simultaneously.

### 2.3.3. Aggregation

The term aggregation describes the adhesion of two or more ice particles after collision leading to one bigger particle (thereafter called aggregate). To calculate rates of aggregation, usually the stochastic collection equation (SCE) (see Equation 2.8, formulated with the size distribution  $f(m)$  as a function of the masses of the colliding particles  $m$  and  $m'$ ) with the use of collection kernels  $K(i, j)$  are solved (Pruppacher et al., 1998). One of the most intuitive formulations is given by Equation 2.9, the sweep-out kernel. It can be derived from the swept out volume of a particle pair. The swept out volume - and thereby the collection kernel - is bigger for a larger difference of the sedimentation velocities  $\Delta v_{sed} = |v_i - v_j|$  of the colliding particles and bigger diameter of the particles ( $D_i$  and  $D_j$ ). Both the collision efficiency  $E_c$  and the sticking efficiency  $E_s$  modify the aggregation kernel. The first one considers that not all of the particles within the swept volume or even particles outside the swept volume collide, the latter takes into account that not all colliding particles stick together. Both parameters can be derived experimentally or by fluid-dynamic calculations.

$$\left(\frac{df(m)}{dt}\right)_{coll} = \int_0^{m/2} f(m') f(m - m') K(i, j) dm' - \int_0^\infty f(m) f(m') K(i, j) dm' \quad (2.8)$$

$$K(i, j) = \frac{\pi}{4} (D_i + D_j)^2 |v_{sed,i} - v_{sed,j}| E_c E_s \quad (2.9)$$

In bulk schemes the change of the prognostic variables are calculated either by numeric integration over the size spectra (as done in the P3-scheme) or by parametrizations based on the SCE using mean properties of the distribution (as done in the SB-scheme). This different treatment of aggregation leads to significant differences in the forward operated  $Z_e$  as shown later.

The observations of Hobbs et al. (1974) reveal a maximum of  $D_{mean}$  near  $-15^\circ\text{C}$  where aggregation of dendrites is assumed to be efficient by the so called interlocking mechanism (Lamb and Verlinde, 2011) which increases  $E_s$ . Both the SB-scheme and the P3-scheme have rather simple approaches of  $E_s$  implemented (see Figure 2.3) which do not account for a maximum of  $E_s$  near  $-15^\circ\text{C}$ .  $E_s$  is also strongly enhanced near the melting temperature (which is considered in both implementations of  $E_s$  used within the SB- or the P3-scheme). This enhancement results from less tight bonds between the molecules of the ice particle (quasi-liquid layer) which increases the probability of bonding with molecules of another ice particle (Lamb and Verlinde, 2011).

Lamb and Verlinde (2011) stated that aggregation enhances precipitation through two pathways. Directly through the increase of sedimentation velocity and indirectly through enhancing the riming efficiency. Riming is considered in the next section.

### 2.3.4. Riming

Like aggregation, riming describes a collection process. During the process of riming, liquid hydrometeors collide with ice particles and freeze instantaneously if the temperature at the ice particle surface is lower than  $0^\circ\text{C}$ . Particles which form through riming

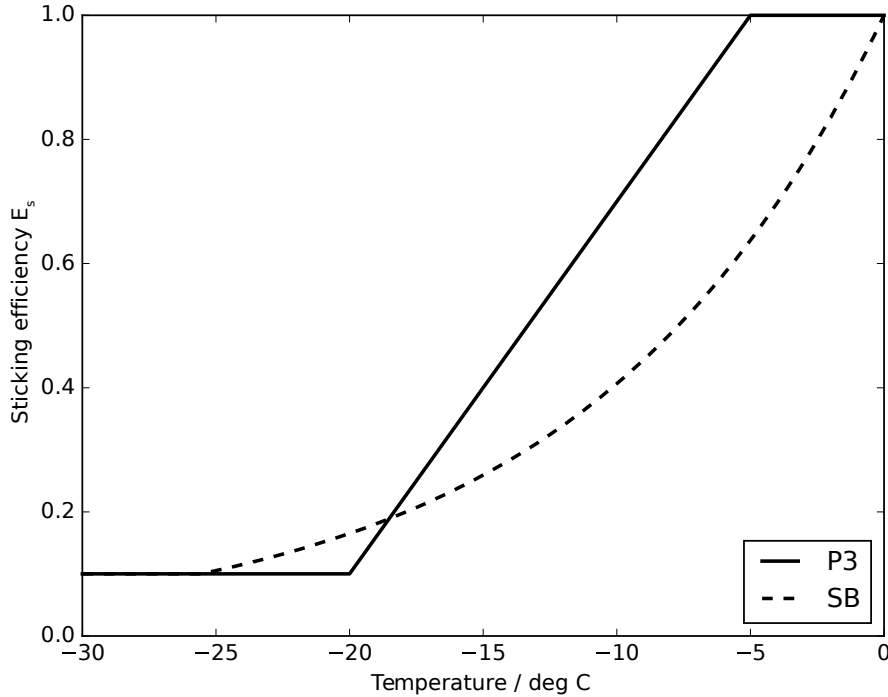


Figure 2.3.: Sticking efficiency as implemented in the P3-(solid line) and the SB-scheme (dashed line).

are often called graupel or hail. As is the case with the calculation of aggregation rates, the SCE has to be solved to retrieve the riming rates.

Because cloud droplets and rain drops have distinct characteristics there are often two different formulations used for the collision of ice particles with cloud droplets or rain drops.

Due to the low sedimentation velocity of cloud droplets (with the liquid water content  $LWC$ ) the continuous collection (see Equation 2.10) is a good approximation for the collection of cloud droplets by ice particles.

$$\left(\frac{dm}{dt}\right)_{coll,ice-droplet} = K(i, j) LWC \quad (2.10)$$

The collection kernel  $K(i, j)$  is similar to the one defined in Equation 2.9 with the difference that the sticking efficiency can be neglected, because the probability of sticking of the droplets at the ice particle surface is close to 1. The density of the rime which forms the ice particle is highly variable between  $\sim 100\text{kg m}^{-3}$  at low temperatures and  $\sim 600\text{kg m}^{-3}$  near the melting temperature (Cober and List, 1993).

If the liquid hydrometeor is large compared to the ice particle (usually this is valid for rain drops) the riming process is also called capture nucleation. In this case the liquid hydrometeor has the larger sedimentation velocity and therefore captures the smaller ice particle. This leads to an immediate freezing of the rain drop and a large

almost-spherical ice particle with high rime density (close to the density of bulk ice) forms.

Both the collection of small droplets and raindrops depend essentially on the shape and the size of the ice crystal.

Riming can lead to a rapid increase of the mass of an ice particle while the increase of projected area is minor. This can lead to high sedimentation velocities and the occurrence of frozen particles at the ground even with the existence of a thicker layer of air with  $T > 0^\circ\text{C}$  (Lamb and Verlinde, 2011).

### 2.3.5. Differential sedimentation

Sedimentation is not only of importance for precipitation and collection processes as described in the previous sections, it can also change the shape of the size distribution by differential sedimentation.

Kumjian and Ryzhkov (2012) describe differential sedimentation as the result of heavier (larger) particles that fall faster than lighter (smaller) particles. Differential sedimentation is a transient process given a homogeneous wind field. In the presence of local updrafts and vertical wind shear differential sedimentation can be maintained over a longer time range. Updrafts lift the smaller particles while larger particles can still sedimentate.

Differential sedimentation manifests itself in a two-moment scheme as the difference between the mean number-weighted sedimentation velocity  $v_{sed,N}$  and the mean mass weighted sedimentation velocity  $v_{sed,q}$ . In general the  $k$ -th moment weighted sedimentation velocity  $v_{sed,k}$  is given by:

$$v_{sed,k} = \frac{\int_0^\infty v_{part}(D) N(D) D^k dD}{\int_0^\infty N(D) D^k dD} \quad (2.11)$$

where  $v_{part}(D)$  is the sedimentation velocity of an individual particle at a given diameter  $D$  and  $N(D)$  is the size distribution. While one-moment schemes can not simulate differential sedimentation, two-moment schemes tend to overestimate this effect compared to bin schemes (see Khain et al. (2015) and references therein).

### 2.3.6. Relative importance and separation of microphysical processes

Lamb and Verlinde (2011) described the relative importance of growth processes in stratiform clouds. According to this, deposition growth is dominant in the upper part of the cloud. At lower levels, aggregation becomes more effective because the ice particles have grown larger and  $E_s$  increases with increasing temperatures. Riming is also more likely to happen in the lower part of the cloud where the temperature is higher and the presence of supercooled droplets more likely.

An approach to further investigate the relative importance of growth processes by radar observations was proposed by Kalesse et al. (2013). They combined investigations of the relationship between the reflectivity  $Z_e$  and the Doppler velocity  $v_{Doppler}$  with microphysical relations of bulk properties in order to detect the dominant growth

mechanisms. Because it is possible to diagnose the occurrence of processes in the model runs or turn of each of the processes individually, in this study the simultaneous appearance of certain microphysical processes and signatures in forward operated observables can be analyzed. In this way the potential of further investigations of the relative importance of growth processes can be tested (see Section 5.6).

## 2.4. Microphysics schemes

One of the most important components of large eddy models like ICON-LEM (which is described in Section 2.1) are the microphysics schemes. Basics of bulk microphysics schemes and conceptual differences of the two microphysics schemes, used in this study, are discussed in this section.

LEM simulations are able to resolve many of the relevant processes in clouds. For example convection does not have to be parameterized. Nevertheless, microphysical processes in clouds occur on much smaller scales than the grid of a LEM simulation. As a result, several approaches have been made to represent cloud microphysics. These are bulk microphysics schemes (in the following bulk schemes), spectral bin microphysics schemes (in the following bin schemes) and Lagrangian cloud models (Khain et al., 2015).

### 2.4.1. Bulk microphysics schemes

Both schemes used in this study (the P3-scheme and the SB-scheme) are bulk schemes. Therefore, a short introduction of bulk schemes is given in the following.

Bulk schemes are usually categorized by the number of moments (see Equation 2.12) they predict.

$$M(k) = \int_0^{\infty} D^k f(D) dD \quad (2.12)$$

Here the size distribution  $f$  is described as a function of the diameter  $D$ .

The moments  $M(k)$  are predicted for a limited number of hydrometeor categories. The more moments and the more hydrometeor categories that are predicted, the more computationally expensive the scheme is. As a result, models with less complexity like climate models often have to rely on single-moment schemes with one or two predicted categories for the ice phase (Dietlicher et al., 2018).

While two-moment-schemes (which predict e.g. the number concentration  $N$  and the mass mixing ratio  $q$ ) have great advantages over single-moment schemes in representing microphysical processes because the size distribution can vary in time and space, they still rely on vast simplifications. Firstly, the shape of the size distribution must always be described by an analytic distribution (mostly the gamma-distribution is chosen). Khain et al. (2015) stated that diffusional growth, sedimentation, melting, and freezing lead to deviations from a gamma-shaped distribution. Secondly, for a correct representation of the impact of a certain process on the size distribution, as many predicted moments as parameters are needed. In other words, the fixing or linking of size distribution parameters, as we will see it in Section 2.4.2 for the P3-scheme as

well as in Section 2.4.3 for the SB-scheme, is hampering the correct representation of an individual process (Khain et al., 2015) and therefore the comparison of the forward operated signal and the actual measurements.

### 2.4.2. The Predicted Particle Properties (P3) scheme

The Predicted Particle Properties (P3; Morrison and Milbrandt, 2015) scheme is a bulk microphysics scheme that represents a new concept for the parametrization of ice-phase microphysics. In contrast to other common two-moment microphysics schemes (e.g. the Seifert-Beheng scheme, see Section 2.4.3), the P3-scheme uses only one ice category, described by four prognostic variables. The P3-scheme is not a classical two-moment-scheme because it also predicts variables which are not moments of the size distribution. A similar approach was already suggested by Morrison and Grabowski (2008). With those variables - the mass mixing ratio of the ice category  $q_i$ , the rime mass mixing ratio  $q_{rim}$ , the bulk rime volume  $B_{rim}$  and the number concentration of the ice category  $N_i$ , a variety of ice species can be represented. The main advantage of the P3-scheme is the avoidance of conversion between different categories. Classical two-moment schemes show a large sensitivity to how ice is partitioned into the different categories. For example the assignment of particles into the hail category instead of the graupel category can result in a significantly different storm structure and precipitation field (Milbrandt et al., 2015).

The above mentioned prognostic variables ( $q_i$ ,  $q_{rim}$ ,  $B_{rim}$ ,  $N_i$ ) are chosen in a way that they can track particle evolution through different ice growth processes. Processes which are not considered to produce rimed mass increase only  $q_i$ . In contrast, processes that are considered to produce rimed mass increases  $q_{rim}$  and thereby  $q_i$  (which is a sum of  $q_{rim}$  and the unrimed part of  $q_i$ ). Additionally  $\rho_{rim}$  ( $q_{rim}$  divided by  $B_{rim}$ ) tracks the conditions where riming occurs in respect to the density of newly created rime mass.

In Milbrandt and Morrison (2016) the concept of the P3-scheme has been extended by introducing a multicategory version which is not implemented into ICON yet. Each of these categories has no prescribed microphysical properties and is therefore a free category. The multicategory P3 version allows multi-modal ice distributions which is a prerequisite for representing microphysical processes which generate particles with a separate mode, e.g. the Hallet-Mossop-process (Mossop, 1976).

In contrary to the ice-phase microphysics, warm cloud processes are handled in a similar way to other two-moment schemes. There are two categories, one for cloud water and one for rain droplets. The number concentrations ( $N_c$  and  $N_r$ ) and the mass mixing ratios ( $q_c$  and  $q_r$ ) of these warm phase categories are prognostic variables of the P3-scheme. The reason for the separation of the warm phase into two categories is the bi-modality of the liquid hydrometeors. One of the modes is composed by cloud droplets the other by rain drops (Lamb and Verlinde, 2011).

Only eight prognostic variables have to be calculated in each timestep for the P3-scheme. This is an advantage concerning computational time over other schemes with a comparable complexity of representing cloud microphysics. For example the

version of the SB-scheme used in this study (described in Section 2.4.3) needs to solve ten equations (two for each hydrometeor category) at each timestep.

### 2.4.2.1. Mass-diameter relationship

With the help of the mass-diameter ( $m$ - $D$ ) relationship the mass of an individual particle can be converted to its diameter or vice versa. This is often needed in microphysics schemes e.g. when process rates are calculated which depend on the diameter, which is not a prognostic variable of the scheme. The  $m$ - $D$  relationship is also one of the main input for the scattering calculation as we will see in Chapter 3 and an important connection between  $q$  and  $N$ . A summary of all parameters describing the full  $m$ - $D$  relationship is shown in Table 2.2. In the following we will examine the assumptions leading to those parameters.

For liquid particles, the  $m$ - $D$  relationship is constant over the whole range of diameters and given by Equation 2.13.

$$m = a D^b = \frac{\pi}{6} \rho_w D^3 \quad (2.13)$$

Where  $m$  is the mass of an individual particle,  $\rho_w$  the density of water and  $D$  the maximum diameter of the particle. This approximation is justified because cloud droplets and rain drops can be approximated by spheres and the density of water lies - compared to the density of ice particles - in a relatively small range under atmospheric conditions (around  $\rho_w = 997 \text{ kg m}^{-3}$ ).

For the ice phase, the  $m$ - $D$  relationship is divided in four different sections across the range of particle sizes separated by critical diameters (see rightmost column in Table 2.2 and Figure 2.4). All of these thresholds provide consistency such that the  $m$ - $D$  relationship is continuous over the whole size distribution.

In the first section at the lower edge of the size distribution small dense spherical ice are represented. This section reaches from the lowest occurring particles up to a critical diameter  $D_{th}$ . From  $D_{th}$  to  $D_{cr}$  the particles are assumed to be dense nonspherical ice. The particles between  $D_{cr}$  and  $D_{gr}$  are represented by graupel. If there are no rimed particles (which is equivalent to  $F_{rim} = 0$ ),  $D_{cr}$  and  $D_{gr}$  are set to infinity. If  $F_{rim}$  is neither zero nor one, the section of the size distribution with the largest particle with  $D > D_{gr}$  are assumed to be partially rimed.

The thresholds separating these sections of different  $m$ - $D$  relationship mentioned in the previous paragraph as well as the coefficients of the  $m$ - $D$  relationship itself depend on the prognostic variables, as described in the following and summarized in Table 2.2. Although some of the variables (e.g.  $\rho_{rim}$  or  $F_{rim}$ ) determining the  $m$ - $D$  relationship coefficients are not prognostic variables themselves, they can be derived directly from the four prognostic variables ( $F_{rim}$  is defined as  $q_{rim}$  divided by the sum of  $q_i$  and  $q_{rim}$ ). Small ice particles are treated similarly to liquid particles with the same relationship as in Equation 2.13 but with a bulk ice density of  $\rho_i = 916 \text{ kg m}^{-3}$ . This assumption is valid because small particles have an almost spherical shape. However, this is not the case for larger particles. Due to their nonspherical shape, larger particle are

distinguishable from smaller particles in their effective density. The  $m$ - $D$  relationship is defined by the following power law expression:

$$m_{va} = a D^b = a_{va} D^{b_{va}} \quad (2.14)$$

Thereby  $a_{va}$  and  $b_{va}$  are the coefficients in the  $m$ - $D$  relationship for large unrimed ice. It should be noted that  $a_{va}$  and  $b_{va}$  are constant and do not depend on the growth history of the particle ensemble. In particular these coefficients do not vary according to the main growth mechanisms (like depositional growth or aggregation). Ensembles of aggregates are often described with a lower exponent in the  $m$ - $D$  relationship than ensembles of pristine crystals.

If the rime mixing ratio  $q_{rim}$  is larger than zero, the larger particles of the size distribution represent rimed or partially rimed particles (red and purple part in Figure 2.4). For completely infilled crystals (red part in Figure 2.4), which are also referred to as graupel, we can assume a spherical shape (exponent of 3 in the power law). After deriving the density of graupel  $\rho_g$  iteratively (see Equation 2.17) the  $m$ - $D$  relationship for graupel can be stated as:

$$m_g = a D^b = \frac{\pi}{6} \rho_g D^3 \quad (2.15)$$

Due to the concept of in-filling proposed by Heymsfield (1982) - which is used in the P3-scheme - small particles fill in with rime at smaller values of  $F_{rim}$ . Therefore larger particles are not completely filled with rime and thus a  $m$ - $D$  relationship that differs from the one used for the graupel particles is required (particularly the not completely infilled particles are not spherical).

$$m_r = a D^b = \left( \frac{1}{1 - F_{rim}} \right) a_{va} D^{b_{va}} \quad (2.16)$$

Equation 2.16 can be derived with the assumption that prior to the complete infilling of the particles  $F_{rim}$  is equal to the rime mass fraction of the individual particle. According to the concept of infilling from Heymsfield (1982) - which is used here - the diameter  $D$  of the particle does not change during the process of riming. Approaching the threshold between partially rimed ice and graupel the particles are getting heavily rimed. This has implications on the radiative scattering calculations which are discussed in Section 2.5.

Calculating an average of  $\rho_{rim}$  with the density of the unrimed part of the particle  $\rho_d$  weighted with  $F_{rim}$  we can derive Equation 2.17 for the graupel density  $\rho_g$ . In this way the evolution of rime growth is represented.

$$\begin{aligned} \rho_g &= \rho_{rim} F_{rim} + (1 - F_{rim}) \rho_d \\ \rho_d &= \frac{6 a_{va} (D_{cr}^{b_{va}-2} - D_{gr}^{b_{va}-2})}{\pi (b_{va} - 2) (D_{cr} - D_{gr})} \end{aligned} \quad (2.17)$$

The density of the unrimed part of the particle  $\rho_d$  is calculated as a mass weighted average over the dense nonspherical particles (green part of the size distribution in Figure 2.4) divided by the exponents.

Table 2.2.:  $m$ - $D$  relationship parameter ( $m = a D^b$ ) and thresholds in the size distribution of the P3-scheme

"particle name"	$a$	$b$	upper threshold
spherical ice	$\frac{\pi}{6}\rho_i (= 900)$	$b_{spher} = 3$	$D_{th} = \left(\frac{\pi\rho_i}{6a_{va}}\right)^{1/(b_{va}-3)} \approx 6.71 \cdot 10^{-5}m$
dense non-spherical ice	$a_{va} = 0.0121$	$b_{va} = 1.9$	$D_{cr} = \left(\frac{1}{1-F_{rim}} \frac{6a_{va}}{\pi\rho_g}\right)^{1/(3-b_{va})}$
graupel	$\frac{\pi}{6}\rho_g$	$b_{spher} = 3$	$D_{gr} = \left(\frac{6a_{va}}{\pi\rho_g}\right)^{1/(3-b_{va})}$
partially rimed ice	$\frac{1}{1-F_{rim}}a_{va}$	$b_{va} = 1.9$	

#### 2.4.2.2. Projected Area-Diameter ( $A$ - $D$ ) relationship

The projected area of a particle  $A$  is the projection of its shape to a horizontally orientated plane. The relationship between the projected area and the diameter ( $A$ - $D$  relationship) is used when deriving the sedimentation velocity of individual particles and the whole distribution. In the latter case, a weighting with a specified property such as the number concentration, mass or reflectivity is necessary (see also Section 2.3.5).

For spherical particles, the  $A$ - $D$  relationship is simply given by the  $A$ - $D$  relationship of spheres:

$$A = a D^\beta = \frac{\pi D^2}{4} \quad (2.18)$$

In this scheme, all hydrometeor categories representing liquid particles as well as the ice particles in specific regions of diameter are assumed to be spherical. These include spherical ice below  $D_{th}$  and graupel between  $D_{gr}$  and  $D_{cr}$ .

For the dense nonspherical ice particles both parameter in the  $A$ - $D$  relationship are taken from an empirical study by Mitchell (1996). For the partially rimed ice particles also the empirical  $\beta$ -parameter for the dense nonspherical ice particles is taken.  $\alpha$  is calculated by linear weighting between the values of graupel and dense nonspherical ice with the mass. The parameter of the  $A$ - $D$  relationship can be found in Table 2.3.

Table 2.3.:  $A$ - $D$  relationship parameters ( $A = \alpha D^\beta$ ) in the P3-scheme

"particle name"	$\alpha_{A-D}$	$\beta_{A-D}$
cloud droplets, rain drops	$\alpha_{spher} = \frac{\pi}{4}$	$\beta_{spher} = 2$
spherical ice, graupel		
dense nonspherical ice	$\alpha_{empir} = 0.13$	$\beta_{empir} = 1.88$
partially rimed ice	$f(\alpha, \beta, a, b, D)$	$\beta_{empir} = 1.88$

#### 2.4.2.3. Size distribution

For all of the three hydrometeor categories (cloud droplets, rain drops and ice particles) the particle size distribution is described by a three-parameter gamma distribution

which can be derived from Equation 2.6 by setting  $\gamma$  to zero. Furthermore, there is an empirical relationship between the slope parameter and either  $N$  or the shape parameter for each category. As a result, there are only two free parameters left for each category.

Here, only the parameters of the size distribution of the ice category are discussed. These parameters depend on properties of the ice category like the  $m$ - $D$  relationship and the threshold values separating different  $m$ - $D$  relationship regions (see Table 2.2). Due to these different  $m$ - $D$  relationship regions, the parameters of the gamma distribution can not be determined analytically. Moreover the normalized mixing ratio of ice  $q_{norm,i}$  (defined as  $q_i$  divided by  $N_i$ ) is calculated for a variety of slope parameter  $\lambda_i$ . For this calculation the coefficients and threshold in Table 2.2 and the  $\mu_i$ - $\lambda_i$  relationship (see Equation 2.19) have to be taken into account. Multiple combinations of  $q_{norm,i}$  and  $\lambda_i$  are stored in a look-up table. During the model run the  $\lambda_i$  can be derived by calculating  $q_{norm,i}$  from the prognostic variables  $q_i$  and  $N_i$ . The same lookup-table also provides important prognostic variables like the mass- and the number-weighted sedimentation velocity ( $v_{sed,q}$  respectively  $v_{sed,N}$ ).

Knowing the shape parameter  $\lambda_i$ , the slope parameter  $\mu_i$  can be calculated through the empirical Equation 2.19 following Heymsfield (2003)

$$\mu_i = 0.00191 \lambda_i^{0.8} - 2 \quad (2.19)$$

Furthermore,  $\mu_i$  is limited to the range  $0 < \mu_i < 6$ . The lower limit of  $\mu_i$  is set to avoid infinitesimal numbers at diameters near zero. The upper limit is a restriction by the measurements of Heymsfield (2003). Nonzero  $\mu_i$  occurs according to Equation 2.19 only for size distributions with  $\lambda_i > 7000 m^{-1}$  which corresponds to a mean particle size of approximately 0.17 mm (Morrison and Milbrandt, 2015). Thus, size distributions with larger mean particle size have the shape of an exponential distribution.

Figure 2.4 illustrates the impact of the predicted bulk properties to the size distribution. As described above  $q_{norm,i}$  defines the shape of the distribution.  $F_{rim}$  and  $\rho_{rim}$  further specify the thresholds between the dense spherical ice, graupel and partially rimed ice particle as well as some coefficients as stated in Table 2.2.

#### 2.4.2.4. Ice-phase processes in P3

As this study focuses on the analysis of the ice phase, this section summarizes only the approaches in the handling of microphysical processes of the ice phase.

In contrast to most bulk schemes the P3-scheme predicts two mixing ratios for one ice category ( $q_{rim}$  and  $q_i$ ). While  $q_{rim}$  traces the evolution of rimed ice mass,  $q_i$  is the sum of both rimed and unrimed ice mass. Therefore one has to decide which microphysical processes increase/decrease the rime ice mass and which processes only increases/decreases the unrimed ice mass. Morrison and Milbrandt (2015) chose to count the ice mass produced by the collection of rain drops and cloud droplets ( $qrcol$  and  $qccol$ ), but also immersion freezing of both - rain drops and cloud droplets ( $qrheti$  and  $qcheti$ ) - as rimed mass. The mass produced by depositional growth ( $qidep$ ) and deposition/condensation freezing ( $qinuc$ ) counts as unrimed mass and thus only increases  $q_i$  and not  $q_{rim}$ . The abbreviations for the process rates corresponding to

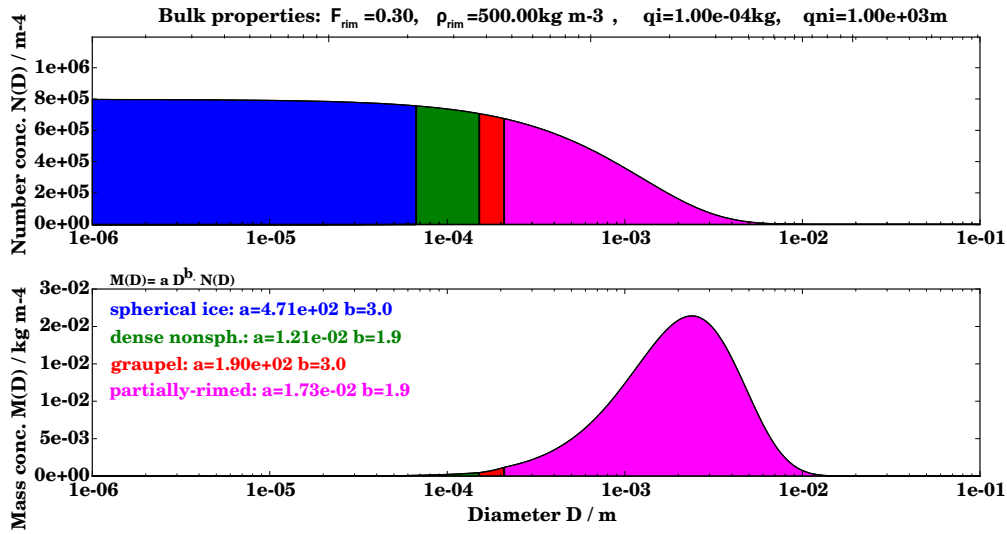


Figure 2.4.: Example of a size distribution of the ice category including different regions of  $m$ - $D$  relationship. The upper plot shows the number concentration  $N(D)$  of a single grid-box. The bulk properties of this grid-box are presented above the plot. The colors indicate the respective region of a  $m$ - $D$  relationship. Blue represents the region where the  $m$ - $D$  relationship of unrimed spherical ice is assumed. In the same way green represents dense nonspherical ice, red represents graupel (spherical completely rimed ice) and purple represents non-spherical partially rimed ice. The lower plot depicts the mass concentration  $M(D)$  of the same grid-box.  $M(D)$  can be derived from  $N$  by multiplying with the assumed  $m$ - $D$  relationship for an individual particle (see Equation 2.13).

the microphysical processes and their sign in changing the prognostic variables are listed in Table 2.4. Each process which decreases  $q_i$  also decreases  $q_{rim}$  in a way that  $F_{rim}$  is held constant. Immersion freezing, as well as deposition/nucleation freezing, increase  $N_i$  because these processes lead to a formation of new ice crystals. In contrast the sublimation, melting and aggregation all reduce  $N_i$ . The reduction of  $N_i$  by sublimation ( $n_{isub}$ ) and melting ( $n_{imlt}$ ) is proportional to  $q_{isub}$  and  $q_{imlt}$  respectively, scaled by the inverse of  $q_{norm,i}$ , so that  $q_{norm,i}$  is held constant. This reduction takes the faster sublimation/melting of smaller ice particles into account (see Equation 2.7) which can also lead to a complete disappearance of smaller ice particles.

Processes which do not change  $q_{rim}$  also do not change  $B_{rim}$ . Collection of rain drops by ice particles, contact freezing and immersion freezing are assumed to produce rime densities close to solid bulk ice around  $900\text{ kg m}^{-3}$ . Less dense rime mass can only be produced by the collection of cloud droplets by ice particles. Processes which decrease  $q_i$  do not change  $\rho_{rim}$  because  $B_{rim}$  decreases in proportion with  $q_i$ .  $B_{rim}$  can also be reduced at a temperature near  $0^\circ\text{C}$  by wet growth which leads to a densification of the particles (Musil, 1970).

Table 2.4.: List of ice phase process rates in the P3-scheme. The second and fourth column show the abbreviations of the rate by which  $q_i$  and  $N$  is changed due to the considered process. The (+) or the (-) after the abbreviation depicts if the process increases or decreases the prognostic variables ( $q_i$  and  $N_i$ ). Column three additionally indicates if the change only counts for  $q_i$  or also for  $q_{rim}$ .  $F_{rim}$  const. indicates that  $q_{rim}$  is changed in a way so that  $F_{rim}$  is held constant.

process name	change in mixing ratio	change in $q_{rim}$	change in $N_i$
collection of rain drops	$qrcol(+)$	yes	-
collection of cloud droplets	$qccol(+)$	yes	-
homogeneous freezing of rain drops	$qrhom(+)$	yes	$rchrom(+)$
homogeneous freezing of cloud droplets	$qchom(+)$	yes	$nchom(+)$
immersion freezing of rain drops	$qrheti(+)$	yes	$nrheti(+)$
immersion freezing of cloud droplets	$qcheti(+)$	yes	$ncheti(+)$
depositional growth deposition	$qidep(+)$	no	
nucleation	$qinuc(+)$	no	$ninuc(+)$
sublimation	$qisub(-)$	yes ( $F_{rim}$ const.)	$nisub(-)$
melting	$qimlt(-)$	yes ( $F_{rim}$ const.)	$nimlt(-)$
aggregation	-	-	$nisl(-)$

The microphysical process formulation of the warm phase processes (except cloud droplet activation), the collection of rain drops/cloud droplets by ice, the depositional growth, the sublimation, melting and aggregation are taken from the original P3-scheme and can be found in the Appendix of Morrison and Milbrandt (2015). Cloud droplet activation is implemented with the parametrization from Hande et al. (2016). Immersion freezing of rain drops/cloud droplets and deposition nucleation are implemented based on Hande et al. (2015).

It should be noted, that the here used implementation of the P3-scheme in ICON used here does not account for contact freezing and secondary ice formation. Hande and Hoose (2017) stated that immersion freezing dominates over contact freezing, so the omission of contact freezing here is not expected to be significant. Secondary ice formation is not used in the one-category P3-scheme because higher concentrations of small particles would smear out the properties of the large particles (Morrison and

Milbrandt, 2015), which is one of the reason for the extension of the P3-scheme to its multicategory version.

### 2.4.3. The Seifert and Beheng (SB) two-moment scheme

The Seifert and Beheng two-moment (SB; Seifert and Beheng, 2006a) scheme is used in this work mainly for comparison. Therefore it is not described in the same level of detail as the P3-scheme. Rather, this section will underline the conceptual differences between the P3-scheme and common two-moment schemes with multiple ice categories.

The SB-scheme used in this study has six different hydrometeor categories implemented, two for the liquid and four for the ice phase. The liquid phase is treated similarly to P3 with a distinction between the smaller cloud droplets and the larger rain drops. The main differences are the use of a different autoconversion scheme and the use of saturation adjustment within the SB-scheme (see Section 2.4.4). For autoconversion the P3-scheme uses the parametrization of Khairoutdinov and Kogan (2000) while the SB-scheme uses the parametrization of Seifert and Beheng (2001).

The ice phase is separated into cloud ice, snow, graupel and hail categories representing different types of solid hydrometeors. The bulk properties corresponding to these categories are  $q_i, q_s, q_g, q_h$  (which are the mass mixing ratio of the cloud ice, snow, graupel and hail category) and  $N_i, N_s, N_g, N_h$  (which are the number concentration of the cloud ice, snow, graupel and hail category). All of these four categories have prescribed properties such as the size distribution parameters or the  $m$ - $D$  relationship parameters. Those set of parameters aim to represent the different particle properties. Thus, the change in properties of the ice size distribution (e.g. by aggregation) can be represented either by a change of a prognostic variable corresponding to one category (e.g. the reduction of  $N_s$  by self-collection within the snow category) or by conversion between categories (e.g. the collection of cloud ice by snow - which changes  $q_i, N_i$  and  $q_s$ ).

#### 2.4.3.1. Size distribution

The SB-scheme uses the full four parameter modified gamma-distribution (Equation 2.6). Although Seifert and Beheng (2006a) formulated the size distribution as a function of particle mass we will discuss the distribution as a function of  $D$  to be consistent with the Sections 2.2 and 2.4.2.3.  $\mu$  and  $\gamma$  are constant for a given particle category (see Table 2.5). In contrast to the P3-scheme, the size distribution can be written in a closed form as a function of the mass mixing ratio and the number concentration (see Seifert and Beheng (2006a), Appendix A).

The parameters which define the shape of the size distribution are listed in Table 2.5. The differences in the  $\mu$  parameter between the P3- and the SB-scheme should be noted. While within the P3-scheme the  $\mu$  parameter is directly linked to the  $\lambda$  parameter via an empirical equation, the SB-scheme prescribes fixed values of  $\mu$  for each category. Moreover all of the categories (including the ice phase categories) have a nonzero  $\mu$  implemented. Therefore the shape of the size distribution of the SB ice phase categories is broader for small mean diameter (see upper left plot in Figure 2.5)

Table 2.5.: Size distribution parameters in Equation 2.6 and  $m$ - $D$  relationship parameters for all six categories in the SB-scheme

category	cloud water	rain	cloud ice	snow	graupel	hail
$\mu$	5	2	2	2	5	5
$\gamma$	3	1	1	1.5	1	1
$a$	524.5	524.5	1.59	0.04	500.8	392.3
$b$	3	3	2.56	2.00	3.18	3

and narrower for larger mean diameter (see upper right plot in Figure 2.5) than the size distribution of the P3 ice category.  $\gamma = 1.5$  for the snow category leads to a more left-skewed shape than the one of the SB ice or the P3 ice category ( $\gamma = 1$ ).

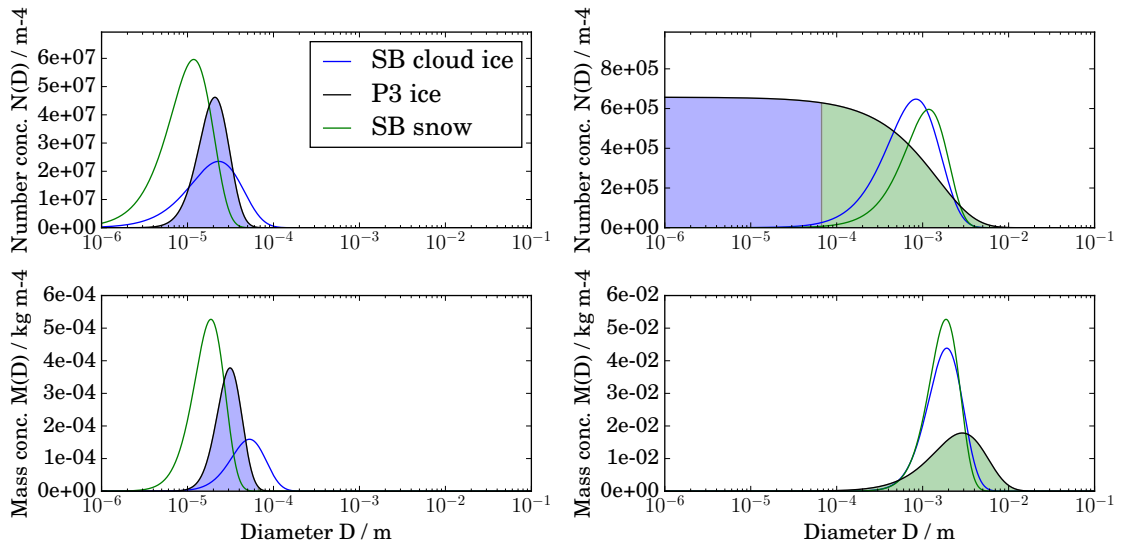


Figure 2.5.: Comparison of the size distribution shape of unrimed categories within the P3 and SB-scheme. Shown are the size distribution of the P3 ice category (black line with blue shading below line marking the region where dense spherical ice is assumed and green shading where dense nonspherical ice is assumed), the SB ice category (blue line) and the SB snow category (green line). The upper row shows the spectral resolved number concentration, the lower row the spectral resolved mass concentration. All of the plots correspond to the same  $N$  of  $10^3 \text{ kg kg}^{-1}$ .  $q$  is chosen as  $10^{-8} \text{ kg}^{-1}$  and  $10^{-4} \text{ kg}^{-1}$  for the left respectively the right plot.

#### 2.4.3.2. Ice-phase processes in SB

The SB-scheme has various parametrizations concerning ice microphysical processes implemented. Those are ice nucleation, depositional growth of ice particles, freezing of water drops, collection processes (aggregation and riming), melting, sublimation

and secondary ice formation. The implementation of these processes can mostly be found in Seifert and Beheng (2006a). The ice microphysical process which differs from those described in Seifert and Beheng (2006a) is ice nucleation for which the original parametrizations was replaced with the one from Hande et al. (2015) as in the P3-scheme version used in this study.

In the following, we want to point out two microphysical processes which are handled with a different approach in the SB-scheme compared to the P3-scheme. The first is sublimation, the second aggregation. In the SB-scheme sublimation decreases  $q_i$  in the same way as deposition increases  $q_i$  while  $N_i$  is held constant in contrast to the P3-scheme where  $q_{norm,i}$  is held constant during sublimation. In the P3-scheme aggregation can be expressed with only one process rate which decreases  $N_i$ . The situation is, due to the four different ice phase categories, more complex for the SB-scheme. In the SB-scheme aggregation processes can affect both  $q$  and  $N$  of two categories (e.g. the collision of two ice particles which form a snow particle). Moreover, in the P3-scheme aggregation rates are calculated using the kernel derived from the sweep-out volume (see Equation 2.9). In contrast, the SB-scheme applies an approximation which uses mean properties (like averaged sedimentation velocities and their spread) of the distribution (see also Section 2.3.3) (Seifert and Beheng, 2006a).

### 2.4.4. Treatment of supersaturation

There are two fundamentally different approaches used in the SB and the P3-scheme to treat supersaturation. In the first approach liquid clouds are kept at water-saturation at each timestep. In the presence of liquid hydrometeors all of the excessive water vapour will condense or evaporate immediately if the vapor pressure is not equal to the saturation pressure. Other variables such as the temperature  $T$  or the pressure  $p$  are adjusted according to this condensation rate. This approach is also called saturation adjustment. For lack of an implemented explicit treatment of supersaturation, saturation adjustment is used in all simulations with the SB-microphysics scheme in this study. In contrast, the P3-scheme used in this study has by default an explicit treatment of supersaturation implemented which solves the condensation equations.

In contrast to most other processes within the microphysics schemes the different treatment of supersaturation can lead to significant differences in the feedback to the dynamics. This feedback manifests itself in buoyancy production and thereby higher magnitude of vertical wind speeds due to latent heat which is enhanced when using saturation adjustment (Grabowski and Morrison, 2017).

## 2.5. Remote sensing of clouds by Radars

Radars (RADIO Detection And Ranging) emit radio-waves and estimate properties based on the received signal which was backscattered in the atmosphere. In atmospheric science radars are used widely to detect precipitation fields. For this purpose, radars with a frequency of several centimeters (C- or S-Band radar) are dominant

due to small attenuation effects (see Section 2.5.5) and easier interpretable signals (most scatterers are in the Rayleigh-regime; see Sections 2.5.2 and 2.5.3). Radars with wavelengths in the range of several millimeters up to a few centimeters (e.g. X-,K- and W-Band radar) find their application in the investigation of cloud properties to which they are more sensitive than the longer wavelength radars. Basic definitions of radar meteorology are given in Section 2.5.1 before the details of scattering and attenuation are discussed in the Sections 2.5.2 to 2.5.5. The forward operator PAMTRA, an application to compare model output and radar observations, is presented in Section 2.5.6 and the field of multi-frequency analysis is introduced in Section 2.5.7.

### 2.5.1. Basics of radar meteorology

The most basic application of a radar is to measure the power which is backscattered by e.g. raindrops to the radar and detected by the antenna. The basic metrics which measure this power is described in this section.

More advanced radars are Doppler radars and polarimetric radars. In this study we use non-polarimetric Doppler radars at several frequencies. Doppler radars are additionally capable of measuring the motion of the hydrometeors in the direction of the radar beam. Polarimetric radars can determine additional parameters such as the linear depolarization ratio which gives additional information about the shape of the scatterers.

$$P_r = \frac{C_{rad}}{R^2} \int_0^\infty \sigma_b(D) N(D) dD = \frac{C_{rad}}{R^2} \frac{\pi^5}{\lambda_w^4} |K_w^2| Z_e \quad (2.20)$$

The backscattered power  $P_r$  to the radar can be formulated with Equation 2.20 (Peichang and Du Bingyu, 2001). The second equal-sign has to be seen as a definition. Here  $C_{rad}$  is a constant for a given radar,  $\sigma_b$  represents the backscatter cross section,  $\lambda_w$  the wavelength of the radar beam and  $|K_w^2|$  the dielectric factor of water.

More often than  $P_r$  the radar reflectivity  $Z_e$  is used.  $Z_e$  has the advantage over  $P_r$  to be independent of specific radar characteristics,  $\lambda_w$  and  $|K_w^2|$  if we consider liquid hydrometeors in the Rayleigh regime. Following from Equation 2.20, we can define  $Z_e$  as follows:

$$Z_e = \frac{\lambda_w^4}{\pi^5 |K_w^2|} \int \sigma_b(D) N(D) dD \quad (2.21)$$

As the size distribution  $N(D)$  was already discussed in Section 2.3 and 2.4, we now want to take a closer look at  $\sigma_b$ .  $\sigma_b$  can be calculated exactly through Mie theory (see Section 2.5.2) or approximated with the Rayleigh theory or derivatives thereof (see Sections 2.5.3 and 2.5.4). In practice, Mie theory is only applied for spherical particles due to the expensive calculations for more complex particle shapes. Rayleigh-scattering is not applicable for larger particles. Hence other scattering theories for large nonspherical particles have been developed such as the Self-Similar Rayleigh-Gans scattering (see Section 2.5.4).

### 2.5.2. Mie-scattering

Mie (1908) derived a theory of diffuse reflection from the Maxwell equations. Applications for atmospheric particles were based on this theory to derive  $\sigma_b$  for spherical particles.

Based on the theory of Mie (1908),  $\sigma_b$  of spherical dielectric particles can be expressed by an infinite series, where each element represents an electric and a magnetic dipole (see Equation 2.22).

$$\sigma_b = \frac{\pi D^2}{4 x^2} \left| \sum_{n=1}^{\infty} (2n + 1) (-1)^n (a_n - b_n) \right|^2 \quad (2.22)$$

To derive the coefficients  $a_n$  and  $b_n$  (which depend on the complex refractive index and  $x$ ) is the key issue in the Mie calculations.

The gray solid line in Figure 2.6 shows the normalized  $\sigma_b$  as a function of the size parameter  $x = kD = \pi \lambda_w^{-1} D$  (here  $k$  represents the wavenumber). We can see that  $\sigma_b$  increases proportional to  $D^6$  for smaller  $x$ . When  $x$  reaches one (which means that the wavelength of the radiation is equal to the size of the scatterer) the slope decreases. Going to even larger  $x$ ,  $\sigma_b$  decreases and increases multiple times. These resonance effects are due to the alternation of constructive and destructive interference of the radiation.

The resonance region of the Mie-scattering has to be considered especially for cloud radars (with  $\lambda_w$  down to a few millimeters for the W-Band). For these wavelengths only small scatterer with  $D \ll 1$  mm can be treated by the Rayleigh approximation. This fact complicates the analysis of the backscattered signal but can also be used when analyzing measurements at multiple radar frequencies (see Section 2.5.7).

### 2.5.3. Rayleigh-scattering

The Rayleigh approximation is valid if the scattering particles are small compared to the wavelength ( $x \ll 1$ ). Then the far zone of the electric field can be considered as a dipole. Therefore we can reduce Equation 2.22 by taking only the lowest order of the series into account. This leads to Equation 2.23.

$$\sigma_b = \frac{\pi^5 |K|^2 D^6}{\lambda_w^4} \quad (2.23)$$

If we insert Equation 2.23 into Equation 2.21 we get  $Z_e = \int D^6 N(D) dD$  which is the sixth moment of the size distribution and motivates the definition of  $Z_e$ .

### 2.5.4. Self-Similar Rayleigh-Gans scattering

The main restriction of the Rayleigh theory is the condition  $x \ll 1$ . Nevertheless, theories based on the Rayleigh theory have been developed to calculate the backscatter from particles with  $D > \lambda_w$ . Those are mainly based on the Rayleigh-Gans approximation. One of them is the Self-Similar Rayleigh-Gans (SSRG) theory. The Rayleigh-Gans approximation requires less rigid restrictions ( $|m_{refr} - 1| \ll 1$  and

$2x|m_{refr} - 1| \ll 1$ ; with the refractive index  $m_{refr}$ ) than the Rayleigh theory itself (Hulst and Hulst, 1957).  $m$  is the refractive index which is close to 1.77 for solid ice but close to 1 for an ice aggregate in which most of the volume within the imaginary sphere (with the diameter  $D$ ) is air.

The Rayleigh-Gans approximation formulates  $\sigma_b$  for an arbitrarily oriented particle with the area of the particle  $A(s)$  intersected by a plane at the range  $s$  (Equation 2.24).  $s$  hereby points in the direction of the wave propagation.

$$\sigma_b = \frac{9\pi k^4 |K|^2}{4\pi} \left| \int_{-\frac{D}{2}}^{\frac{D}{2}} A(s) \exp(i 2 k s) ds \right|^2 \quad (2.24)$$

One method to derive  $\sigma_b$  based on Equation 2.24 is to assume spheroids with a homogeneous mixture of ice and air (which is then called "soft spheroids") and get a simple equation for  $A(s)$ . Hogan and Westbrook (2014) showed that the resulting  $\sigma_b$  differs significantly from their approach (comparison of the dashed black line and the gray line in Figure 2.6). Rather than making a simple assumption on  $A(s)$  which should be valid for all kind of snow particles, Hogan and Westbrook (2014) derived an equation for the integral in Equation 2.24 based on the self similarity of the aggregates.

$$\sigma_b = \frac{9\pi k^4 |K|^2 V^2}{16} \left\{ \cos^2(x) \left[ \left(1 + \frac{\kappa_{fit}}{3}\right) \left(\frac{1}{2x + \pi} - \frac{1}{2x - \pi}\right) - \left(\frac{\kappa_{fit}}{2x + 3\pi} - \frac{\kappa_{fit}}{2x - 3\pi}\right) \right]^2 + \beta_{fit} \sum_{j=1}^n (2j)^{-\gamma_{fit}} \sin^2(x) \left[ \frac{1}{(2x + 2\pi j)^2} + \frac{1}{(2x - 2\pi j)^2} \right] \right\} \quad (2.25)$$

Here  $V$  is the volume of solid ice of the aggregates.  $\beta_{fit}$ ,  $\gamma_{fit}$  and  $\kappa_{fit}$  are parameters of a statistical description for  $A(s)$  of an ensemble of aggregates.

Furthermore, Leinonen et al. (2017) stated that the self-similar Rayleigh-Gans (SSRG) can be used for particle ensemble of aggregates up to a large degree of riming which will be relevant in Chapter 3. Figure 2.6 shows the normalized  $\sigma_b$  for a numerically generated ensemble of aggregates calculated with multiple assumptions. It shows good agreement up to  $x = 50$  between the mean of  $\sigma_b$  ( $\overline{\sigma_b}$ ) calculated by Equation 2.25 and  $\overline{\sigma_b}$  derived explicitly from Equation 2.24 with the exact  $A(s)$  values. In contrast  $\overline{\sigma_b}$  calculated by the concept of soft spheres shows an underestimate for  $x > 1$  which becomes particularly obvious for higher  $x$ .

### 2.5.5. Attenuation by gases and hydrometeors

The radar beam undergoes attenuation both on the way to the scatterer and the way back to the radar. Attenuation has to be considered when analyzing  $Z_e$  (or other radar observables). In the atmosphere, attenuation occurs due to both gases and hydrometeors. While attenuation by gases can be taken into account more easily if the atmospheric conditions are known, estimating attenuation by hydrometeors

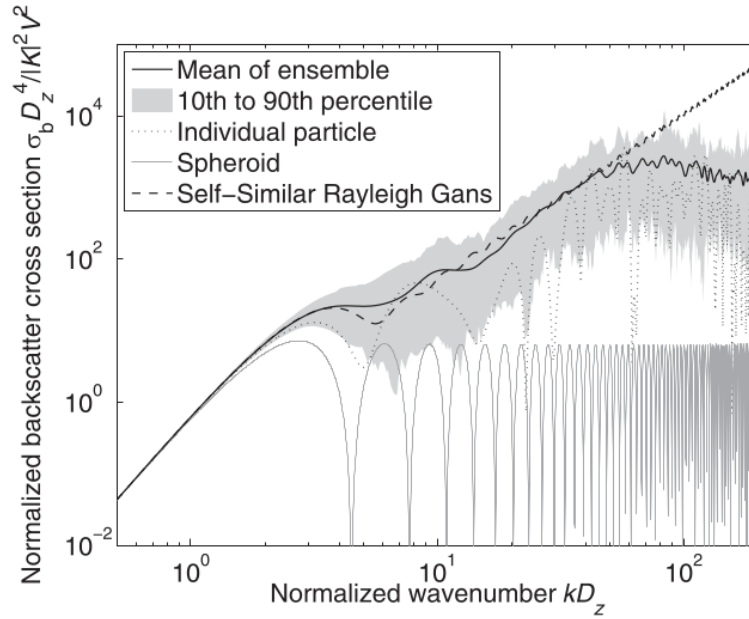


Figure 2.6.: Normalized backscattering cross section  $\sigma_b$  for a numerically generated ensemble of aggregates. The mean ( $\overline{\sigma_b}$ ) and 10th to 90th percentile of  $\sigma_b$  calculated explicitly with the Rayleigh-Gans theory (see Equation 2.24) for this ensemble is depicted in the black line respectively in gray shading.  $\overline{\sigma_b}$  corresponding to Equation 2.25 is shown in the dashed black line. For reference  $\overline{\sigma_b}$  for the ensemble calculated by the concept of soft spheroids and a randomly picked individual particle of the ensemble is shown in gray solid respectively gray dashed lines (from Hogan and Westbrook, 2014)

needs a more profound knowledge of the scatterers along the path of the radar beam. In general, the attenuation by hydrometeors is largest for the shortest radar wavelengths. As a result, C- and S-Band radars are less affected by attenuation than cloud radars. Comparing different hydrometeor types, attenuation by cloud droplets has the highest impact, while attenuation is less important for rain drops, snow and cloud ice (Stephens, 1994).

### 2.5.6. Passive and Active Microwave TRANSfer model (PAMTRA)

The comparison of observations and models is per se difficult because model variables are not observed, and vice versa. PAMTRA is a forward operator which can simulate observations from passive and active instruments using model data and therefore make a comparison between e.g. vertically pointing radars and atmospheric models possible. PAMTRA is based on Kollias et al. (2011) and was further developed at the Institute of Geophysics and Meteorology (IGM), University of Cologne. In the following, the input variables to PAMTRA are described, followed by the steps performed during

a PAMTRA simulation which are relevant for the calculation of  $Z_e$  and the thereby provided output (see also Figure 2.7).

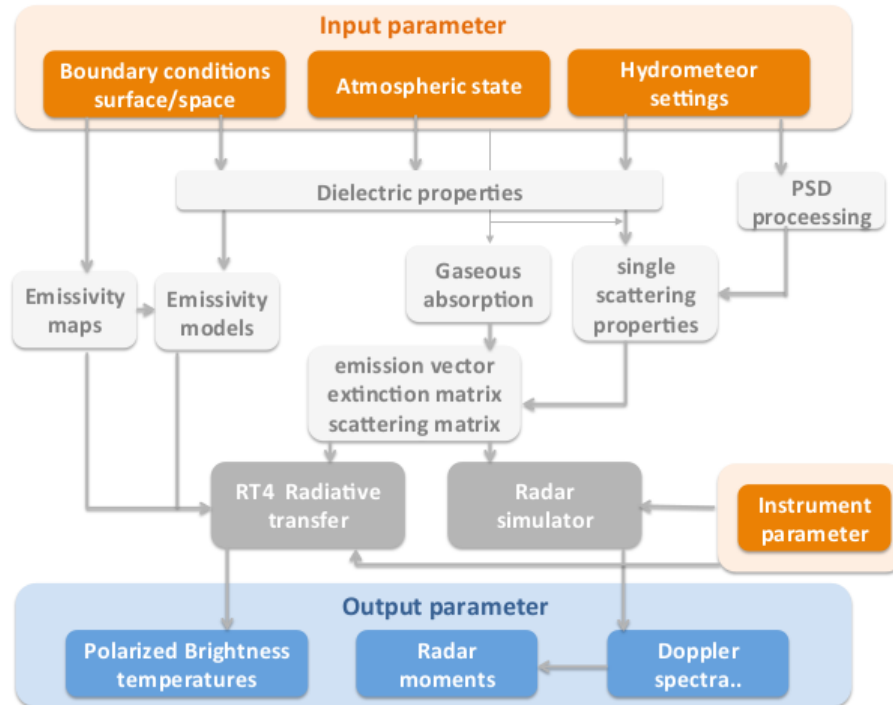


Figure 2.7.: Flowchart of the forward operator PAMTRA including input parameter (in orange), steps performed during the PAMTRA simulation (in grey) and thereby provided output (in blue) (taken from Maahn (2015))

Input variables to PAMTRA are the boundary conditions of the surface and the space (which are especially relevant for passive instruments), properties describing the atmospheric state (including  $T$ ,  $p$  and  $RH$ ), instrument parameters (e.g. the frequency or the Nyquist velocity of the radar) and hydrometeor properties. These hydrometeor properties include the phase, the aspect ratio, the  $m$ - $D$  and  $A$ - $D$  relationship parameters, the scattering and sedimentation velocity model and multiple parameters describing the size distribution of the hydrometeors.

The latter can be provided either via a bin or a bulk interface. The bin interface requires the input of projected area and particle mass at the middle of each bin (for the ice phase) and the number of particles in each bin interval (for both ice and liquid phase). In contrast, the bulk interface uses the moments (e.g.  $N$  and  $q$ ) of the particle category, the parameters of the size distribution and  $m$ - $D$  and  $A$ - $D$  relationship parameter (which must be valid for all diameters) to process number, mass and projected area in each bin internally.

Given this input, PAMTRA can calculate the dielectric properties (e.g. the refractive index), absorption by gases and the scattering properties of single particles. The latter are calculated depending on the scattering model defined by the user (the theory and

formulation behind some of the possible models are described in the Sections 2.5.2 to 2.5.4). These calculations are done for each bin and hydrometeor category separately.

If the user chooses to get the radar moments as an output,  $Z_e$  is derived by integrating  $N(D) \cdot \sigma_b$  over the whole spectrum and summing up the contribution of all hydrometeor categories. PAMTRA is also capable of simulating the Doppler spectra, as explained in detail in Maahn (2015).

At the end of the PAMTRA simulation similar steps as in the postprocessing of real radar data (including the removal of the radar noise which was artificially added before the calculation of the radar moments) are performed (Maahn, 2015).

### 2.5.7. Multi-frequency analysis

As we have seen in the Sections 2.5.1 to 2.5.4,  $\sigma_b$  varies with  $x$  which is proportional to  $D$  and  $\lambda_w^{-1}$ . If the same scatterer is observed by radars with different  $\lambda_w$  we have to consider that  $x$  increases with decreasing  $\lambda_w$ . Keeping in mind that  $Z_e$  is derived from the measured backscattered power assuming scatterers in the Rayleigh regime, we can see that two radars with different  $\lambda_w$  which observe scatterers which are in the Rayleigh regime will give the same  $Z_e$ . On the other hand, if there are scatterers present which can not be treated by the Rayleigh-regime because the condition  $x \ll 1$  is no longer satisfied,  $Z_e$  of the radar with the longer  $\lambda_w$  will be smaller than  $Z_e$  of the radar with the shorter  $\lambda_w$ .

Matrosov (1992) showed that this effect can be linked to  $D_{mean}$  and later fitted a power law relation between the dual wavelength ratio (DWR; defined by Equation 2.26) and  $D_{mean}$  (Matrosov, 1998).

$$DWR = Z_{e,\lambda_{w,1}} - Z_{e,\lambda_{w,2}} \quad (2.26)$$

where  $Z_{e,\lambda_{w,1}}$  represents  $Z_e$  detected by the radar with  $\lambda_{w,1}$  and  $Z_{e,\lambda_{w,2}}$  represents  $Z_e$  detected by the radar with  $\lambda_{w,2}$  (both in dB).

Kneifel et al. (2015) and others extended this approach by the use of an additional radar with  $\lambda_{w,3}$ . This triple frequency approach can give additional information of the scatterers. By comparison of in-situ ground based measurements and DWR they derived a conceptual model how the bulk properties of the ice phase hydrometeor manifests in the triple-frequency space (see Figure 2.8). They found that the increase of  $D_{mean}$  takes place along a specific particle curve (e.g. the light or the dark blue curve in Figure 2.8) while the densification (increase of the effective particle density) of the particle distribution leads to a rotation of this curve (indicated by the array with a color gradient from light to dark blue).

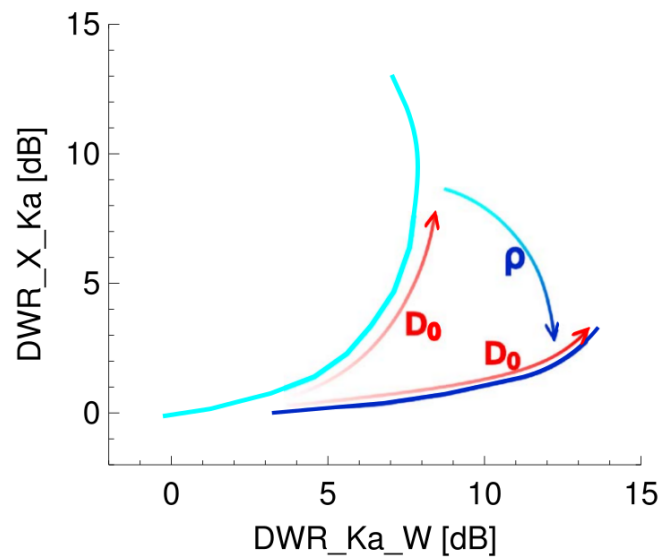


Figure 2.8.: Schematic illustration of the regions of different particle types in the triple-frequency space (from Kneifel et al. (2015)). Shown are typical measurements given specific particle properties in a space spanned by two DWR-metrics. The light blue line depicts a particle curve for low density particles, the dark blue line for high density particles. The red arrow indicates in which direction the particles get larger while the array with a color gradient from light to dark blue indicates how densification of particles appear in this diagram.



### 3. Adaption of PAMTRA to P3

While PAMTRA was already capable of handling model output from the SB-scheme, an adaption of PAMTRA to the P3-scheme had to be developed during this work, in order to analyze the forward operated signal from both schemes. The variable size distribution parameters and the varying  $m$ - $D$  relationship (for the ice category) would hamper the implementation via the bulk interface. Due to these issues, the bin interface is used although the P3-scheme predicts bulk properties. In the following, the adaption is explained with the help of the pseudo-code shown in Listing 3.1.

In the code, PAMTRA is called via the python interface pyPAMTRA (see Maahn (2015)) for each timestep of the model output file, which should be forward operated. This adaption only uses the eight prognostic variables of P3 (concerning the hydrometeor properties) so that no additional output from ICON is necessary for the PAMTRA simulation. Therefore at the beginning of each PAMTRA simulation some bulk properties of the hydrometeors must be re-diagnosed. Those properties are the two size distribution parameters ( $\mu$  and  $\lambda$ ) for each of the three hydrometeor categories,  $F_{rim}$  and  $\rho_{rim}$ . Furthermore, the thresholds  $D_{crit,s}$  and  $D_{crit,r}$  between the  $m$ - $D$  relationship regions of snow and graupel and graupel and partially rimed ice, respectively, and the non-fixed parameters of the  $m$ - $D$  and the  $A$ - $D$  relationship are re-diagnosed. These diagnoses are tightly based on the assumptions and internal calculations of the P3-scheme

In the following part of the code, different "categories" that appear within the PAMTRA core have to be separated. These "categories" are the P3-scheme categories of cloud droplets and rain, but also the diameter region of the P3 ice category where we can apply the same scattering routine. Mie-sphere (a scattering routine performing Mie calculations for spheres) is applied for the dense spherical particles and the graupel particles, whereas the SSRG-scattering routine (based on Hogan and Westbrook (2014); see also 2.5.4) is applied for the dense non-spherical and the partially-rimed particles.

For each category,  $N_0$  can be calculated by a simple analytic function. Based on  $N_0$  and the other size-distribution parameters, the number of particles per size bin ( $n_{ds}$ ; `pamData[.]` indicates that this variable is passed to PAMTRA via the pyPAMTRA interface) can be calculated.

$n_{ds}$  is already sufficient input in case of liquid hydrometeors (which are assumed to be spherical and have the density of water at the current ambient temperature). For the ice category, also the aspect ratio, the area ( $area_{ds}$ ) and the mass ( $mass_{ds}$ ) - or the density ( $rho_{ds}$ ) for the spherical particle - at the center of each bin must be specified. For the latter two, the  $m$ - $D$  and the  $A$ - $D$  relationship as described in Section 2.4.2.1 and 2.4.2.2 are taken. The aspect ratio is set to 1 for the spherical particles and to 0.6 (in accordance with Hogan et al. (2012)) for the non-spherical particles. Finally PAMTRA can be run by specifying the radar frequencies.

### 3. Adaption of PAMTRA to P3

---

Listing 3.1: Pseudo-code of the adaption of PAMTRA to the P3-scheme

---

```
#calculate shape parameters of the warm phase based on moments, T and p
#1. for cloud droplets
[mu_c,lamc] = get_cloud_dsd(qc,qnc,pres,temp)
#2. for rain drops
[mu_r,lamr] = get_rain_dsd(qr,qnr,pres,temp)

Frim = qirim/(qi+qirim) # calculate bulk rime fraction
rho_rim = calc_bulkRhoRime(qirim,birim) #calculate bulk rime density

#get parameters which describe P3 ice category distribution:
[mui,lami, #parameter of size distribution
dcrit,dcrits,dcritr, #thresholds between m-D relationship-regions,
cs1,ds1,cs,ds,cgp,dg,csr,dsr, #m-D relationship parameter
aas1,bas1,aas2,bas2,aas3,bas3,aas4,bas4] #A-D relationship parameter
=calc_threshold_and_params_in_size_dist(qi,qni,rho_rim,Frim)

for i_hydromet in range(0,4):#loop over different "categories":
#i_hydromet==0 -> cloud water; i_hydromet==1 -> rain drops
#i_hydromet==2 -> ice (mie); i_hydromet==3 -> ice (ssrg)
#cloud water and rain are real categories, the number of categories in
#the ice phase is the number of scattering-routines used in the ice phase
#calculate intercept parameter for each "categories"
N0 = qn...lam...*(mu...+1.)/gamma(mu...+1.)
for i_h in range(0,num_lev):#loop over vertical levels
#calculate number density [m-3] with diameter d_ds and bin with d_ds
pamData[n_ds] = N0*d_ds**mu...*exp(-lam...*d_ds)*del_ds
if i_hydromet>=2:#if ice phase
for i_bin in range(0,nbins):#loop over size range
if d_ds[i_bin]<=dcrit and i_hydromet==2:#spherical ice
pamData[rho_ds] = 917. #density of bulk ice
#mass_ds is not needed in mie-sphere
pamData[mass_ds] = pi/6.0 pamData[rho_ds]*d_ds[i_bin]**3
pamData[area_ds] = pi/4*d_ds[i_bin]**2
pamData[as_ratio] = 1.0
elif dcrit<d_ds[i_bin]<=dcrits and i_hydromet==3:
#dense nonspherical ice
pamData[area_ds] = aas2*d_ds[i_bin]**bas2
pamData[mass_ds] = cs*d_ds[i_bin]**ds
pamData[as_ratio] = 0.6
elif dcrits<d_ds[i_bin]<=dcritr and i_hydromet==2:#graupel
pamData[rho_ds] = cgp
#mass_ds is not needed in mie-sphere
pamData[mass_ds] = pi/6. *pamData[rho_ds]*d_ds[i_bin]**3
pamData[area_ds] = pi/4*d_ds[i_bin]**2
pamData[as_ratio] = 1.0
elif dcritr<d_ds and i_hydromet==3:#partially rimed
pamData[area_ds] = aas4*d_ds[i_bin]**bas4
pamData[mass_ds] = csr*d_ds[i_bin]**dsr
pamData[as_ratio] = 0.6
pam.runPamtra(rad_freq) #run pamtra by specifying radar frequency
```

---

---

The SSRG approximation is used here for the partially rimed ice. As stated in Section 2.4.2.1, partially-rimed particles are more rimed the closer they are to the threshold to graupel particles. For heavily-rimed particles (with  $D$  in vicinity of  $D_{crit,r}$ ) the SSRG scattering approach might not be accurate any more (Leinonen et al., 2017).

Next, idealized PAMTRA runs were performed to test the performance of the adaptation. Table 3.1 provides  $Z_{e,Ka}$  and  $DWR_{Ka-W}$  for the ice categories in the P3- and SB-scheme, respectively (for a given combination of bulk properties). These values have been calculated with PAMTRA by prescribing  $p$ ,  $RH$  and  $T$  as denoted above the table. In the following the term  $Z_e$  is used without any further notation of  $\lambda_w$ , when we deal with observed or simulated equivalent reflectivity detected by a 35.5 GHz-radar (which lies in the Ka-Band).  $Z_e$  corresponding to other frequencies will be denoted by an index.

In Table 3.1, the values corresponding to the size distributions in Figures 2.4 and 2.5 are highlighted in bold. The first highlighted row, which corresponds to a size distribution of a rather low  $q_{norm,i}$  of  $10^{-11}$  kg, produces  $Z_e$  of  $-66.79$  dBZ for the P3 ice category which is about 3 dB and 1 dB lower than the same combination for the SB cloud ice and the SB snow category, respectively. This difference results from the smaller amount of relative large particles of the P3 ice category (see Figure 2.5) compared to the SB ice category and the smaller individual particle mass (defined by the  $m$ - $D$  relationship) of the P3 category in comparison with the SB snow category. Similar considerations apply for the other unrimed size distributions, which correspond to higher  $q_{norm,i}$ . For example, the second highlighted row which corresponds to a size distribution with  $q_{norm,i} = 10^{-7}$  kg leads for the P3 ice category to  $Z_e = 11.23$  dBZ and has about the same offset to the SB categories as the combination of  $q$  and  $N$  discussed before.

A significant  $DWR_{Ka-W}$  value - which is measurable with currently used radars - for the unrimed size distributions of the P3 ice category only occurs for the second highlighted row with  $9.27$  dBZ. Here, the corresponding  $DWR_{Ka-W}$  value for the P3 category is about 3 dB and 2 dB higher than the  $DWR_{Ka-W}$  corresponding to the SB snow and cloud ice category, respectively. This difference can be explained by the higher amount of large particles in the P3 ice category (see Figure 2.5) which contribute mostly to the  $DWR_{Ka-W}$  value.

Table 3.1 also shows some combinations of bulk properties for size distributions where rime is present. The third highlighted row corresponds to a size distribution with relatively low  $F_{rim}$  and medium  $\rho_{rim}$ . Here, the idealized PAMTRA simulation gives a  $Z_e$  value of  $12.34$  dBZ and a  $DWR_{Ka-W}$  value of 0.08 dB.  $Z_e$  is reasonable as it is moderately higher than those of the unrimed size distribution with the same  $q$  and  $N$ . The smaller value for  $DWR_{Ka-W}$  can be explained by a lower  $\lambda_i$  (narrower distribution).  $Z_e$  increases with increasing  $F_{rim}$  for this combination of  $q$  and  $N$  reaching  $19.06$  dBZ for  $F_{rim} = 1.0$  and  $\rho_{rim} = 500$  kg m $^{-3}$ . An increase of  $Z_e$  can also be seen when  $F_{rim}$  is kept at 1.0 and  $\rho_{rim}$  is further increased.

Increasing  $F_{rim}$  leads to a decrease in  $DWR_{Ka-W}$  unless  $F_{rim}$  is close to 1, which is also connected to the decrease in  $\lambda_i$ . For  $F_{rim} = 1$ , also the largest particles are represented by the graupel rather than the partially rimed particle. This change

### 3. Adaption of PAMTRA to P3

manifests itself in an abrupt increase of  $DWR_{Ka-W}$  for  $F_{rim}$  close to 1. The dependency of  $DWR_{Ka-W}$  on  $\rho_{rim}$  for fully-rimed particles is further discussed in Section 5.6.1. Here, only the decrease of  $DWR_{Ka-W}$  with increasing  $\rho_{rim}$  at  $F_{rim} = 1$  should be noted.

Since the rimed SB categories (graupel and hail) contain only the more heavily rimed particles we can expect lower  $N$  when a similar composition of particles as in the P3 ice category should be represented. But due to the different  $\mu$  parameter in the size distribution (see Table 2.5) of the rimed SB categories these categories reach similar values of  $Z_e$  as the rimed P3 ice category already at lower values of  $N$  (in Table 3.1  $N$  for the rimed SB categories is set to 100 instead of 1000 as for all other categories).

Table 3.1.: Sensitivity of  $Z_e$  and  $DWR_{Ka-W}$  to prescribed parameters in different categories. Input to PAMTRA, besides the bulk properties of the hydrometeor categories which are indicated in the table, is:  $p = 735 \text{ hPa}$ ,  $RH = 90\%$ ,  $T = 268 \text{ K}$ . It should be noted that the Figures 2.4 and 2.5 show the size distributions corresponding to the rows highlighted in black and the corresponding combinations for the SB unrimed ice categories

category	scattering regime	$q$ kg kg <sup>-1</sup>	$N$ kg <sup>-1</sup>	$F_{rim}$	$\rho_{rim}$ kg m <sup>-3</sup>	$Z_e$ dB <sub>Z</sub>	$DWR_{Ka-W}$ dB
P3 ice	mie/ssrg	<b>10<sup>-8</sup></b>	<b>1000</b>	<b>0</b>	<b>0</b>	<b>-66.79</b>	0.002
		10 <sup>-6</sup>	1000	0	0	-26.68	0.08
	mie/ssrg	<b>10<sup>-4</sup></b>	<b>1000</b>	<b>0</b>	<b>0</b>	<b>11.23</b>	<b>9.27</b>
		<b>10<sup>-4</sup></b>	<b>1000</b>	<b>0.3</b>	<b>500</b>	<b>12.34</b>	<b>8.27</b>
		10 <sup>-4</sup>	1000	0.7	500	13.59	5.42
		10 <sup>-4</sup>	1000	1.0	200	16.79	13.33
		10 <sup>-4</sup>	1000	1.0	500	19.06	10.02
		10 <sup>-4</sup>	1000	1.0	700	19.77	9.28
		10 <sup>-4</sup>	1000	1.0	900	20.07	8.42
SB cloud ice	ssrg	10 <sup>-8</sup>	1000			-63.53	0.01
		10 <sup>-6</sup>	1000			-23.60	0.38
		10 <sup>-4</sup>	1000			14.45	7.01
SB snow	ssrg	10 <sup>-8</sup>	1000			-65.79	0.001
		10 <sup>-6</sup>	1000			-25.81	0.13
		10 <sup>-4</sup>	1000			12.35	6.41
SB graupel	mie	10 <sup>-4</sup>	100			19.62	13.78
SB hail	mie	10 <sup>-4</sup>	100			21.87	10.80

## 4. Case studies and model setup

Overall, the idealized PAMTRA simulations show comparable  $Z_e$  and  $DWR_{Ka-W}$  values for the same combination of bulk properties (as far as they are comparable). By considering only size distributions which do not contain rimed particles, the uncertainty in  $Z_e$  resulting from the parameters of the size distribution can be roughly estimated by 3 dB. The comparison of the bulk properties of the P3 ice category with those of the SB scheme is inherently difficult due to the possible allocation of  $q$  and  $N$  to the different SB categories. This difficulty emphasizes the importance of a metric such as  $Z_e$  which is independent of the conceptual approaches within the microphysics schemes and can also be compared to observations.

In this work, two different case studies are analyzed in order to investigate the performance of the P3-microphysics scheme and compare it with the SB-microphysics scheme. Both case studies are based on a day where a synoptically driven cloud system was present (a short synoptic description for the individual cases is given in the Sections 4.1 and 4.2).

Sections 4.3 to 4.4 describe the domain used, initialization method, as well, as the boundary data and give an overview of the simulations performed.

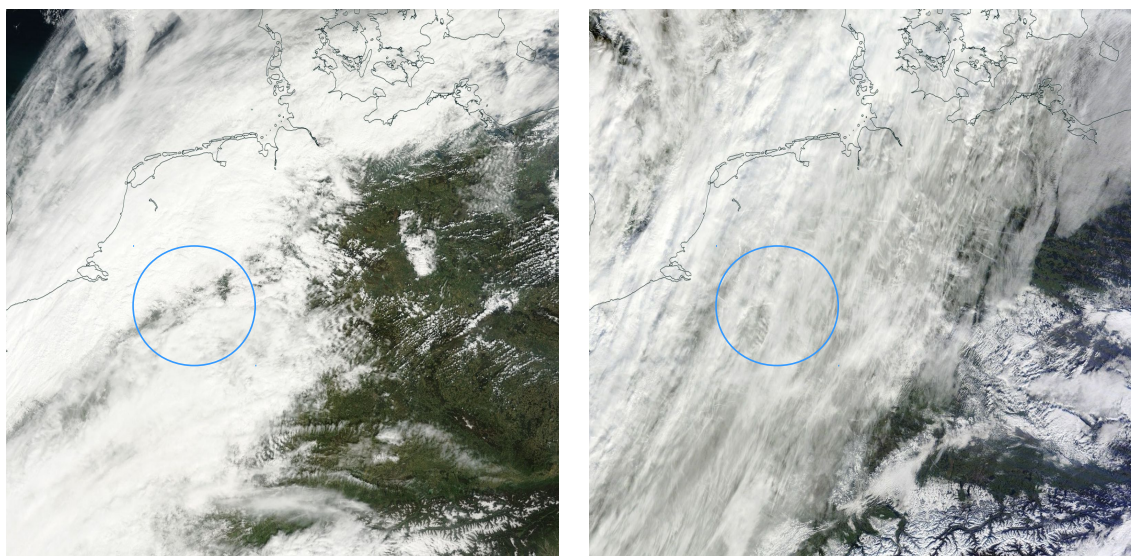
### 4.1. Case study 1: 26th April 2013

On 26th April 2013, a trough laid over the north-west of France and the Benelux countries. Accompanied with that, a cold front passed over central Europe. In the morning, the cloudiness increased until a complete-overcast situation was reached at noon. Only in the late afternoon did the cloudiness decrease slightly. There were several rain showers with light to medium rain in the course of the day. The wind blew from the south before the front-passage occurred and then turned to a northern wind after the frontal passage. Figure 4.1a shows the corrected reflectance for the morning hour which depicts the almost overcast situation in western to central Europe and a clear sky in the east of Germany.

The 26th April 2013 was part of the HOPE campaign (Macke et al., 2017) where a variety of instruments (including a vertically pointing Ka-Band radar) were placed in an area surrounding the town of Jülich.

### 4.2. Case study 2: 24th November 2015

On 24th November 2015, a low pressure system was located over Iceland. The associated frontal system passed Germany on this day from the north-west. Ice clouds



(a) 26th April 2013

(b) 24th November 2015

Figure 4.1.: Corrected reflectance from MODIS on TERRA. The blue circle depicts the modelled domain (see also Section 4.3) which is centered at Jülich Research Center and has a diameter of 220 km. The overpass over the domain center takes place daily at around 10:46 UTC. The pictures are created with <https://worldview.earthdata.nasa.gov>.

descended in the course of the day and increasingly intense precipitation occurred (first in the form of rain and later also as snow). The corrected reflectance in Figure 4.1b shows a widespread cloud band of medium opacity in the modelled area.

For the 24th November 2015, data from the TRIPLE-frequency and Polarimetric radar Experiment for improving process observation of winter precipitation (TRIPEX) are available. During TRIPEX, vertically pointing radars at three frequencies (within the X-,Ka- and W-Band) were located at the Jülich Research Center.

### 4.3. Domain

The model runs performed during this work are setup with domains in shape of a circle. The center of these domains is located at the Jülich Research Center at  $50.91^{\circ}N$  and  $6.41^{\circ}E$ . All runs have a domain with a diameter of 220 km with an effective resolution of 624 m (the boundary of this domain is shown with the blue circle in Figure 4.1). The simulation of this domain is performed with a timestep of 3 s. The control runs additionally have a refined inner-domain with a diameter of 175 km, an effective resolution of 312 m and a timestep of 1.5 s. This domain is forced by the outer domain with a one-way nesting approach. The model uses the SLEVE coordinates

(see also Section 2.1.1) as a vertical grid with 150 model levels and a model top at 21 km.

## 4.4. Initialization and boundary data

The simulation of the 26th April 2013 is initialized at 04:00 UTC. The initialization, as well as the lateral boundary data, is derived from the operational COSMO-DE forecast runs for the 26th April 2013 in the same way as in Heinze et al. (2016). For the case study of the 24th November 2015, model output from the Integrated Forecasting System (IFS) of the European Centre for Medium-Range Weather Forecasts (ECMWF) has been used for initialization and lateral boundary data generation. Here the initialization takes place at 00:00 UTC.

For setting the lower boundary conditions, the *globecover2009* dataset (which e.g. contains the surface albedo and the land sea fraction) as provided by the German Weather Service (DWD) is taken and gridded to the domain.

## 4.5. Overview of the model runs

Table 4.1 gives an overview over the model runs which appear in this work. To increase readability in the following each of the model runs are referred by the specifier of this table.

The configuration of the model runs is described in the following. *SB control* is the control run with the SB-scheme, *P3 control* the control run with the P3-scheme. The suffixes *April* or *Nov.* are used, additionally, to clarify if the case study of the 26th April 2013 or the 24th November 2015 is considered. For the November case, additionally, sensitivity runs (modified formulation of microphysical processes) have been performed. One of them is the *P3 satad* run in which the saturation is adjusted before each call of the P3-scheme in the same way it is done for the SB-scheme. *P3 no aggreg.* and *P3 100000timesaggregation* are model runs with the P3-scheme in which the aggregation is turned off completely respectively the rates are multiplied by  $10^5$ . As aggregation just reduces  $N_i$  as described in Section 2.4.2.4 the before mentioned changes are just applied to this process rate. Similar to this approach, in the *Nov. SB no snowslf* run the self-collection of the snow category is turned off, that means  $N_s$  is not reduced by the self-collection routine. For the *Nov P3 nsub0* run, the change in  $N_i$  due to sublimation in the P3-scheme is deactivated, while for the *Nov. SB nssub* run a change in  $N_i$  due to sublimation of the snow category in the SB-scheme similar to the approach in the P3-scheme is applied. While in the control runs of the SB-scheme, there is no change of  $N_s$  applied, when sublimation occurs  $N_s$  is decreased by  $q_{ssub} \cdot N_s \cdot q_s^{-1}$ , where  $q_{ssub}$  is the process rate, decreasing  $q_s$  due to sublimation. In that way  $q_{norm}$  of the snow category is held constant.

Table 4.1.: List of performed model runs. See a more detailed description of the sensitivity runs in the text.

case	micro- physics scheme	domains (diameter[km] /resolution[m])	specifier	deviations from the control run
26.04.2013	P3	(220km/624m); (175km/312m)	<i>April P3 control</i>	-
26.04.2013	SB	(220km/624m); (175km/312m)	<i>April SB control</i>	-
24.11.2015	P3	(220km/624m); (175km/312m)	<i>Nov. P3 control</i>	-
24.11.2015	P3	(220km/624m)	<i>Nov. P3 satad</i>	saturation adjustment called (before the microphysics scheme)
24.11.2015	P3	(220km/624m)	<i>Nov. P3 no aggreg</i>	aggregation turned off
24.11.2015	P3	(220km/624m)	<i>Nov. P3 100000times aggregation</i>	aggregation rates scaled by the factor $10^5$
24.11.2015	P3	(220km/624m);	<i>Nov P3 nisub0</i>	process rates of $N_i$ due to sublimation turned off
24.11.2015	SB	(220km/624m); (175km/312m)	<i>Nov. SB control</i>	-
24.11.2015	SB	(220km/624m)	<i>Nov. SB no snowslf</i>	self-collection within the snow category turned off
24.11.2015	SB	(220km/624m)	<i>Nov. SB nssub</i>	process rates decreasing $N_s$ applied, so that $q_{norm}$ is constant during sublimation

## 5. Results and discussion

In this chapter, the results from the various simulations are compared and evaluated using the forward-operated model output from the PAMTRA radar simulator. Furthermore, idealized PAMTRA simulations, investigating the multi-frequency space are described.

We start with a comparison of the forward-operated output of ICON (with using either the P3- or the SB-scheme) with cloud radar observations in the time-height space (Section 5.1). The concept of fall streaks used in this work is discussed in Section 5.2, before the relative importance of pure ice cloud processes in the control runs is analyzed in Section 5.3. Further investigations of pure ice cloud processes are carried out by sensitivity runs in Section 5.4. Based on these sections we will look at the precipitation field in Section 5.5 and analyze the differences therein, which results in the use of the different microphysics schemes and the sensitivity studies. The last Section (5.6) shows approaches to use synergistic effects between model and multi-frequency radar observations by exploring the microphysical processes discussed in the first sections of this chapter.

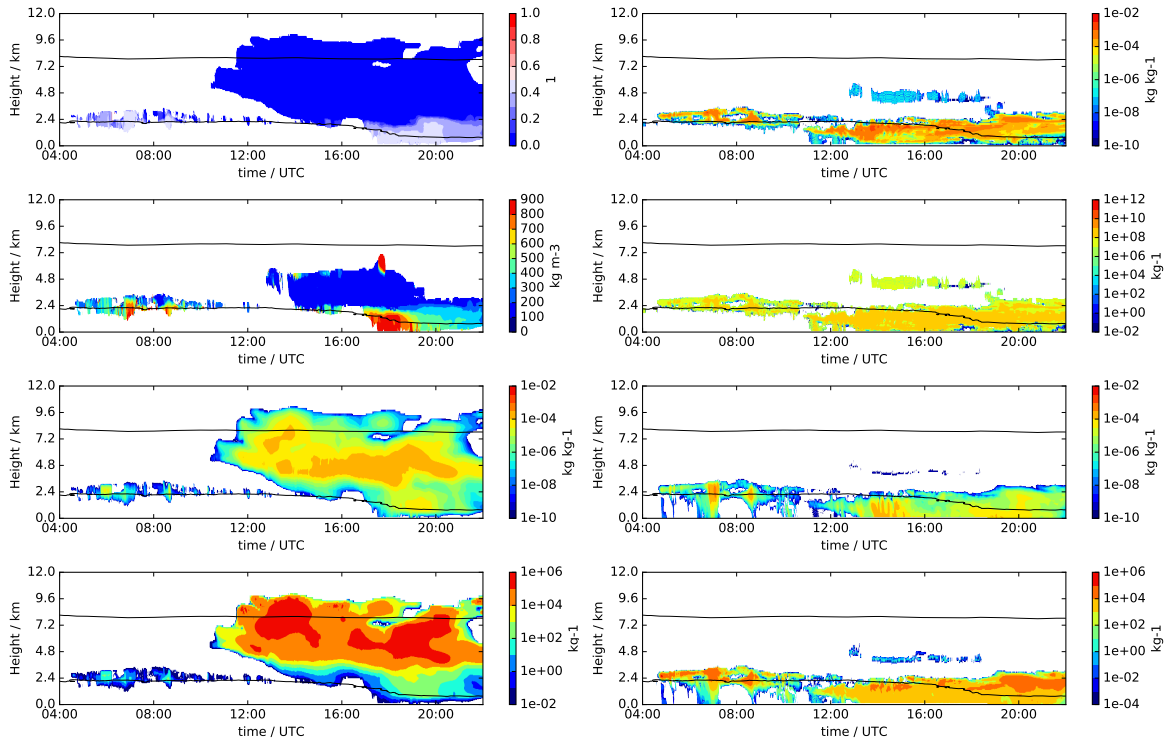
### 5.1. Model-observation comparison in the time-height space

In the beginning of the analysis, a first comparison between the model output and the observations is drawn by looking at  $Z_e$  (forward operated and measured) in the time-height space. This perspective will provide an overview of the hydrometeors throughout the whole vertical extension of the troposphere. With the help of joint histograms the deviations of the forward operated and the observed  $Z_e$  are analyzed in more detail. Time-height plots of the reflectivity weighted sedimentation velocity  $v_{sed,Z}$  (in case of the model runs) or the Doppler velocity ( $v_{doppler}$ ; in case of the observations) allow a first overview of the particle growth, which occurs mainly from cloud top to the cloud base in the here considered cloud.

#### 5.1.1. 26th April 2013

For the April case, measurements by a cloud radar, which was placed near the village of Krauthausen, and a column of the model output corresponding to this location are used. The cloud radar is of the type MIRA-35 (the name indicates the frequency of the radar beam which is 35.5 GHz) from the company *METEK* and was operated by the Leibniz-Institute for Tropospheric Research (TROPOS). The observational dataset is calibrated and corrected by gas and hydrometeor attenuation. Variables

## 5. Results and discussion



(a) Cold phase variables:  $F_{rim}$ ,  $\rho_{rim}$ ,  $q_i$  and  $N_i$  (from top to bottom) (b) Warm phase variables:  $q_c$ ,  $N_c$ ,  $q_r$  and  $N_r$  (from top to bottom)

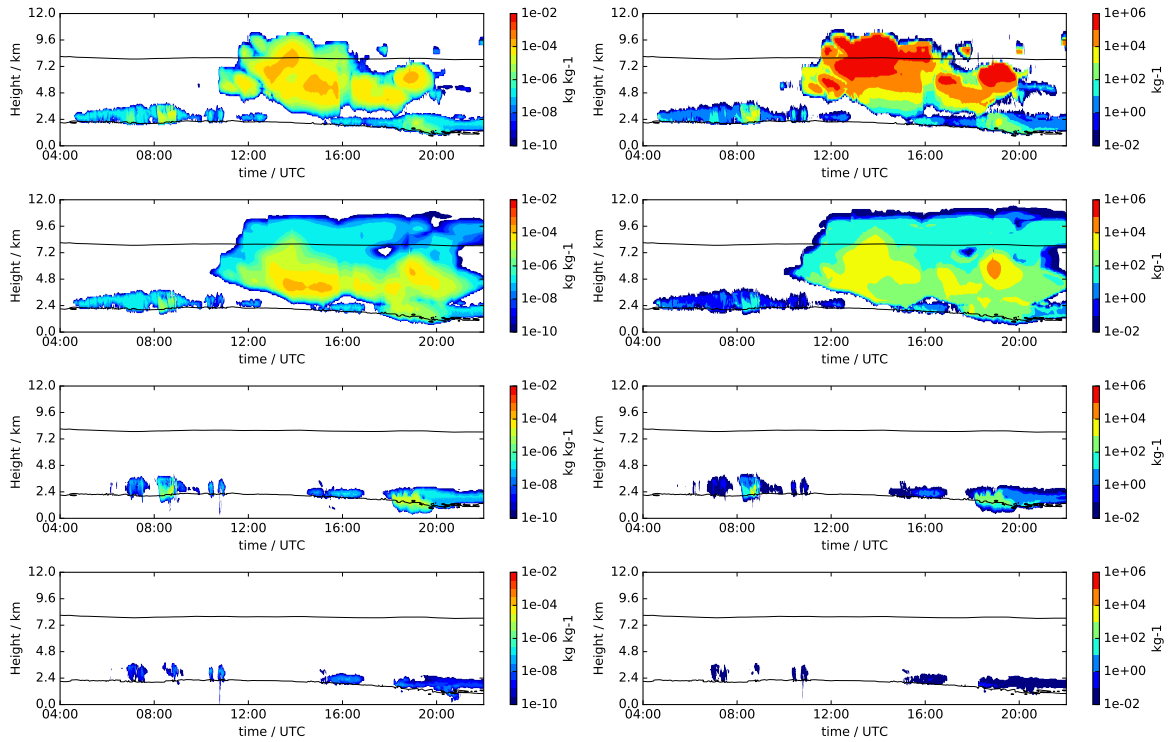
Figure 5.1.: Prognostic variables of the *P3 control* run and variables calculated from them, which are relevant for the PAMTRA run.

from the ICON output and variables calculated from them (as e.g.  $F_{rim}$ ), which are used for the PAMTRA simulations, are shown in Figure 5.1 for the P3-scheme and in Figure 5.2 for the SB-scheme.

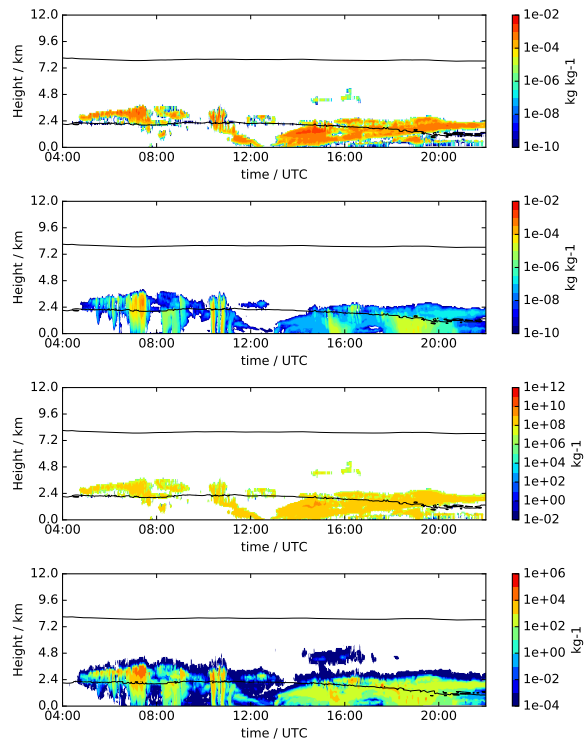
Figure 5.3 shows  $Z_e$  in the time range from 04:00 UTC to 22:00 UTC and the height range from 0 to 12 km above the cloud radar. The forward operated  $Z_e$  is overlaid by the 0°C and the -40°C isoline. Only values of  $Z_e$  exceeding -40 dB<sub>Z</sub>, which is close to the sensitivity limit at 12 km are shown. In addition to the forward operated  $Z_e$  from the outer domain (Figures 5.3b and 5.3d), the forward operated  $Z_e$  from the nested domain is also shown (Figures 5.3c and 5.3e). There are only minor differences, in the clouds simulated in the two domains, which are mainly due to the different magnitude of resolved turbulence. These emerge mostly in the low level (liquid phase) clouds.

In general, the cloud structure (which can be estimated by the times and heights where  $Z_e$  exceeds -40 dB<sub>Z</sub>) is well matched with both microphysics schemes and for both domains, except for the last hours where the model misses clouds in many heights. In each run, a low level cloud is present in the morning hours which is mostly composed of liquid hydrometeors (apparent in the Figures 5.1 and 5.2 for the outer domain). Around 11:00 UTC a cloud consisting of unrimed ice particles occurs at heights around 5 km and increases in depth in the following hours. Considerable amount of rime

5.1. Model-observation comparison in the time-height space



(a)  $q$  of cloud ice, snow, graupel and hail (b)  $N$  of cloud ice, snow, graupel and hail  
(from top to bottom) (from top to bottom)



(c) From top to bottom:  $q$  of cloud water and rain,  $N$  of cloud water and rain

Figure 5.2.: Prognostic variables of the *SB control* run for the April case.

does not occur until liquid hydrometeors appear at heights significantly above the freezing level (which decreases in the course of the day due to the frontal passage) at around 18:00 UTC. This late occurrence of rime is apparent in both schemes (see Figures 5.1 and 5.2). In the SB-scheme, the rimed mass goes mostly into the graupel category (which is prescribed with a lower effective density than the hail category). The P3-scheme shows high values of  $\rho_{rim}$  in the timespan between about 17:00 and 19:00 UTC with values of  $F_{rim}$  which do not exceed 0.5 (see Figures 5.1 and 5.2).

Keeping the good agreement of the cloud structure in mind, we should also consider the difference in the  $Z_e$  values. Both schemes show short precipitation events in the morning hours apparent in high  $Z_e$  values near the ground, which are rarer in the observations. In contrast, too few precipitation events occur with both schemes in the afternoon. These are also of a too low intensity in the run with the P3-scheme.

In the higher levels, where the cloud is almost completely composed of unrimed ice, the SB-scheme shows too high reflectivity values. This overestimation is especially obvious at heights around 5 km. A more detailed analysis of these deviations is possible by looking at the Contoured Frequency by Altitude diagrams (CFADs) (see Figure 5.4).

The left side of Figure 5.4 shows histograms of observed and forward operated  $Z_e$  from model output with the P3- and the SB-scheme (from top to bottom). The bin widths of the histogram are  $2 dB_Z$  for the  $Z_e$  axis and 240 m and 300 m for the height axis for the forward operated respectively modeled data. In the middle of each plot the counts in each height-reflectivity bin are shown as a joint histogram (which is then called CFAD). On top of that, a one-dimensional histogram of  $Z_e$  is shown, which uses the same x-axis as the CFAD below. On the right side of the CFAD another one-dimensional histogram depicts the number of pixels where  $Z_e$  exceeds  $-40 dB_Z$  in the specific height bin (using the same y-axis as the CFAD). All three histograms are normalized by the total number of pixels in the considered time-height space. As a result, the integral of the histogram over height and  $Z_e$  is equal to one only if  $Z_e$  of the pixels at each time step and height exceeds  $-40 dB_Z$ . The same holds true also for the two-dimensional histograms.

In order to aid the comparison between the different CFADs, the right side of Figure 5.4 depicts the difference of counts in each height-reflectivity bin compared to observations in the middle of each plot and an overlay of the one-dimensional histograms on the sides (red for the forward operated  $Z_e$ , blue for the observed  $Z_e$ ). In the joint histograms red pixels express that more counts of the forward operated  $Z_e$ , than the observed  $Z_e$ , can be found in the specific  $Z_e$ -height bin. Blue pixels indicate that more pixels of the observed  $Z_e$  are assigned to that bin.

Figure 5.4a shows an almost steady increase of the observed  $Z_e$  with decreasing height which is only interrupted at a height of approximately 5 km where the cloud base lies at around 12:00 UTC. This local peak of reflectivity is even more pronounced in  $Z_e$  corresponding to the P3 and the SB-scheme (see Figures 5.4b and 5.4d). There both schemes show an overestimation of  $Z_e$ . Above this height the forward operated  $Z_e$  of the P3-scheme lies in the right order of magnitude (with a slight overestimation at altitudes about 9 km).  $Z_e$  from the SB-scheme is up to 10 dB higher than the observations at heights above 4 km.

Below 4 km counts are found in a wider range of  $Z_e$  for the observations. This spread is also visible in the forward operated  $Z_e$ , but a cluster of a high number of counts are found there at around  $-10 \text{ dB}_Z$  for the P3-scheme and about  $-30 \text{ dB}_Z$ ,  $-10 \text{ dB}_Z$  and  $10 \text{ dB}_Z$  for the SB-scheme.

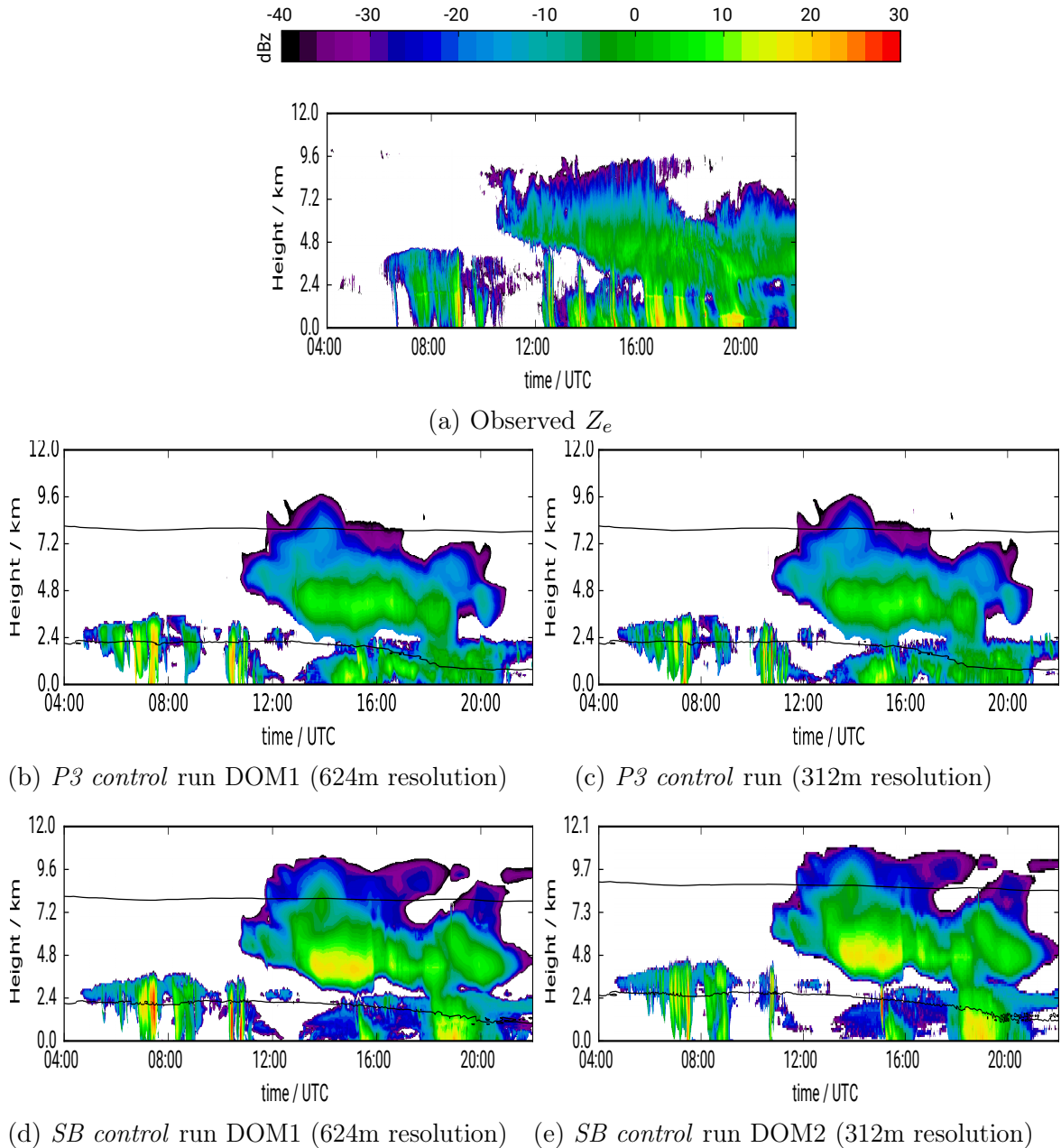


Figure 5.3.: Time-height plot of observed  $Z_e$  (with MIRA-35 near the village of Krauthausen) and forward operated  $Z_e$  (using the column of the model output closest to the before mentioned site). The  $0^\circ\text{C}$  and the  $-40^\circ\text{C}$  isolines are shown by black lines.

The three datasets have their maximum frequency at very different reflectivities. The peak in observations at  $-5 \text{ dB}_Z$  is much larger than either the SB-scheme ( $-25 \text{ dB}_Z$ ) or the P3-scheme ( $-17 \text{ dB}_Z$ ). Comparing the one-dimensional histograms of  $Z_e$  we see a maximum of occurring  $Z_e$ -counts at  $-25 \text{ dB}_Z$ ,  $-17 \text{ dB}_Z$  and  $-5 \text{ dB}_Z$  from the SB-scheme, the P3-scheme and the observations. A faster decay is also evident after reaching this maximum value in the observations as compared to the model output.

The one-dimensional histogram on the right side can be interpreted as the frequency of clouds occurring at a specific height. This data shows an overestimation of the cloud-top height by the SB-scheme and a relative good agreement between observation and both schemes at middle and lower heights can be observed.

As we have seen in Section 2.5,  $Z_e$  is very sensitive to the size of the scatterer. Thus, a mismatch of  $Z_e$  between model and observation can be caused by a mismatch of the characteristic size of the hydrometeor distribution. A good indication for the size of the hydrometeors is  $v_{sed}$  in modal space or  $v_{doppler}$  as a radar observable (see Figure 5.5). It should be noted, that the depicted  $v_{doppler}$  in Figure 5.5a relates to the actual velocity of all hydrometeors (including the advection by vertical wind speed) towards the radar while  $v_{sed,Z}$  in the Figures 5.5b and 5.5c is derived from the bulk properties of the hydrometeor categories denoted above the plot. Here the 6th moment of the size distribution is used in order to have a quantity close to the contribution of the hydrometeor category to  $v_{doppler}$ . An exact match of these properties can therefore only be expected for the same size distribution if the hydrometeors are small (to fulfill the Rayleigh criterion), spherical and liquid phase. Nevertheless, we will look at some general characteristics of these variables. Figure 5.5a shows vertically orientated areas of increased  $v_{doppler}$  which match the fall streak signatures in Figure 5.4a. In those areas,  $v_{doppler}$  reaches values above  $1 \text{ m s}^{-1}$  at heights above 7 km. Following these fall streaks to the cloud base we can find values of  $v_{doppler}$  exceeding the displayed range of  $2 \text{ m s}^{-1}$ . In contrast a relative steady increase of  $v_{sed,Z}$  appears for the P3 ice category towards the cloud base.  $v_{sed,Z}$  higher than about  $1.5 \text{ m s}^{-1}$  is only reached for areas with a significant rime fraction (compare Figure 5.5b with 5.1).

As the analysis focuses on the unrimed ice phase, Figure 5.5c shows  $v_{sed,Z}$  only for the cloud ice and snow category. Here we see relatively low values of  $v_{sed,Z}$  for the cloud ice, but slightly larger values towards the cloud base. Interestingly  $v_{sed,Z}$  of snow already has high values in the upper part of the cloud (it should be noted, that  $q_s$  and  $N_s$  are very low here) and increases to values over  $1.5 \text{ m s}^{-1}$  at around 3 km height (where considerable  $q_s$  and  $N_s$  are present). This high  $v_{sed,Z}$  together with the relative high  $N_s$  values are responsible for the overestimation of  $Z_e$  at this height. These differences between the SB- and the P3-scheme can be traced back to the implementation of aggregation and sublimation to some degree, as we will see in Section 5.4 for the November case.  $v_{doppler}$  of the later afternoon and below the freezing level should not be compared to the Figures 5.5b and 5.5c as the high values there are presumably due to rimed and liquid phase particles.

In this section, we saw good agreement between model and observations in the cloud structure and reasonable magnitudes of  $Z_e$ . Nevertheless, some significant deviations are obvious at low heights for both schemes and additionally at medium heights for

the SB-scheme concerning  $Z_e$ . Based on the comparison between  $v_{doppler}$  and  $v_{sed,Z}$  the overestimation of  $Z_e$  by the SB-scheme can be suspected in the overestimation of the snow particles size. This hypothesis will be further evaluated by sensitivity runs in Section 5.4 for the November case.

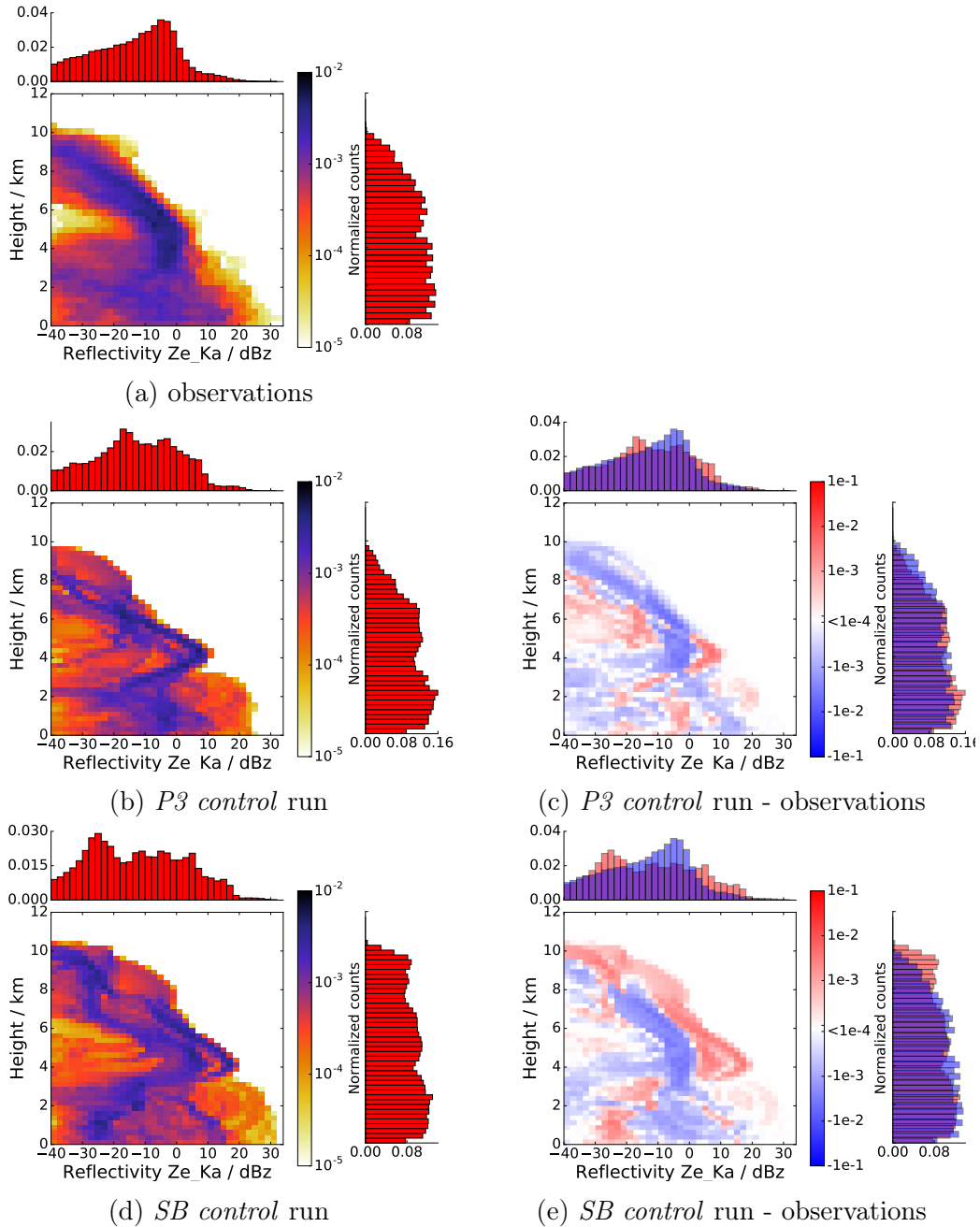
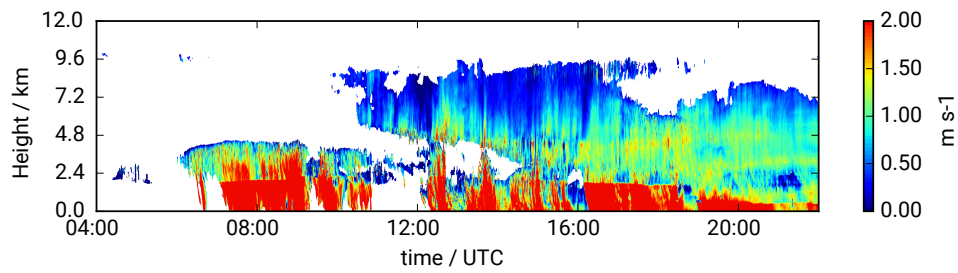
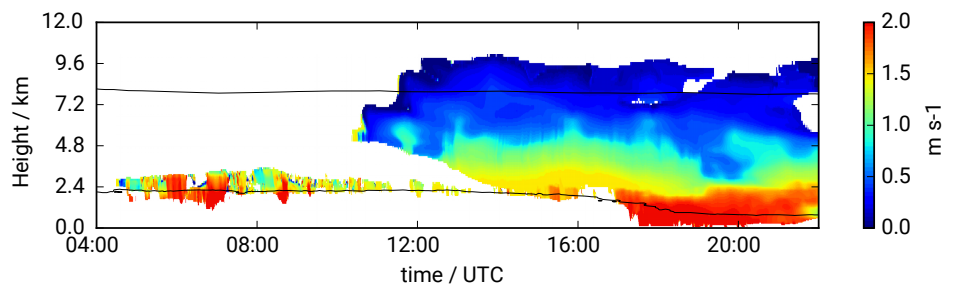


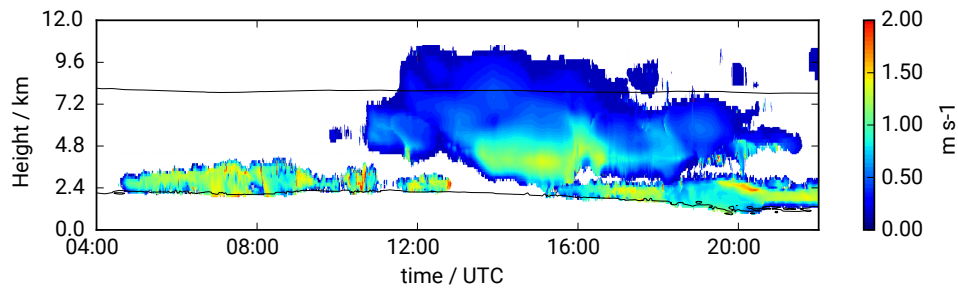
Figure 5.4.: CFADs of observed and forward operated reflectivity of the April case using data from 04:00 UTC to 22:00 UTC. Further explanations of these figures can be found in the text.



(a)  $v_{doppler}$  from cloud radar observations



(b)  $v_{sed,Z}$  of the ice category in the *P3 control* run



(c)  $v_{sed,Z}$  of the cloud ice (top) and snow (bottom) category in the *SB control* run

Figure 5.5.: Time-height plots of observational and model variables linked to the velocity of the hydrometeors (April case). The  $0^{\circ}\text{C}$  and the  $-40^{\circ}\text{C}$  isolines are shown by black lines

## 5.1.2. 24th November 2015

In order to compare the P3- and the SB-scheme against observations in more detail, a second case study is considered in this section. For the November case, observations of a cloud radar (MIRA-36s from *METEK* operating with 35.5 GHz), which was placed at the Jülich Research center, are compared with forward operated values based on the column of the model output which is closest to this location.

The same representation of the data as for the April case is used here. Therefore the methodological description and remarks of the Figures to Section 5.1.1 are not repeated. Figure 5.6 shows the observed and the forward operated  $Z_e$  as a time-height series. The model output was forward operated from runs with the P3-scheme in 612 m (also with saturation adjustment applied) and 312 m horizontal resolution and with the SB-scheme (in both resolutions). MIRA-36s was operated alternating between scanning mode and vertically pointing mode, which is the reason for the data gaps in Figure 5.6a.

In this case, too, the cloud structure is well matched for model runs with both schemes and for both domains. Figure 5.6 shows an underestimation of  $Z_e$  in the morning hours by both schemes before  $Z_e$  increases and a reasonably good agreement with observations is found at of 10:00 UTC. Again the SB-scheme shows higher values of  $Z_e$  compared to the P3-scheme, here especially at heights of 2 to 3 km (compare Figures 5.6b and 5.6e). In this case, the P3-scheme underestimates  $Z_e$  by up to 8 dB, while  $Z_e$  from the SB-scheme is close to  $Z_e$  of the observations.

Increased spectral width, which is observed in the observations in the afternoon (not shown), indicates the occurrence of riming. This occurrence of riming is also visible in the model output (see Figures A.1 and A.3), where values of  $F_{rim}$  significantly exceeding 0 in the P3-scheme and a substantial amount of graupel (hail is almost not existent) in the SB-scheme can not be found in the morning hours but is present in the afternoon.

The differences between the run with the lower and the run with the higher resolution are small (compare Figure 5.6b with Figure 5.6c and Figure 5.6e with Figure 5.6f). Some deviations occur after 16:00 UTC where the areas of high  $Z_e$  have a slightly different structure. These deviations are probably due to more small scale turbulence in the higher resolution run. Due to these small deviations, only the lower resolution run is used in the following, in order to be able to make a comparison with sensitivity runs, which are only available on the low resolution.

Larger differences are apparent when comparing the *P3 control* run with the *P3 satad* run. For the latter one,  $Z_e$  is substantially larger from about 16:00 UTC to 17:00 UTC and values of  $Z_e$  exceeding 20 dB<sub>Z</sub> can be found even at heights of about 5 km. These high  $Z_e$ -values indicate a more convective nature of the cloud at this time and location and can strongly impact the precipitation field. Furthermore,  $Z_e$  is lower at lower heights in the *P3 satad* run compared to the *P3 control* run after around 17:00 UTC which could also be caused by a spatial shift of the clouds between these simulations. The full-domain precipitation field (which can be found in Section 5.5) can be used to investigate if the differences of the different model runs are due to

different physical representations in the different schemes or merely due to a spatial mismatch.

The CFAD of the observed  $Z_e$  (see Figure 5.7a) depicts a steady increase of  $Z_e$  with decreasing height (except below 1 km height). The one-dimensional histogram above this CFAD shows a broad left-skewed distribution of  $Z_e$  with the maximum of counts around  $0 \text{ dB}_Z$ . The one-dimensional histogram on the right of the CFAD show maximum occurrence of clouds around 4 km.

$Z_e$  from the P3-scheme also shows a steady increase of  $Z_e$  (see Figure 5.7b). The corresponding CFAD, showing the deviations from the observations (see Figure 5.7c), reveals an underestimation of the maximum  $Z_e$ -values for the P3-scheme, which is expressed in the blue pixels at the highest occurring values of  $Z_e$  at each height. These indicate less counts in the forward operated  $Z_e$  than in the observed  $Z_e$  at a specific height. The area of blue pixels furthermore increases with decreasing height which implies an underestimation of the increase of  $Z_e$  as particles fall. For the *P3 satad* run (see Figures 5.7d and 5.7e), the underestimation is smaller at heights below 4 km, because between 16:00 UTC and 17:00 UTC the reflectivity values are increased in comparison to the *P3 control* run. At heights of about 3 km and below 1 km the maximal occurring  $Z_e$  values from the *P3 control* run are even higher than the maximum  $Z_e$  values from the observations (see red pixels at these heights in Figure 5.7e). A better agreement of the SB-scheme with the observations than the P3-scheme is shown in Figure 5.7f. The alternating pattern of blue and red pixels at heights above 6 km means that the forward operated  $Z_e$  is of the right magnitude. In the two kilometers below, we can see a small underestimation of  $Z_e$ , whereas the red area below 2 km indicates an overestimation.

The distribution of the one-dimensional histograms of  $Z_e$  of both schemes reveal a maximum occurrence of  $Z_e$  at values, that are much smaller than the maximum corresponding to the observations. Furthermore, the distributions of the forward operated  $Z_e$  are right-skewed, so that the occurrence of high  $Z_e$ -values is rarer than in the observations (more pronounced for the P3-scheme). With the help of the histogram on the right side of the CFAD from the P3- and the SB-scheme (see Figures 5.7c and 5.7g), the overestimation of the cloud top by both schemes and the slight underestimation of the occurrence of clouds at lower heights by the SB-scheme becomes apparent.

We want to look in this section also at the variables which are linked to the velocity of the particles (see Figure 5.8). Figure 5.8a shows values of  $v_{doppler}$ , that are below  $0.5 \text{ m s}^{-1}$  at heights around 8 km and increase with decreasing altitude. Values close to or above  $2 \text{ m s}^{-1}$  of  $v_{doppler}$  in the afternoon are probably due to the presence of liquid or rimed particles. The P3 ice category (which is the only category present until 12:00 UTC; see Figure A.1) underestimates the sedimentation velocity at almost the complete first half of the day (keep in mind the limited comparability of this comparison, which results in the impact of different hydrometeor types and the vertical motion to  $v_{doppler}$ , discussed in Section 5.1.1). This underestimate indicates that the particle are too small, which, in turn, could be an explanation for the underestimation of  $Z_e$  by the P3-scheme.

5.1. Model-observation comparison in the time-height space

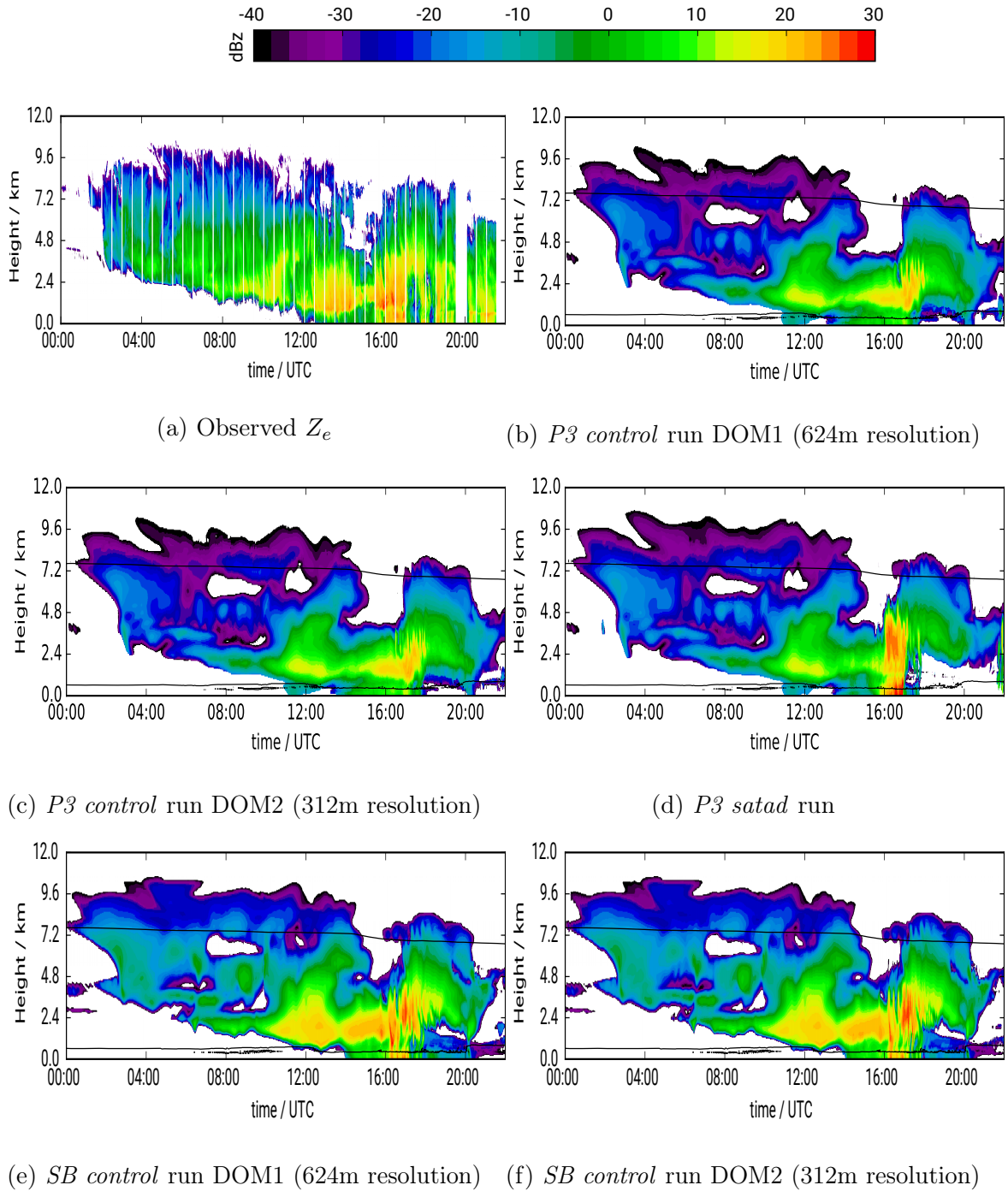
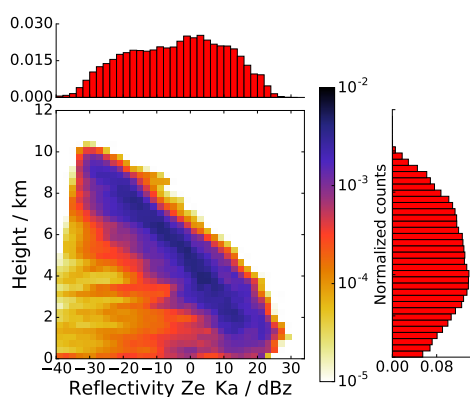
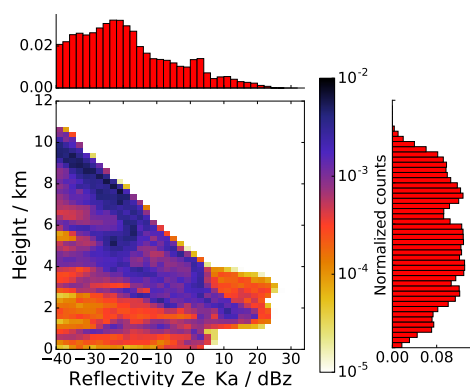


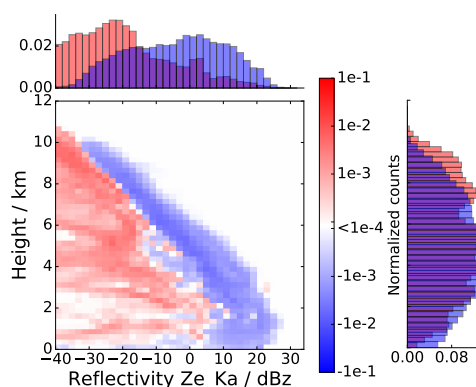
Figure 5.6.: Time-height plot of observed (with MIRA-36-s at the Jülich Research center) and forward operated  $Z_e$  (using the column of the model output closest to the before mentioned site). The  $0^\circ\text{C}$  and the  $-40^\circ\text{C}$  isolines are shown by black lines.



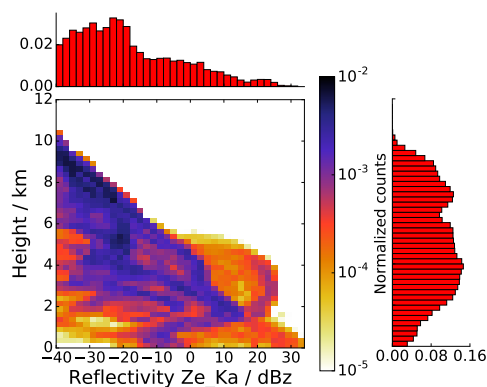
(a) observations



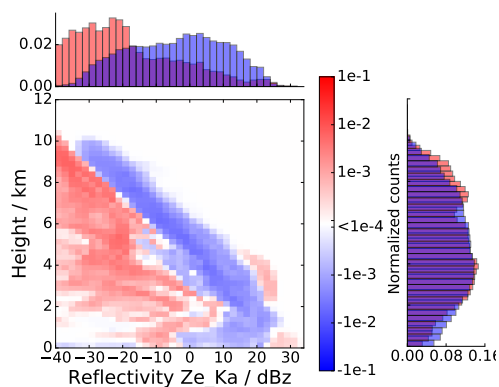
(b)  $P3$  control run



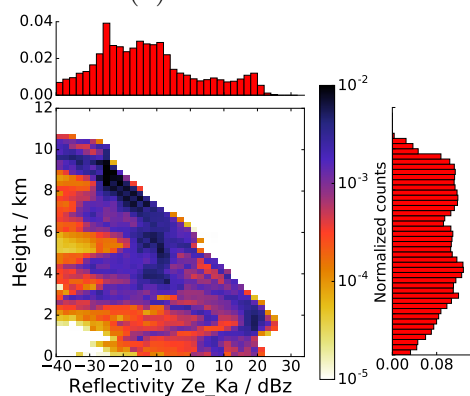
(c)  $P3$  control run - observations



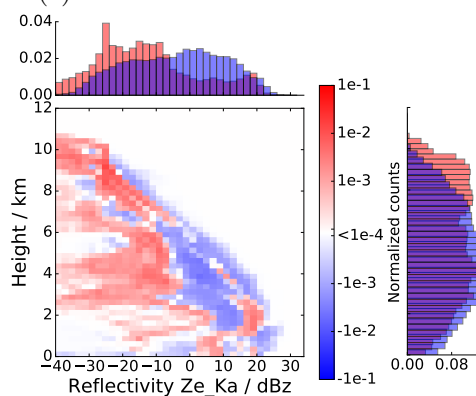
(d)  $P3$  satad run



(e)  $P3$  satad run - observations



(f)  $SB$  control run



(g)  $SB$  control run - observations

Figure 5.7.: CFADs of observed and forward operated  $Z_e$  of the November case.

Values of  $v_{sed,Z}$  significantly higher than  $0.5 \text{ m s}^{-1}$  occur between 07:00 UTC and 10:00 UTC at heights of around 4 km and also at heights below 5 km from around 11:00 UTC to 12:00 UTC and over a longer time range in the afternoon. In the first timespan, the increased values of  $v_{sed,Z}$  correspond to small numbers of  $N_i$  (see Figure A.1a). None of the microphysical processes were found to be responsible for this decrease of  $N_i$  (see Section 5.3), therefore this change is likely a result of advection of inhomogeneities in the cloud. This hypothesis is supported by a vertical slice of  $N_i$  and  $q_i$  of the *P3 control run* at a height of 2470 m at 12:00 UTC (see Figure A.4).

In the second timespan,  $q_i$  increases, connected to strong depositional growth in the layers above (see Section 5.3). The high  $v_{sed,Z}$  values in the afternoon appear together with increased  $F_{rim}$  and are of a similar magnitude to the highest  $v_{doppler}$  values but about 2 hours later than these.

Comparing  $v_{sed,Z}$  of the unrimed SB-categories with the P3 ice category at times and heights with  $F_{rim}$  close to 0 reveals similar characteristics as already found in Section 5.1.1 (see Figure 5.8c). Note also the relatively high  $v_{sed,Z}$  values of the snow category near the cloud top (where  $q_s$  and  $N_s$  is relatively small). The maximum of  $v_{sed,Z}$  between 07:00 UTC and 10:00 UTC at heights of around 4 km also appears with the SB-scheme and is associated with  $v_{sed,Z}$  values up to  $1.5 \text{ m s}^{-1}$ . Around 12:00 UTC and about 2 km,  $v_{sed,Z}$  of snow reaches values up to  $2 \text{ m s}^{-1}$  which is significantly higher than  $v_{sed,Z}$  of the P3-scheme in this region. In contrast to the P3-scheme, the hydrometeors do not reach the ground despite this high sedimentation velocity. We will look in more detail at this time range in Section 5.4 to understand where these differences originate.

As in the April case, there was good agreement of the cloud structure between model runs with both schemes; but in the November case, both schemes underestimate  $Z_e$  in a longer timespan in the morning. The P3-scheme shows an underestimation of  $Z_e$  also in the second part of the day, while the SB-scheme is closer to the measurements. The *P3 satad* run shows enhanced  $Z_e$  values, most likely connected to the stronger latent heat release and the consequential higher buoyancy production. A significant amount of rain is seen at heights above 2 km already at 14:00 UTC, in the *P3 satad* run, while this is not the case for the *P3 control* run (compare Figures A.1 and A.2). The latent heat release can originate from the applied saturation adjustment and lead to the increased amount of liquid hydrometeors at heights above the  $0^\circ\text{C}$  isotherm and enhance riming. In addition, strong differences in the time-height plots of  $v_{sed,Z}$  were observed, which are investigated further in Sections 5.3 and 5.4.

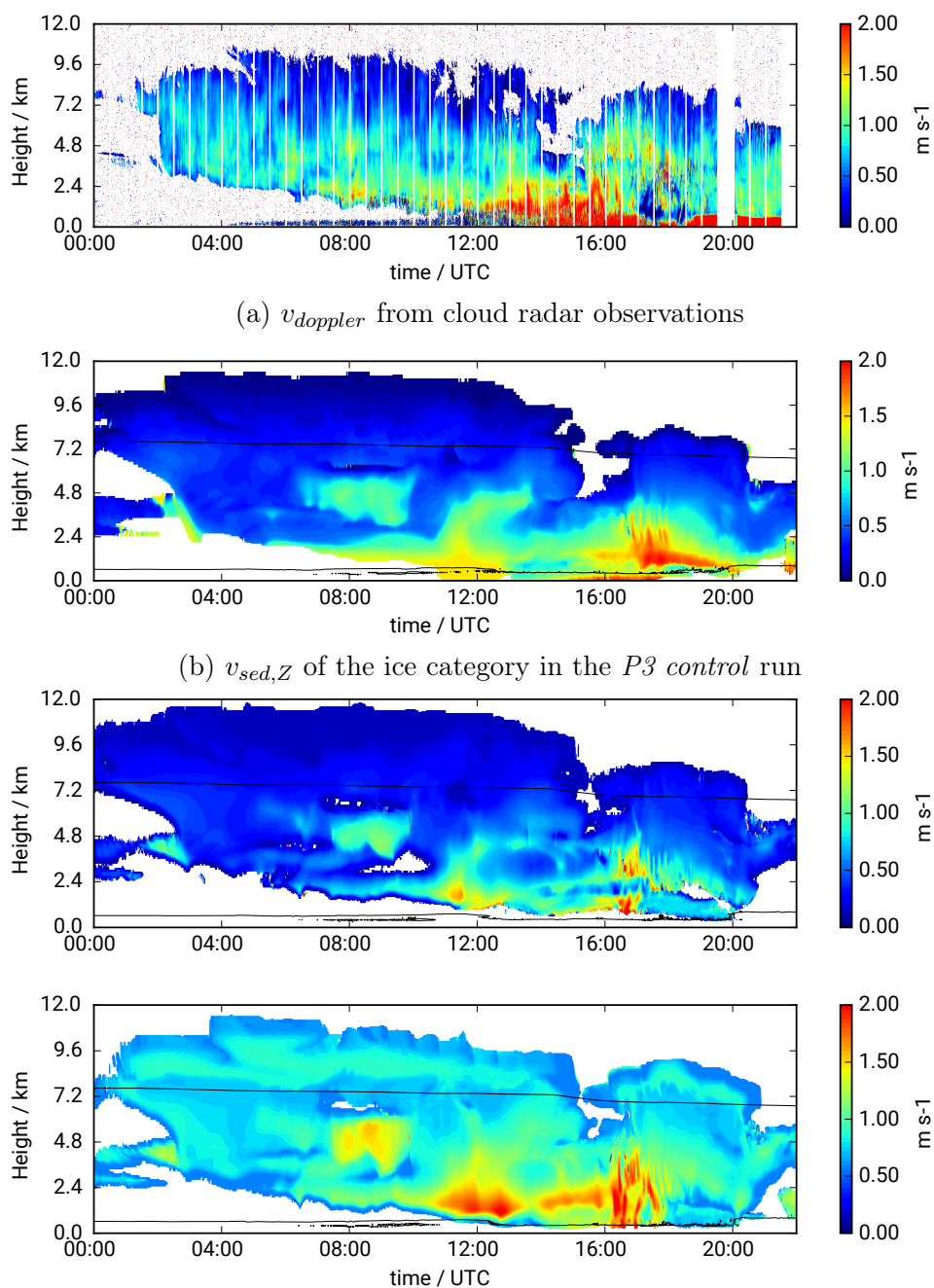


Figure 5.8.: Observational and model variables which are linked to the velocity of the hydrometeors (November case). The  $0^{\circ}\text{C}$  and the  $-40^{\circ}\text{C}$  isolines are shown by black lines

## 5.2. Fall streaks

In this section, the concept of Lagrangian fall streaks (Pfitzenmaier et al., 2017) is introduced and in the following sections they are applied to the time-height radar data. By analyzing the fall streaks, the growth processes of the ice particles can be tracked in time. This method provides an advantage over analyzing the time-height plots, because the microphysical processes can be separated from advection.

Fall streaks in radar data, which manifest themselves through the contrast in the microphysical properties, have been found already by Marshall (1953). Pfitzenmaier et al. (2017) proposed a definition based on particle dynamics, which can also be applied to model output in a straightforward manner. This definition tracks the particle populations following their own motion, which is a superposition of advection and sedimentation. The application of this definition to radar measurements has just recently become possible through radars which can retrieve the full 3D wind. The radars used for the measurements in this work, however, do not have the capability to retrieve the full 3D wind. As a result, the method is not applicable to the observations. However, the 3D wind is known for the model and consequently the method is applied here, but only to the model data.

Pfitzenmaier et al. (2017) formulated the time displacement  $\Delta t(z)$  at the height  $z$  due to the antenna elevation,  $v_{doppler}$  of the particle populations as well as the standard deviation of  $v_{doppler}$ . Because only vertically pointing radars are analyzed in this study the contribution to  $\Delta t(z)$  resulting from the antenna elevation does not have to be taken into account. Moreover the turbulence contribution, which would require an estimate of the standard deviations of the Doppler velocities, is neglected for simplicity here.

In the adaption of this fall streak concept to this work  $v_{doppler}$  is replaced by the sum of  $v_{sed,Z}$  (here: negative for movements towards the ground) and  $w$ , so that  $\Delta t(z)$  can be written as follows:

$$\Delta t(z) = \frac{\Delta h}{v_{sed,Z}(z, t) + w(z, t)} \cdot \frac{|u_h(z, t)| - |u_h(z - \Delta h, t)|}{|u_h(z, t)|} \quad (5.1)$$

Here  $|u_h|$  is the absolute value of the horizontal wind vector and  $h$  is the model output layer thickness. The first term can be interpreted as the time, that a particle population needs to move to the next model layer. The second term describes the horizontal displacement of the particle population relative to the mean displacement of the whole cloud in this time. This relative displacement scales with the wind shear at the given height. In this work the lowest model output level where  $N$  exceeds  $10^{-10} \text{ kg}^{-1}$  is chosen as the starting point for the fall streak calculations. Based on this starting point the fall streak is calculated towards the cloud top by adding  $\Delta t(z)$  at each model output level and moving to the next higher model output level. In that way, the time relative to the start of the fall streak calculation can be determined for each model output level (see an example for the fall streak calculated from the cloud base at 12:00 UTC for the *Nov. P3 control* run in Table 5.1). If there are multiple layers of clouds (with the definition  $N > 10^{-10} \text{ kg}^{-1}$ ),  $\Delta t(z)$  is set to zero for the levels with  $N < 10^{-10} \text{ kg}^{-1}$ . It should be noted, that  $v_{sed,Z}(z) + w(z) \approx 0$  leads to very large

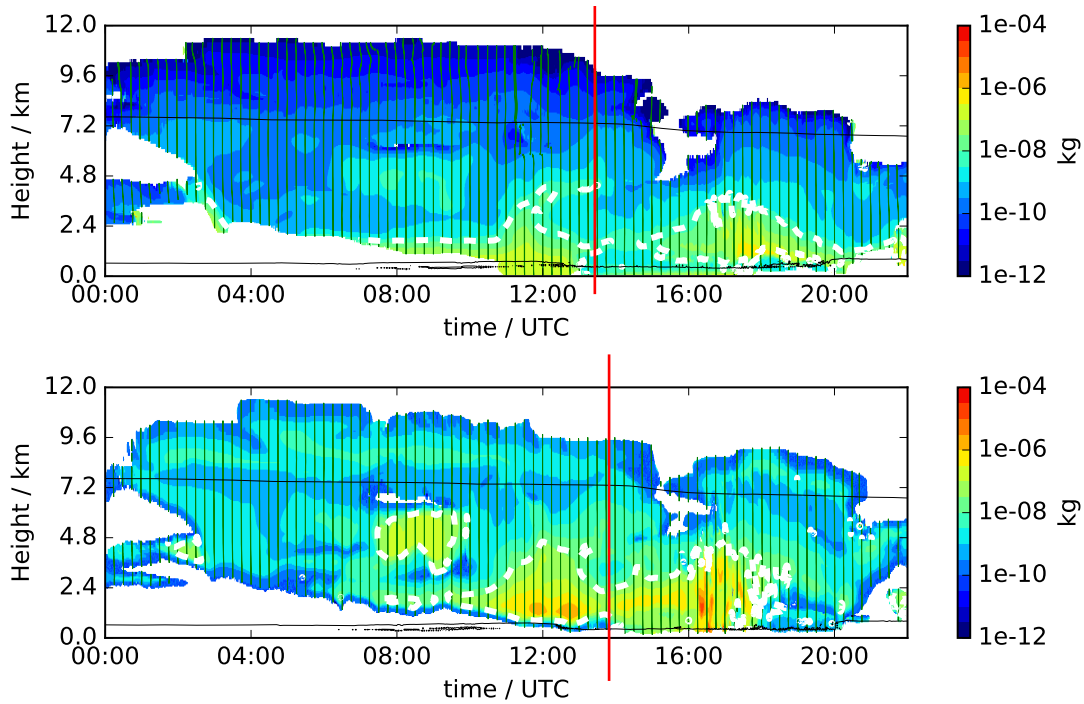


Figure 5.9.: Normalized mixing ratio ( $q_{norm}$ ) of the ice category in the *P3 control* run (top) and of the snow category in the *SB control* run (bottom). The dark green lines depict the fall streaks calculated from the cloud base every 15 minutes as described in Section 5.2, the dashed white line surrounds the area with  $DWR_{Ka-W} > 2\text{dB}$  (calculated taking all categories into account) and the vertical red line indicates the time where riming becomes relevant. As in previous figures, the  $0^\circ\text{C}$  and the  $-40^\circ\text{C}$  isolines are shown by black lines

values of  $\Delta t(z)$ , which results in discontinuities or an almost horizontal line of the fall streak e.g. for the particles, which reach the cloud base at 12:00 UTC, this occurs at heights of 6300 m (see last three lines in Table 5.1). These discontinuities can also be seen at later time steps from 12:00 UTC to 13:00 UTC for the P3 ice category in the *Nov. P3 control* run (see Figure 5.9 (top)) but not for the SB snow category in the *Nov. SB control* run (see Figure 5.9 (bottom)), which can be explained by the small  $v_{sed,z}$  values of the P3 ice category. For the fall streaks, where these discontinuity do not occur, the time relative to the start of the fall streak calculation lies in the order of a few tens of seconds and the fall streaks appear as almost straight lines for the relatively long time range displayed e.g. in Figure 5.9.

The method to retrieve fall streaks in the way described above relies on strong assumptions. The one which is most important for this work is the homogeneity within the cloud and of the dynamical conditions. We saw already some indication for inhomogeneity in the analyzed time-height space in the Section 5.1.2 and therefore the fall streaks which are indicated in the next sections should be analyzed carefully.

Table 5.1.: Example of a fall streak calculation (visualized also by the dark green line in Figure 5.9 (top)) for a particle population, which reaches the cloud base at 12:00 UTC and a height of 150 m. Here values of  $v_{sed,Z}$  are negative for a movement towards the ground.

time relative to the start of the fall streak calculation / s	height / m	$v_{sed,Z}(z, t)$ $+w(z, t)$ / $\text{m s}^{-1}$	$ u_h(z, t) $ $- u_h(z - \Delta h, t) $ / $\text{m s}^{-1}$	$ u_h(z, t) $ / $\text{m s}^{-1}$	$\Delta t(z, t)$ / s
0	150	-1.41	-0.22	8.38	0.92
0.92	200	-1.37	0.97	9.35	-3.77
-2.86	250	-1.34	0.73	10.05	-2.71
-5.57	300	-1.33	1.80	11.85	-5.72
-11.29	350	-1.30	0.59	12.43	-1.82
...					
-44.48	6250	0.01	0.005	16.71	1.26
-43.22	6300	0.005	0.14	16.85	79.94
36.73	6350	0.007	0.20	17.12	82.75
...					

### 5.3. Pure ice-cloud growth-processes in the November case

In the previous sections, we have seen large differences in  $v_{sed,Z}$  between the P3- and the SB-scheme, which can be a result of different process formulations within the schemes. In order to detect potential deficiencies in these process formulations, the reason for these deviations must be analyzed. Therefore, the relative importance of the processes in the model runs from the November case is investigated in this section. This investigation is limited to growth processes (because of their superior importance for the formation of precipitation) in pure ice clouds (to reduce the number of processes happening simultaneously).

Due to the latter restriction on pure ice cloud processes, the analysis should be carefully separated between the time ranges where rimed particles are present and where they are not. In the absence of riming, backtracing of the pure ice cloud processes to the different implementations of these processes is easier than in the presence of riming.

In order to compare the processes, which manifest themselves either through a change in  $q$  or  $N$ , the change in the normalized mixing ratio  $q_{norm}$  ( $\Delta q_{norm}$ ) induced by each considered process is analyzed. The calculation of  $\Delta q_{norm}$  is illustrated in Equation 5.2, where  $\Delta q_{proc}$  and  $\Delta N_{proc}$  are the process rates by which the prognostic variables  $q$  and  $N$  change within a fixed time period.

$$\Delta q_{norm} = \frac{q + \Delta q_{proc}}{N + \Delta N_{proc}} \quad (5.2)$$

To facilitate a further interpretation of  $\Delta q_{norm}$  we first look at the absolute values of  $q_{norm}$  (Figure 5.9). The relationship between  $q_{norm}$ ,  $v_{sed,Z}$ ,  $DWR_{Ka-W}$  and  $DWR_{X-Ka}$  is shown in Figure A.6 which allows us to link this analysis to the comparison of  $v_{sed,Z}$  in Section 5.1.2 and the approaches in which  $DWR$  is used as a size indicator in Section 5.6.2.

As we are interested in processes that are relevant for precipitation,  $\Delta q_{norm}$  is only analyzed for the SB snow category (which represents all precipitating particles in the ice phase in the absence of rimed particles) and not for the SB cloud ice category. Moreover the snow category dominates over the ice category in terms of contribution to  $Z_e$  (Figure A.5) and the mass mixing ratio at heights lower than 4 km (Figure A.3a).

Because  $v_{sed,Z}$  is a monotonic function of  $q_{norm}$  (see Figure A.6),  $q_{norm}$  in Figure 5.9 shows similar features as  $v_{sed,Z}$  in Figure 5.8. Therefore no further comparison between the P3 ice category and the SB snow category is made here. Just the general appearance of larger  $q_{norm}$  in the SB snow category should be noted. The fall streaks appear almost as straight vertical lines in Figure 5.9 due to the long time range depicted here. This allows us to analyze the evolution of  $q_{norm}$  mainly as a function of height.

Figure 5.10 shows  $\Delta q_{norm}$  induced by the main processes which occur in pure ice clouds. Those are aggregation, deposition, sublimation and sedimentation (the resulting change in  $q_{norm}$  by these processes are referred by  $\Delta q_{norm,aggr}$ ,  $\Delta q_{norm,depos}$ ,  $\Delta q_{norm,subl}$ ,  $\Delta q_{norm,sedi}$ ). The top row of Figure 5.10 depicts the different impacts of aggregation on  $q_{norm}$  between the two microphysics schemes. In the P3-scheme,  $\Delta q_{norm,aggr}$  is always positive (which is obvious when considering that aggregation only reduces  $N_i$  in the P3-scheme) and affects  $q_{norm}$  only very slightly. In the SB-scheme, aggregation has a larger impact on  $q_{norm}$  and can either decrease or increase  $q_{norm}$  of the snow category. Near the cloud top, aggregation leads to a first appearance of snow particles. This is followed by an increase of  $q_{norm}$  by collision of two cloud ice particles which form a snow particle and a collection of cloud ice particles by snow particles. The collision of two cloud ice particles can also decrease  $q_{norm}$  of the snow category if the resulting snow particle is smaller than  $q_{norm}$  (which occurs mainly in the middle heights of the cloud). Near the cloud base, self-collection of snow is the dominating aggregation process which leads to a rapid increase of  $q_{norm}$  there.

The middle row of Figure 5.10 shows  $\Delta q_{norm,depos}$  and  $\Delta q_{norm,sublim}$  (these two processes can be plotted in one panel because depositional growth only happens for  $RH_i > 100\%$  and sublimation only happens for  $RH_i < 100\%$ ). Depositional growth increases  $q_{norm}$  in both schemes. In the upper part of the cloud  $\Delta q_{norm,depos}$  is of similar magnitude for both schemes, in the lower part of the cloud  $\Delta q_{norm,depos}$  takes higher values for the SB snow category than for the P3 ice category. This can be explained by the higher mean mass of the SB snow category which leads to a more effective depositional growth (see Equation 2.7). Due to the different implementations  $q_{norm}$  stays constant for a sublimating population of ice hydrometeors in the P3-scheme while  $q_{norm}$  is decreased through sublimation in the SB-scheme. This is especially important near the cloud base where sublimation leads to a rapid decrease in  $q_{norm}$  of the SB snow category.

The last process considered is sedimentation. Sedimentation, as implemented in both microphysics schemes, leads to a flux of  $q$  and  $N$  to the next-lowest model level. The effect of sedimentation is mimicked by Equation 5.3, which allows a fast estimation of the change to  $q_{norm}$  through sedimentation. Here the index  $z_i$  stands for the current model output level while  $z_{i+1}$  refers to the value from the model output level above.

$$\Delta q_{norm,sedi}(z_i) = \frac{q_{z_i} + \{[v_{sed,q,z_{i+1}} - w_{z_{i+1}}] q_{z_{i+1}}\} - \{[v_{sed,q,z_i} - w_{z_i}] q_{z_i}\}}{N_{z_i} + \{[v_{sed,N,z_{i+1}} - w_{z_{i+1}}] N_{z_{i+1}}\} - \{[v_{sed,N,z_i} - w_{z_i}] N_{z_i}\}} \quad (5.3)$$

The estimate of  $\Delta q_{norm,sedi}$  is shown in the lowest row in Figure 5.10. This estimate shows an alternating pattern of positive and negative values of  $\Delta q_{norm,sedi}$  for both schemes. In the upper part of the cloud, a decrease of  $q_{norm}$  due to sedimentation is prevalent (which is more pronounced in the SB-scheme). Near the cloud base  $\Delta q_{norm,sedi}$  has positive values which are several orders of magnitude higher/ of the same order of magnitude than the growth mechanisms discussed before for the P3-scheme and the SB-scheme, respectively.

None of the processes above analyzed change  $q_{norm}$  only in the absence of riming, but their relative importance on  $q_{norm}$  can only be estimated in the presence of riming when the riming processes are included in the analysis (which is not the case here).

In this section, we saw that all of the processes, contribute significantly to the variation of  $q_{norm}$  in the SB-scheme. In contrast, aggregation is not important in the P3-scheme for the here considered variables and sublimation does not decrease  $q_{norm}$ . These differences can explain the lower  $q_{norm}$  and  $v_{sed,Z}$  of the P3 ice category compared to the SB snow category, as we saw at the beginning of this section and in Section 5.1.2. As we have seen major differences relating to aggregation and sublimation between the two microphysics schemes, those processes are analyzed in the next section with sensitivity runs. The variation of  $q_{norm}$  in Figure 5.9 can not be fully explained by the contributions to  $\Delta q_{norm}$  by the processes analyzed in Figure 5.10 (even for the period where riming does not happen and primary ice formation can is not expected). This fact suggests than inhomogeneities in the cloud field (or secondary ice formation in the case of the SB-scheme) are present.

## 5.4. Sensitivity runs concerning pure ice-cloud processes in the November case

We saw in the last section that the importance of the different pure ice-cloud growth processes varies to a large extent between the two considered schemes. This section analyzes model runs, which were performed with modified formulations of the growth processes (in the following referred as sensitivity runs) discussed above (see Section 4.5 for a description of the applied changes). The goal is to gain further insights about, what portion of the difference in  $q_{norm}$  between the two schemes can be assigned to the particular process formulation.

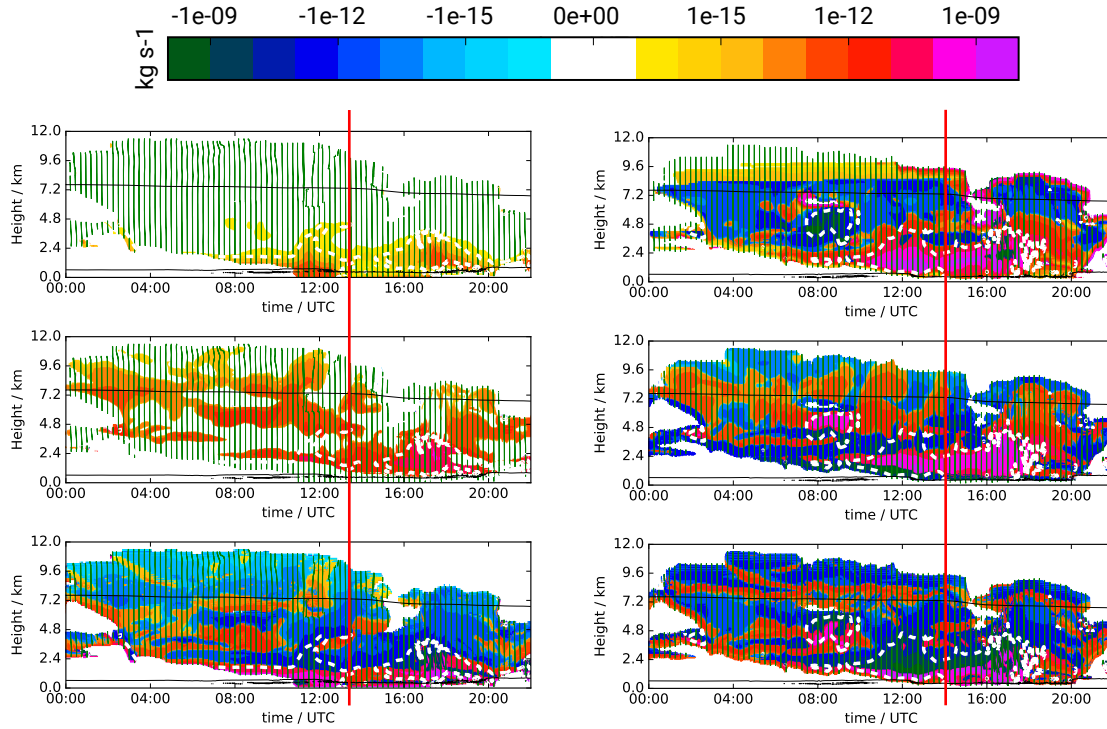


Figure 5.10.: Changes in  $q_{norm}$  ( $\Delta q_{norm}$ ) through aggregation (top row), deposition and sublimation (second row) and sedimentation (lowest row). On the left side  $\Delta q_{norm}$  is shown for the ice category in the *P3 control* run and on the right side for the snow category in the *SB control* run. The overlaid lines depict the same features as in Figure 5.9.

For the analysis, we look at time-height data of  $v_{sed,Z}$  and CFADs. The time range of this analysis is limited from 10:00UTC to 16:00UTC. The first hours of the simulations are excluded because there was no significant increase of  $q_{norm}$ , which can be traced back to the processes considered in Section 5.3. Data after 16:00UTC is not considered here, because of the impact of processes connected to riming (which are excluded in the analysis) becomes increasingly larger. Figure 5.12 shows  $v_{sed,Z}$  of the *P3 control* run and several sensitivity runs. Here  $v_{sed,Z}$  is chosen as a size indicator because it is sensitive to  $q_{norm}$  over a wide range and directly comparable to Figure 5.8.

$v_{sed,Z}$  corresponding to the *P3 noaggregation* (Figure 5.11b) run is hard to distinguish from  $v_{sed,Z}$  from the *P3 control* run (Figure 5.11a; minor differences occur at low heights around 16:00 UTC). This similarity of the model runs is consistent with the previous section, where we saw only a weak effect of aggregation on  $q_{norm}$ . If the aggregation rates are scaled up by the factor  $10^5$ , as done in the *P3 100000timesaggregation* run,  $v_{sed,Z}$  increases significantly (Figure 5.11c). It should be noted, that the limiter of  $D_{mean}$  (and therefore also the limiter of  $v_{sed,Z}$ ; see also Figure A.6) is reached in the lower part of the cloud in the time range where the particles are completely unrimed

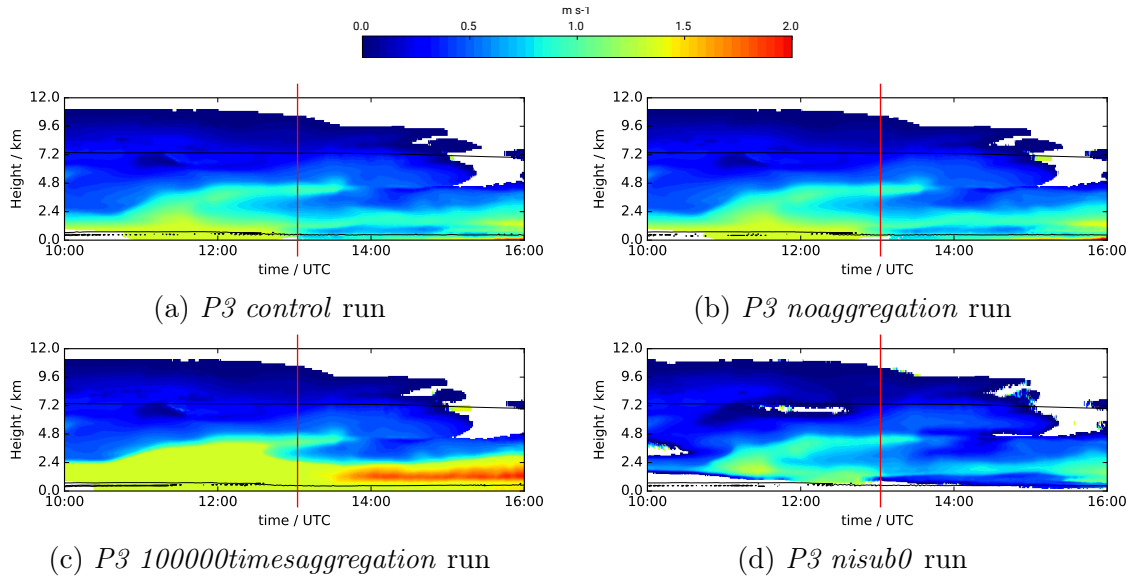


Figure 5.11.:  $v_{sed,Z}$  of the P3 ice category of the *P3 control* run and different sensitivity runs. The vertical red lines indicate the time where riming becomes relevant. The  $0^\circ\text{C}$  and the  $-40^\circ\text{C}$  isolines are shown by black lines

(before about 13:00 UTC). In the time range, where riming occurs,  $v_{sed,Z}$  reaches values up to  $2\text{ m s}^{-1}$ , which suggests that the enhanced aggregation above the liquid layers also enhances riming.

The difference in the implementation of sublimation between the *P3 nisub0* run and the *P3 control* run have a large impact on the  $v_{sed,Z}$  (see Figure 5.11d), too.  $v_{sed,Z}$  is significantly lower at lower heights for the *P3 nisub0* run and also the cloud coverage at heights of 3 km and 7 km is interrupted at around 10:00 UTC and 12:00 UTC, respectively. Moreover in the *P3 nisub0* run no particles reach the ground in this time range, which results from the lower values of  $v_{sed,Z}$ .

Also for the SB-scheme the sensitivity to the implementation of aggregation and sublimation was tested. If self-collection of snow is turned off (as done in the *SB nosnowself* run; see Figure 5.12b)  $v_{sed,Z}$  decreases at heights below 2.5 km and no particles reach the ground from 10:00 UTC to 16:00 UTC.  $v_{sed,Z}$  in the *SB nssub* run depicts changes only at heights below 2 km before the time where riming becomes important. There the particles keep a significant  $v_{sed,Z}$  until they sublimate almost completely ( $v_{sed,Z}$  in areas with  $N_s < 10^{-10}\text{ kg}^{-1}$  is not shown) or reach the ground.

All of the sensitivity tests in this work modify the process rates of the number concentration  $N$ . This change in  $N$  impacts  $Z_e$  in two different ways. On the one hand an increase in  $N$  increases  $Z_e$  because there are more scatterers, on the other hand an increase in  $N$  leads to a decrease of  $q_{norm}$  and thereby indirectly to a decreased  $Z_e$ . The indirect effect is expected to have the larger impact, because of the strong dependency of  $Z_e$  to the size of the scatterers. Analogous statements can be made about a decrease in  $N$  implied by a different implementation of the processes.

The effect of the sensitivity tests on  $Z_e$  is assessed in the following by CFADs using  $Z_e$ -values in the time range from 10:00 UTC to 16:00 UTC (see Figure 5.13).

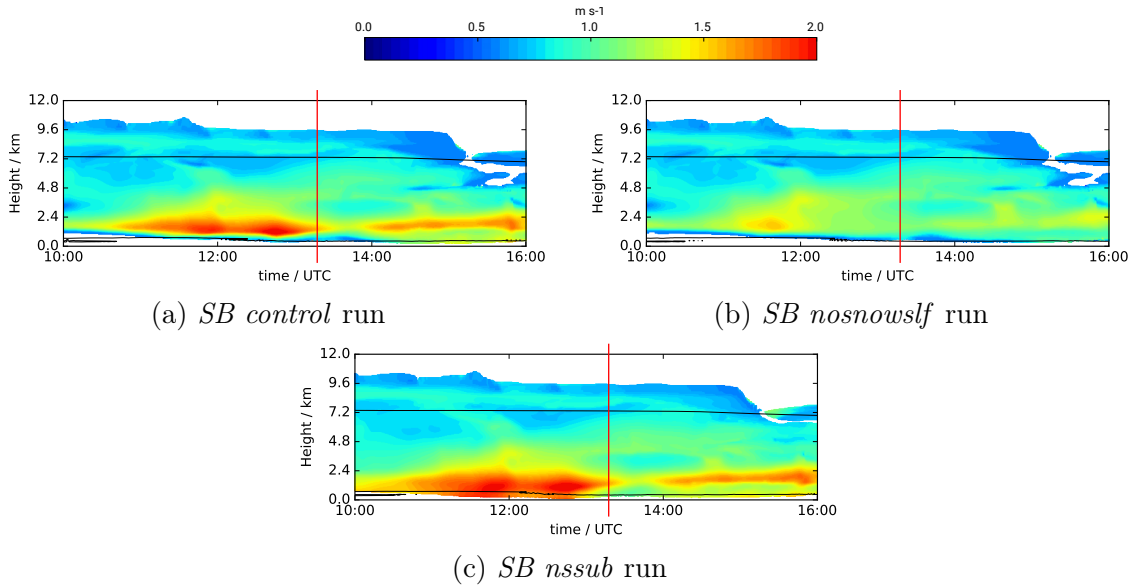


Figure 5.12.:  $v_{sed,Z}$  of the SB snow category in the *SB control* run and different sensitivity runs. The vertical red lines indicate the time where riming becomes relevant. The  $0^\circ\text{C}$  and the  $-40^\circ\text{C}$  isolines are shown by black lines

Increasing the aggregation rates decreases the underestimation of  $Z_e$  by the P3-scheme at heights below 5 km (see Figure 5.13b). The implementation of sublimation, which allows a reduction of  $q_i$ , but not of  $N_i$  leads to an increase in the underestimation of  $Z_e$  in the lowest kilometers and a stronger mismatch of the occurrence of clouds at these heights (see Figure 5.13c). The values of  $Z_e$  of the *SB control* run were already in the right order of magnitude in this time range (see Figure 5.13d). Turning off snow self-collection results from an underestimation of several dB at heights around 2 km (see Figure 5.13e). The *SB nssub* run shows a better match of the occurrence of clouds at the lowest km of the atmosphere, but overestimates  $Z_e$  at those heights (see Figure 5.13f).

Although the main difference between the P3- and the SB-scheme is expected to be in the representation of riming processes, pure ice cloud processes already effect  $v_{sed,Z}$  and  $Z_e$  to a large extent. The results of this section imply that aggregation is underestimated in this case study by the P3-scheme and self-collection in the SB snow category is necessary to get reasonable values of  $Z_e$  at heights near the cloud base. In both schemes, the correct occurrence of hydrometeors near the ground can only be reached when sublimation also decreases  $N$ . Some characteristics of the forward operated  $Z_e$  (such as the steeper slope in the increase of  $Z_e$  with heights in the range of 4 km to 9 km) did not change in the sensitivity runs. As riming does not take place at these heights in this case, the cause of this difference can be expected in the conceptual approaches of the schemes rather than the implementation of the microphysical processes. The main conceptual approaches which are worth considering are the number of unrimed ice categories and the shape of the size distribution.

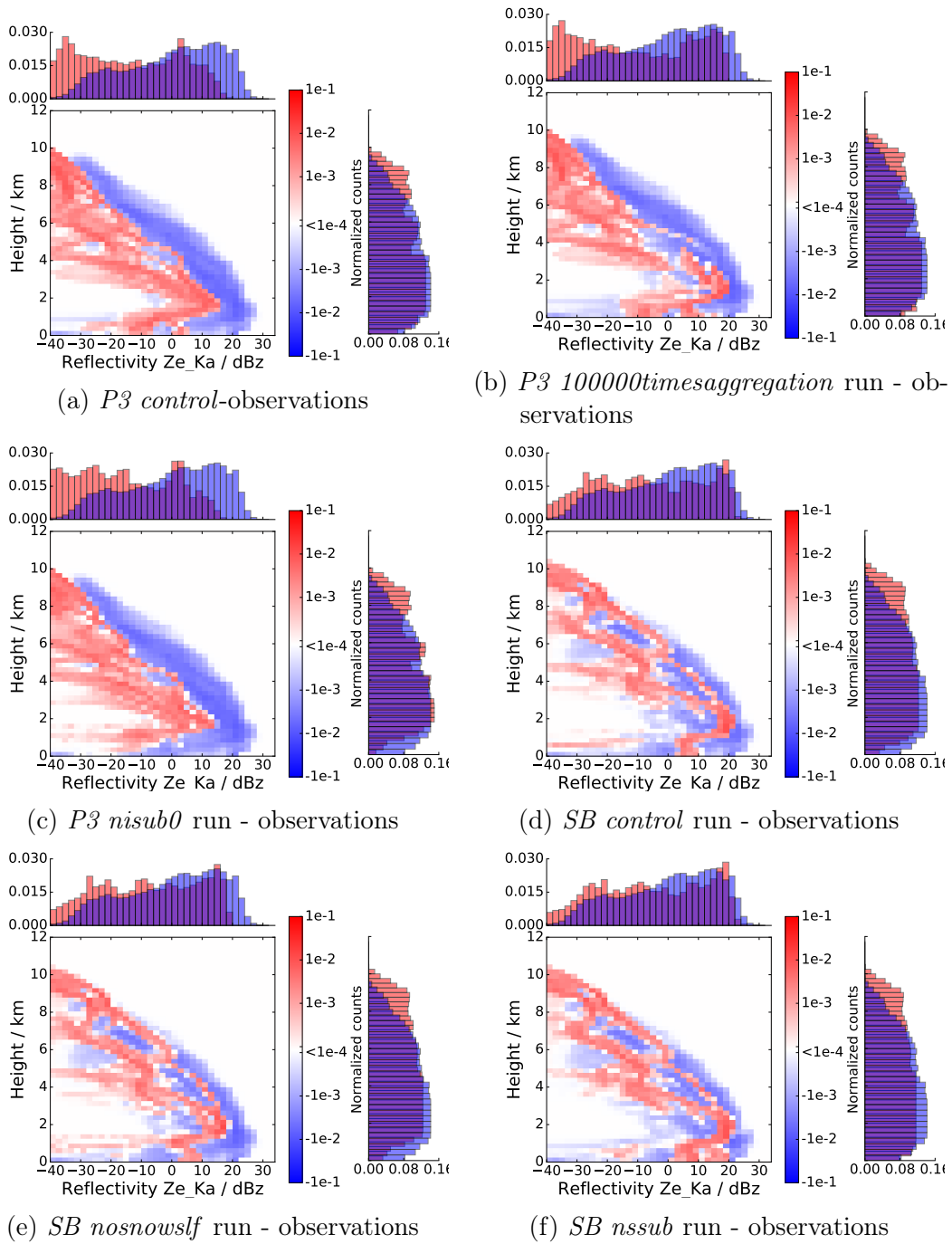


Figure 5.13.: Difference of CFADs of observed and forward operated  $Z_e$  of the November case in the time range from 10:00 UTC to 16:00 UTC including sensitivity runs. For further explanation of the depicted histograms see Section 5.1.1

## 5.5. Precipitation fields

In the previous sections, we saw large differences in the  $Z_e$  values close to the ground between the microphysics schemes, the observations and the sensitivity runs. As  $Z_e$  values close to the ground are strongly correlated to precipitation rates, we also expect large differences in the precipitation field. The selection of the microphysical processes in the previous section was based on their importance for precipitation. Consequently, the investigation of the precipitation field, which is done in this section, takes a key role in this work.

For the actual precipitation field the radar online calibration (RADOLAN) data provided by the German Weather Service (DWD) is used. RADOLAN data is generated based on 17 scanning radars and rain gauge observations covering the whole of Germany. The precipitation field of the model runs is taken directly from the model output.

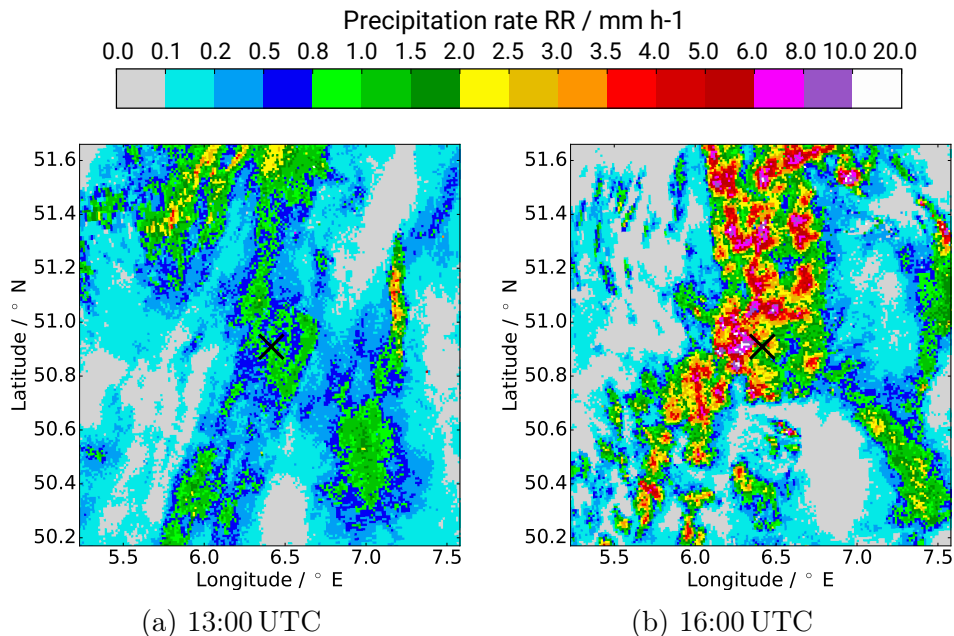


Figure 5.14.: Precipitation field from the RADOLAN dataset. The black cross indicates the cloud radar site and the center of the model domain.

The analysis of the precipitation field focuses on two points in time, which represent different stages of the cloud. At 13:00 UTC, there are no signals of riming visible in the observations and also the model runs in the area close to the cloud radar site (which is indicated by a black cross in the middle of each figure in this section) do not show rimed particles. At 16:00 UTC, strong indications of riming have been found in the cloud radar observations and also all model runs exhibit larger numbers of rimed particles at this time. At 13:00 UTC, the RADOLAN data shows low intensity precipitation (up to a precipitation rate  $RR = 2 \text{ mm h}^{-1}$ ) in the closer environment of the cloud radar and medium rain (up to a  $RR = 6 \text{ mm h}^{-1}$ ) in the outer regions of the displayed field (which covers most of the inner domain in the two-domain

model setups). A large fraction of pixels in the displayed area have precipitation with  $RR > 0.1 \text{ mm h}^{-1}$ . The rain intensifies in the following hours, so that at 16:00 UTC a larger band of medium rain passes the site of the cloud radar from the west to the east. Embedded in this region of medium rain are some locations of heavy rain ( $RR > 6 \text{ mm h}^{-1}$ ; see Figure 5.14).

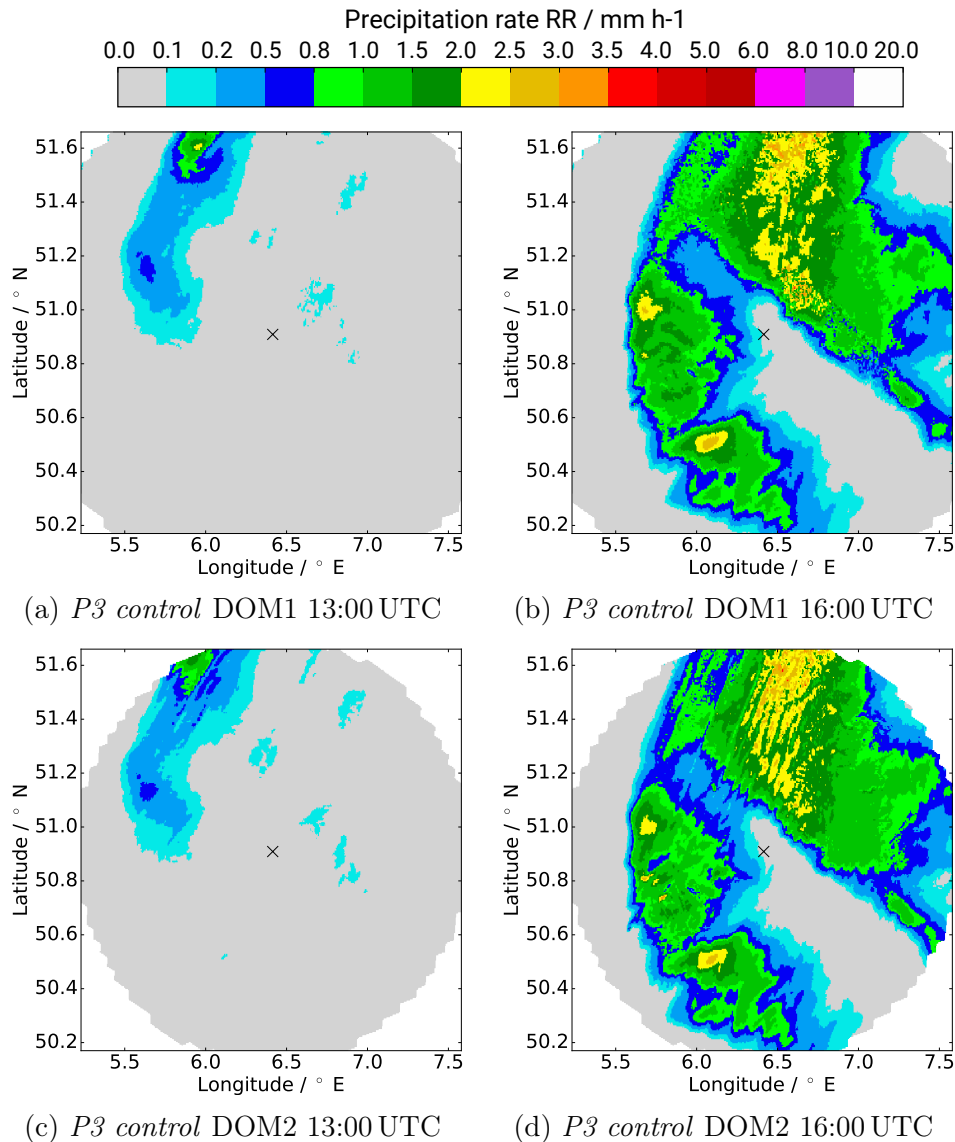


Figure 5.15.: Precipitation field of the *P3 control* run in both domains. The black cross indicates the cloud radar site and the center of the model domain.

Also in the precipitation field of the control runs there are areas of precipitation moving eastwards in the considered time range, but the structure of these areas do not match well with the observations. The *P3 control* run shows a small area where  $RR = 0.1 \text{ mm h}^{-1}$  is exceeded at 13:00 UTC which is mostly accumulated at the north-west of the domain (see Figure 5.15a). Although the *SB control* run shows a larger area with considerable precipitation (not only in the north-west of the domain, but

## 5. Results and discussion

also to the east of the cloud radar site; see Figure 5.16), the precipitation-free region is too large and the intensity is slightly underestimated. At 16:00 UTC, both control runs exhibit a large area with medium precipitation and miss the heavy precipitation almost completely. Compared against each other, the model runs with both schemes lead to a similar spatial pattern of the precipitation area. Only in the southern part of the domain the precipitation area is shifted more to the east in the *P3 control* run compared to the *SB control* run. As there is no clear difference in the horizontal wind field and there are only minor deviations between the different schemes in terms of the vertical wind speed  $w$  (compare the Figures 5.19a and 5.19c), we can expect that this mismatch is due to a faster formation of precipitation in the SB-scheme.

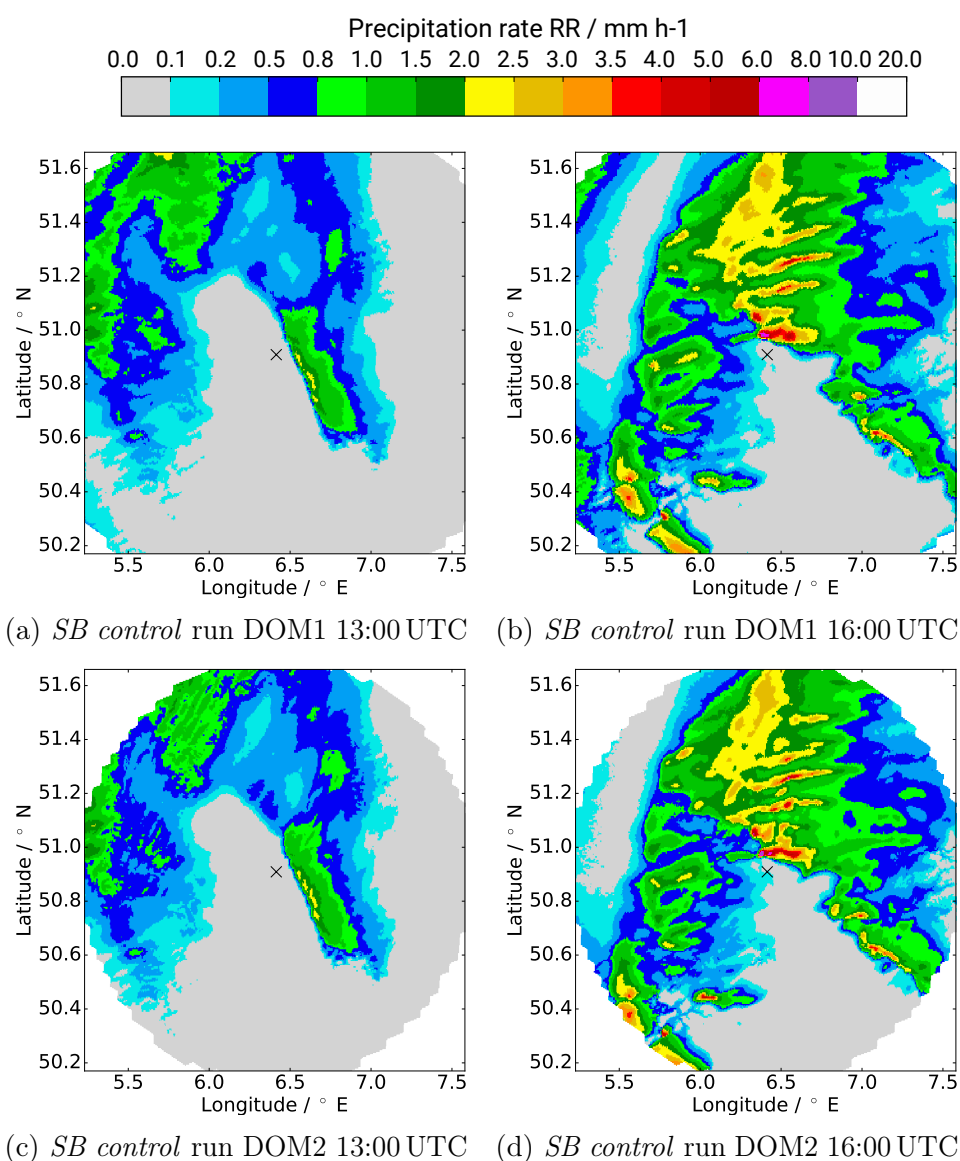


Figure 5.16.: Precipitation field of the *SB control* run on both domains. The black cross indicates the cloud radar site and the center of the model domain.

Going to the precipitation field of the refined domains (see Figures 5.15c, 5.15d, 5.16c and 5.16d) there are hardly any deviations from the low resolution domain visible. The coarse structure and the intensity of the precipitation field remains the same while additional small scale structures appear. These include wave-like features which are especially visible in the north-east in Figure 5.15d and the north-west in Figure 5.16c. These features most probably result in the alternating pattern of up- and downward motion. This pattern can be found in all model runs (see Figure 5.19), but deviations of the structure and strength of  $w$  between the different schemes and configurations are present. The alternating pattern in the precipitation field, which is only seen in the refined domain, can be due to the more pronounced small scale variation of  $w$  in the refined domain (compare e.g. the Figures 5.19a and 5.19b).

Switching on saturation adjustment in the P3-scheme has little impact on the precipitation field at 13:00 UTC, because saturation adjustment affects only grid points where liquid hydrometeors are present. In contrast, the impact on the precipitation field at 16:00 UTC is large. While the precipitation is less intense in the north-west and south of the domain, a medium-sized area of medium to heavy rain is clustered near the center of the domain. This region of increased rain intensity matches spatially with a line of stronger and finer structured updrafts. The mechanisms by which saturation adjustment leads to enhanced  $w$  are explained in Section 2.4.4. Figure 5.19f also depicts deviations of the *P3 satad* run from the *P3 control* run in terms of the horizontal wind field (e.g. a stronger northward component in the line of stronger updrafts). Interestingly, the fine structure in the field of  $w$  are less pronounced and shifted to the west in the *SB control* runs (Figures 5.19c and 5.19d) which also apply saturation adjustment. The modifications which were related to aggregation (the *P3 10000timesaggregation* and the *SB nownowslf* run) lead to significant changes concerning the intensity of the precipitation. The area with  $RR > 1 \text{ mm h}^{-1}$  increases substantially in the *P3 10000timesaggregation* run at 13:00 UTC and more locations with medium rain appear in the south of the domain at 16:00 UTC (see Figures 5.17c and 5.17d). Also the spatial variation in the precipitation rates increases although the deviation in the horizontal and vertical wind field at 4.8 km height is small (e.g. the Figures 5.19a and Figures 5.19e). The changes between the *SB nownowslf* and the *SB control* run are rather subtle and express themselves mostly in the lower maximum precipitation rates.

The sensitivity tests, in which modifications to the implementation of sublimation have been applied, exhibit only minor impacts on the precipitation field (see Figures 5.17e, 5.17f, 5.18c and 5.18d). Although the additional decrease of  $N$  during sublimation (which is the default configuration in the P3-scheme and applied in the *SB nssub* run to the SB snow category) increases the number of grid points where non-zero precipitation rates can be found, they do not exceed values of  $0.1 \text{ mm h}^{-1}$ . These observations account for both points in time and microphysics schemes. It should be noted, that the modification of the sublimation process has just been applied to the snow category in the SB-scheme.

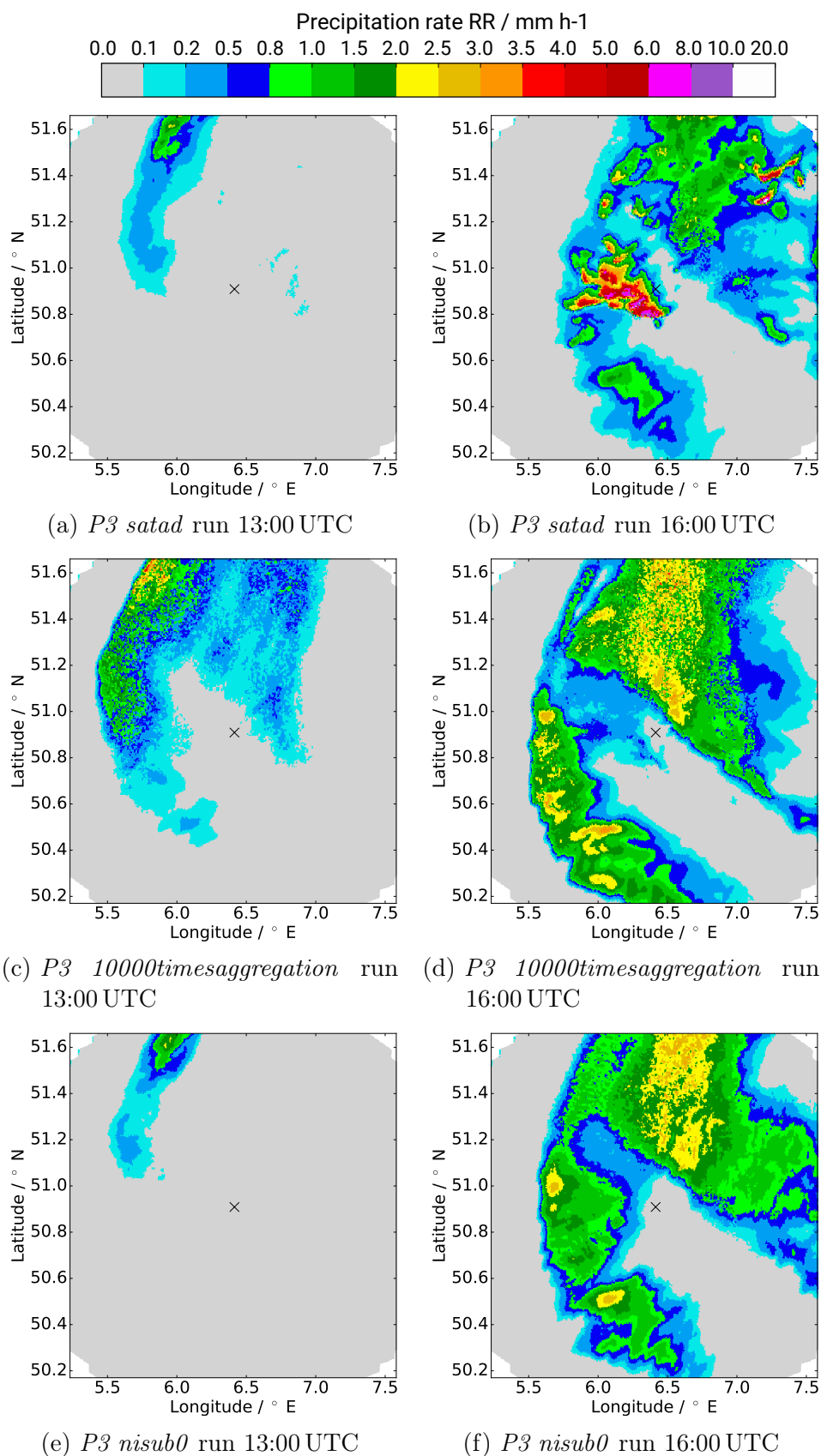


Figure 5.17.: Precipitation field of the P3 sensitivity runs. The black cross indicates the cloud radar site and the center of the model domain.

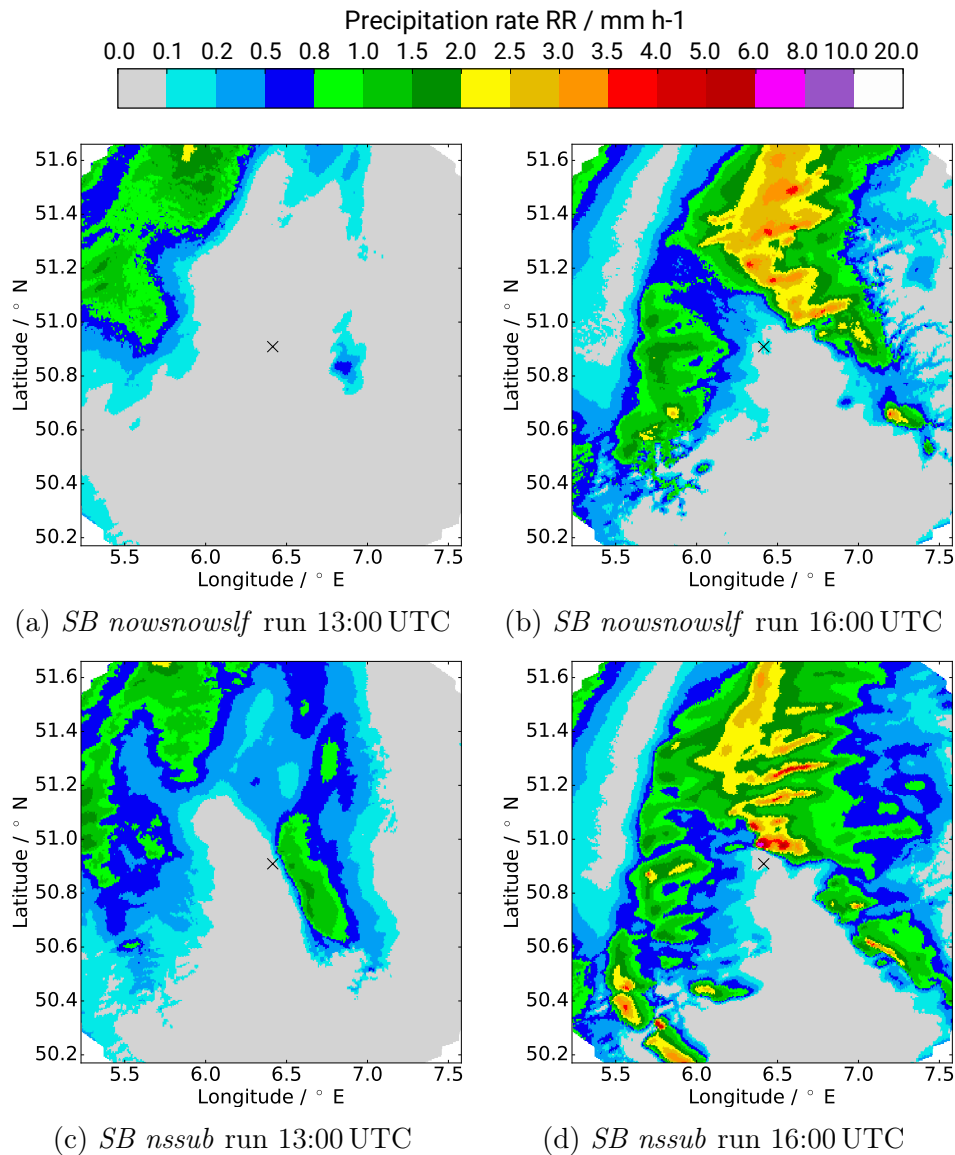


Figure 5.18.: Precipitation field of the SB sensitivity runs. The black cross indicates the cloud radar site and the center of the model domain.

The mismatch of the model runs to the observed precipitation field was large and similar structures could not be found. Furthermore, the intensity of the precipitation is underestimated by both schemes. Insights could be gained about the sensitivity of the microphysics schemes to growth processes in pure ice clouds. Especially the formulation of the aggregation processes and the treatment of supersaturation has been shown to have a considerable effect on the precipitation field, while the different implementations of sublimation do not seem to be important for the precipitation field (although a significant impact on  $Z_e$  close to the ground has been shown in previous sections).

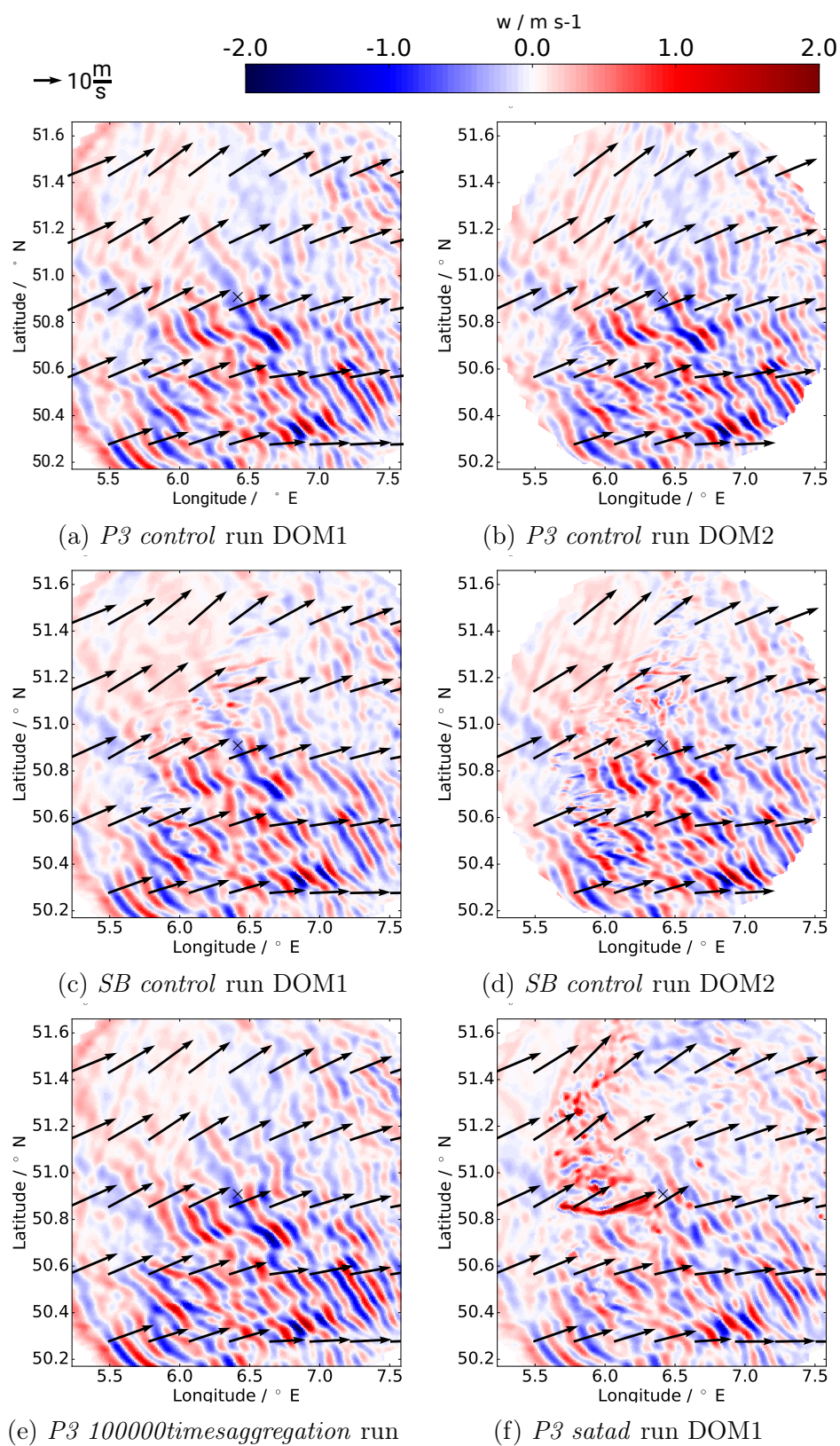


Figure 5.19.: Horizontal (displayed by black arrays; see reference vector above) and vertical wind speed  $w$  (see colorbar above) at 16:00 UTC and a height of 4.8 km for different model runs and domains. The black cross indicates the cloud radar site and the center of the model domain.

## 5.6. Using multi-frequency space to distinguish fingerprints of growth processes

Until now, this work has focused on the evaluation of the microphysics schemes by cloud radar measurements and the sensitivity of those schemes to changes in their formulation of growth processes. We observed significant differences between the schemes, but could not finally conclude which of the formulations performs better in the two case studies. Therefore, further connections between the schemes and observations are searched for by examining fingerprints of the growth processes in the cloud radar observables.

The remainder of this work investigates, how the growth processes, as assumed in the microphysics schemes (with a focus on the P3-scheme), manifest themselves in the multi-frequency space and to what extent it is possible to distinguish the fingerprints of growth processes in multi-frequency diagrams. This investigation is based on performed forward operation runs with up to three different frequencies. Those frequencies are chosen with respect to the radars used in the TRIPEX-campaign, in which in addition to the described 35.5 GHz radar also radars at 94.4 GHz and 9.4 GHz have been operated. These three frequencies belong to the Ka-, W- and X-Band. Therefore  $Z_e$  corresponding to the different frequencies are indicated by different indices ( $Z_{e,Ka}$  for the 35.5 GHz-radar,  $Z_{e,W}$  for the 94.4 GHz-radar and  $Z_{e,X}$  for the 9.4 GHz-radar) in the following. This allows us to cast a first glance, which process are the most important in the November case study, and if the assumptions of the microphysics schemes are correct.

As this analysis is limited to one case study (the November case) the goal of this work is not to make a comprehensive analysis of the frequency of occurrence of the ice growth processes, but rather to assess the feasibility of using synergy effects between models and their bulk microphysics schemes and multi-frequency measurements with regard to these processes.

### 5.6.1. Triple-frequency space

The triple-frequency space has been used to distinguish ice particle populations of different particle properties in previous studies (see Section 2.5.7; Kneifel et al., 2015). In this section, we evaluate if a similar picture as in those studies can be seen in forward operated signals with the assumptions on the microphysics and scattering schemes discussed in the Sections 2.4 and 2.5. If the overall picture is similar, this could provide a valuable testbed for testing and improving parametrizations. Furthermore, it is shown why it is not possible to separate between different pure ice cloud growth processes in the forward operated model output within the triple-frequency space.

In order to be able to analyze which factors influence the position of a modelled particle population in the triple-frequency space, firstly the dual-wavelength ratio  $DWR(\lambda_{w,1}, \lambda_{w,2})$  for two given wavelengths  $\lambda_{w,1}$  and  $\lambda_{w,2}$  should be considered. Equation 5.4 can be deduced by substituting Equation 2.21 and Equation 2.6 into

Equation 2.26.

$$\begin{aligned}
 DWR(\lambda_{w,1}, \lambda_{w,2}) &= 10 \log_{10} \left( \frac{\int \sigma_b(D, \lambda_{w,2}) D^\mu \exp(-\lambda D^\gamma) dD}{\int \sigma_b(D, \lambda_{w,1}) D^\mu \exp(-\lambda D^\gamma) dD} \right) \\
 &= dB \int \sigma_b(D, \lambda_{w,2}) D^\mu \exp(-\lambda D^\gamma) dD \\
 &\quad - dB \int \sigma_b(D, \lambda_{w,1}) D^\mu \exp(-\lambda D^\gamma) dD
 \end{aligned} \tag{5.4}$$

From Equation 5.4 we can see that DWR depends on the parameters of the size distribution and the scattering properties, which are expressed via  $\sigma_b$  (see Section 2.5). For all SB categories,  $\lambda$  is nonzero and  $\gamma$  deviates from one only for the snow category (Table 2.5). The P3 ice category does not include  $\gamma$  in the description of the size distribution and  $\mu$  is zero for  $D_{mean} > 0.17$  mm (see Section 2.4.2.3). At these low values of  $D_{mean}$  neither  $DWR_{Ka-W}$  nor  $DWR_{X-Ka}$  have considerable values (see Figure A.6). As a result, we can simplify Equation 5.4 by setting  $\mu = 0$  and  $\gamma = 1$  for the P3 ice category. Thus,  $DWR_{Ka-W}$  and  $DWR_{X-Ka}$  depend only on  $\lambda$  and  $\sigma_b$  for the P3 ice category.  $\sigma_b$ , in turn, depends on the  $m$ - $D$  relationship via  $V$  in Equation 2.25 in case of the SSRG-scattering routine and by its influence on the effective refractive index of the ice-air mixture in case of the Mie-sphere scattering routine.

Figure 5.20a shows combinations of bulk properties of the P3 category in the triple-frequency space. Size distributions with the same  $q_{norm}$  (independent of the specific combination of  $q_i$  and  $N_i$ ),  $F_{rim}$  and  $\rho_{rim}$  take up the same point in this space.

For unrimed particle populations ( $F_{rim} = 0$ ), the value of  $\rho_{rim}$  does not have a meaning, which is the reason why the crosses in Figure 5.20a represent all particle populations in the absence of rimed particles. For these particle populations, increasing  $q_{norm}$  leads to a continuous increase of  $DWR_{Ka-W}$  up to 11 dB and  $DWR_{X-Ka}$  up to 4 dB.  $DWR_{Ka-W}$  and  $DWR_{X-Ka}$  do not increase with  $q_{norm}$  for  $q_{norm} > 10^{-7} \text{ kg}^{-1}$ , because for this value of  $q_{norm}$  already the minimum prescribed  $\lambda_i$  of  $500 \text{ m}^{-1}$  is reached.

Going to a medium  $F_{rim}$  of 0.7 and  $\rho_{rim} = 500 \text{ kg m}^{-3}$  (see circles in Figure 5.20a), the curve, a particle population describes when increasing  $q_{norm}$ , does not change visibly. This appears logical if we consider that the largest particles (which contribute most to DWR values) are partially rimed and for those neither the exponent in the  $m$ - $D$  relationship nor the scattering routine is different from the unrimed particles. Nevertheless, there is a slower increase of  $DWR_{Ka-W}$  and  $DWR_{X-Ka}$  than for the unrimed particle population, because  $\lambda$  is higher at each  $q_{norm}$  until  $\lambda_i = 500 \text{ m}^{-1}$  is reached. The higher value of the  $a$  coefficient in the  $m$ - $D$  relationship does not balance this effect and has no visible impact on the shape of the curve. Only at values of  $F_{rim}$  close to one, the shape of the curves changes significantly (see the diamonds in Figure 5.20a which represent the combination of  $F_{rim}$  of 0.95 and  $\rho_{rim} = 500 \text{ kg m}^{-3}$ ). The sensitivity to the  $m$ - $D$  relationship of the curves from  $F_{rim} < 1$  turns out to be small if not changing the parameter in the  $m$ - $D$  relationship drastically (not shown).

A maximum of  $DWR_{Ka-W}$  is reached for  $q_{norm} = 3 \cdot 10^{-7} \text{ kg}$ , when  $F_{rim}$  and  $\rho_{rim}$  are set to 1.0 and  $700 \text{ kg m}^{-3}$ , respectively (Figure A.6a). The maximum is followed

by a decrease of  $\text{DWR}_{Ka-W}$  with increasing  $q_{norm}$ . When  $\text{DWR}_{X-Ka}$  still increases, this maximum of  $\text{DWR}_{Ka-W}$  manifests itself in a hook shape in the triple-frequency space. This feature can be seen for the particle populations with  $\rho_{rim} = 700 \text{ kg m}^{-3}$  and  $\rho_{rim} = 900 \text{ kg m}^{-3}$  (stars and triangles pointing to the left). For the populations with  $\rho_{rim} = 500 \text{ kg m}^{-3}$  (triangles pointing to the right) the increase of  $\text{DWR}_{Ka-W}$  gets very small at  $q_{norm}$  of about  $10^{-6} \text{ kg}$ , but a minimum is not reached. For  $\rho_{rim} = 500 \text{ kg m}^{-3}$  and  $\rho_{rim} = 900 \text{ kg m}^{-3}$  we see that also the increase of  $\text{DWR}_{X-Ka}$  is getting smaller for  $q_{norm}$  near  $10^{-5} \text{ kg}$ . The differences between the curves of different  $\rho_{rim}$  can be explained through the increase of the refractive index of the ice-air mixture with increasing  $\rho_{rim}$ , which has an impact on  $\sigma_b$ .

The curves in the triple-frequency space, which corresponds to the SB cloud ice and snow category, occupies a similar space than the curve of the unrimed P3 ice category for low values of  $q_{norm}$  (see crosses and pluses in Figure 5.20b). The onset of significant  $\text{DWR}_{Ka-W}$  starts later with increasing mean size of the particle distribution for the SB categories, so that e.g.  $\text{DWR}_{Ka-W} = 2 \text{ dB}$  is reached at higher values of  $q_{norm}$  than for the unrimed P3 ice category (visible in Figure A.6). Because this later onset is not seen for  $\text{DWR}_{X-Ka}$ , the curve of the SB ice categories has a slightly higher slope in the triple-frequency space for  $q_{norm} < 10^{-6}$ . Due to the less rigid restrictions on the mean size of the particle distribution compared to the unrimed P3 ice category, DWR values still change, when going to higher values of  $q_{norm}$ . For  $q_{norm} < 10^{-6} \text{ kg}$ ,  $\text{DWR}_{Ka-W}$  decreases for both unrimed SB categories. This decrease, together with an ongoing increase of  $\text{DWR}_{X-Ka}$ , leads to a hook shape of the curves similar to those from the P3 particle populations representing rimed particles. The slight difference between the SB cloud ice and snow category arises from both the different size distribution parameter and  $m$ - $D$  relationship parameter.

The shape of the curves from the SB graupel and hail category also match well with the P3 ice category when a particle population with similar properties is represented. We see a hook shape for both categories (more pronounced for the hail category). Compared to the P3 ice category, the SB categories follow an almost straight line with only slightly increasing  $\text{DWR}_{X-Ka}$  values up to higher values of  $q_{norm}$ , before the increase of  $\text{DWR}_{X-Ka}$  dominates and the curves bends to the left. This difference becomes smaller if the size distribution parameter  $\mu$  and  $\gamma$  are set to those of the P3 ice category (upward pointing triangles).

The fact that  $q_{norm}$  (rather than a combination of  $q_i$  and  $N_i$ ) is sufficient to determine the location in the triple-frequency space implies, that processes, as implemented in the microphysics schemes, which increase  $q_{norm}$  by lowering  $N_i$  can not be distinguished from processes, which increase  $q_{norm}$  by increasing  $q_i$  within a given category. As a result, the pure ice cloud growth processes, discussed in the previous sections, can not be separated in this space. We overcome this limitation in Section 5.6.2 by replacing the y-axis with  $Z_e$ .

In contrast, processes which affect  $F_{rim}$  or  $\rho_{rim}$  in the P3-scheme or lead to a transformation of particles to another category in the SB-scheme, could be analyzed in the triple-frequency space, but as this work focuses on the pure ice cloud growth processes, we will not follow up on this approach. Merely, self-collection of cloud ice particles

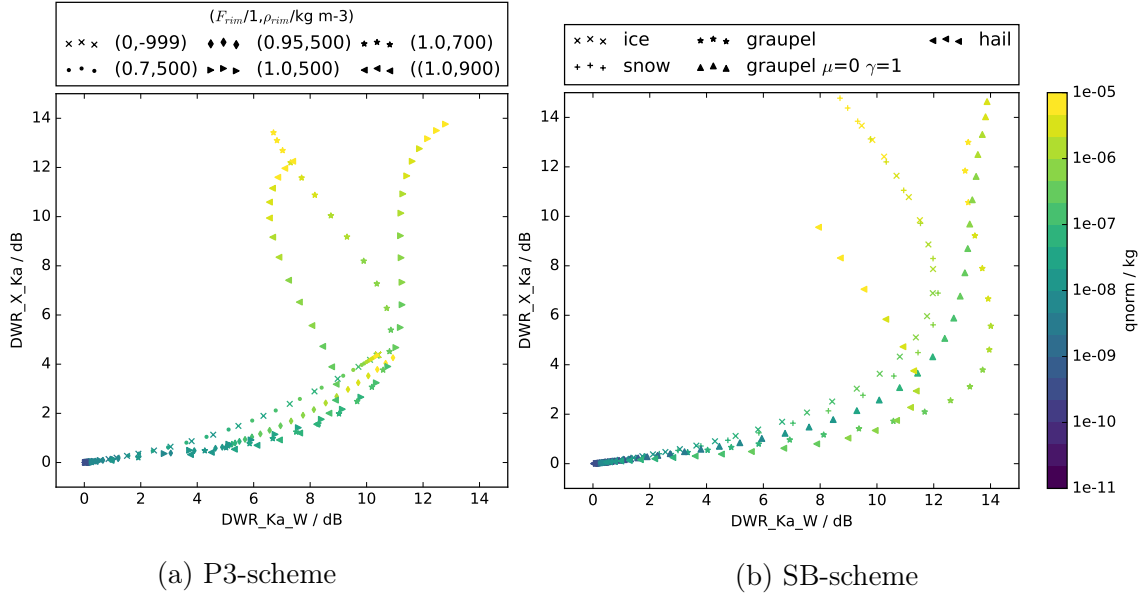


Figure 5.20.: Ice categories of the SB-scheme and combinations of bulk properties of the P3 ice category (both distinguished by different symbol types as denoted above the figures) in the triple-frequency space.  $q_{norm}$  of each data point is indicated by the colors of the symbols. For graupel also a modified version with changed size distribution parameter  $\mu$  and  $\gamma$ , as denoted in the legend, is displayed.

which forms snow particles in the SB-scheme is a pure ice cloud growth process which could be analyzed in that way. But the similarity of the curves corresponding to the cloud ice and the snow category in Figure 5.20b promises only limited potential of this analysis.

The clockwise rotation of the curves with increasing effective density (as observations e.g in Kneifel et al. (2015) suggest; see also Section 2.5.7) is reflected here only when approaching values of  $F_{rim}$  close to one at relative low values of  $\rho_{rim}$  (in the P3-scheme) or switching the category from the SB ice cloud or snow category to the graupel category. Especially at high values of  $q_{norm}$  we see, in a sense, an opposite effect - a bending towards higher  $DWR_{X-Ka}$ -values at lower  $q_{norm}$  - when staying at  $F_{rim} = 1$  and increasing the rime density. A similar effect occurs, when switching from hail to graupel in the SB scheme (which is considered to have a lower  $\rho_{rim}$ ). Additionally, the parameters of the size distribution proved to be important for the shape of the curve in the triple-frequency space.

### 5.6.2. $Z_e$ -DWR space

As shown in the previous section, there are no independent signatures of a change in  $q_i$  and  $N_i$  in the triple-frequency space. Because we are interested in distinguishing processes, which differ from each other in the way they are increasing or decreasing  $q_{norm}$  (in particular aggregation, depositional growth, sublimation and sedimentation),

we replace the y-axis with a radar observable which is also sensitive to a change in  $N_i$  even when  $q_{norm}$  is kept constant. The most obvious radar observable, which meets this criterion, is  $Z_e$ . Although even  $DWR_{Ka-W}$  is sensitive to a change in mean size only for relative high values of  $q_{norm}$  we stick to this variable as an indicator for the change in the mean size of the particle population. An alternative as a size indicator would be  $v_{doppler}$ , which is more sensitive to small values of  $q_{norm}$ , but has the disadvantage of being dependent on the air motion (which could only be overcome by longer temporal average periods only). It has to be considered, that DWR is not always a monotonic function of  $q_{norm}$  (see previous section), but monotony is given for the P3 ice category in the absence of rime (where we want to apply this analysis). Choosing  $DWR_{X-W}$  would give a considerable sensitivity to changes in mean size over a wider range of  $q_{norm}$  and fulfill the criterion of monotony also for most combinations of bulk properties. Nevertheless,  $DWR_{Ka-W}$  has been chosen here, because  $DWR_{X-Ka}$  from the available radar of the November case exhibits a rather high signal to noise ratio.

#### 5.6.2.1. Isolines of $q_i$ and $N_i$ based on the P3 ice category in the absence of rime

If we limit our investigation to the unrimed representations of the P3 ice category,  $q_i$  and  $N_i$  determine the bulk properties of each model pixel completely. As a result, it also determines  $Z_e$  at all frequencies if the environmental conditions (such as temperature and relative humidity) are constant and attenuation is not important or the data is corrected to this effect before the analysis. By varying  $q_i$  and  $N_i$  over a wide range and keeping the other variable constant, isolines of these two properties are generated (see gray lines in Figure 5.21).  $Z_e$  corresponding to a given combination of  $q_i$  and  $N_i$  is calculated with PAMTRA with the same assumptions as the evaluation test of the adaption in Table 3.1.

Figure 5.21 also contains a possible growth scenario of a particle population in the P3-scheme. In this scenario  $DWR_{Ka-W}$  increases first through depositional growth (the signs of the corresponding process rates are denoted on the right of Figure 5.21), before aggregation, sublimation and a combination of sublimation and sedimentation further increases  $DWR_{Ka-W}$ . While depositional growth leads to a change along the  $N_i$  isoline and aggregation along the  $q_i$  isoline, sublimation (as implemented in the P3-scheme) takes a curve in the  $Z_e$ -DWR space which is not following an isoline, but stays at the same  $DWR_{Ka-W}$  value. Sedimentation can change both,  $q_i$  and  $N_i$ , with both signs (see also Section 5.3). For example, if the flux of  $q_i$  is bigger at the top of the grid box than at the bottom, the change in  $q_i$  induced by sedimentation is positive. But the fluxes could also be reversed. Near the cloud base we observed a positive change in  $q_{norm}$  through sedimentation in Section 5.3. This positive change is induced by a decreasing flux of  $q_i$  which is not compensated by the decrease of the flux of  $N_i$ . If sedimentation occurs in the here described way, the superposition with sublimation can result in the path of the yellow crosses in Figure 5.21.

By plotting  $Z_e$  against  $DWR_{Ka-W}$ , pure ice cloud growth processes can be distinguished by characteristic curves. The interpretation of this plot can be simplified

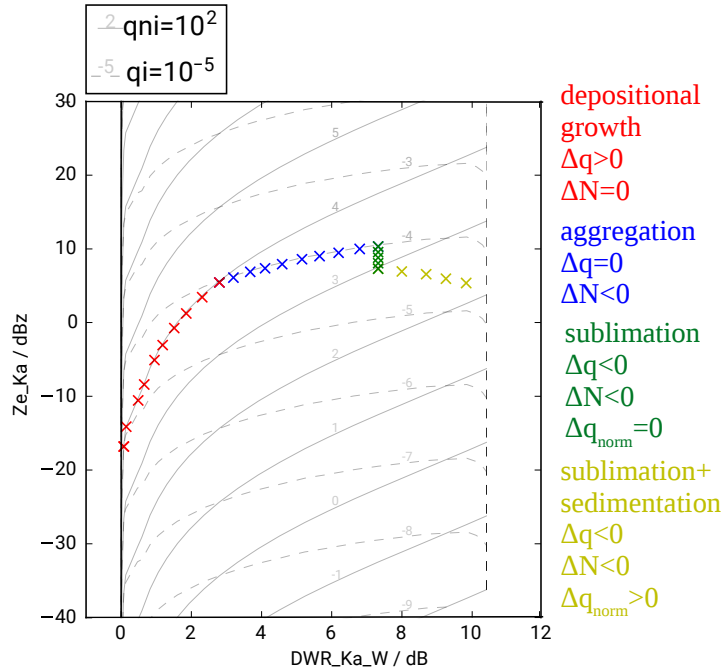


Figure 5.21.: Idealized analysis in the  $Z_e$ -DWR space. The gray lines indicate isolines of  $N_i$  (solid) and  $q_i$  (dashed) for each decade. The crosses indicate a hypothetical evolution of  $N_i$  and  $q_i$ , which could occur if depositional growth, aggregation, sublimation and sublimation together with sedimentation takes place successively. The sign of the change in  $N_i$  and  $q_i$  is denoted on the right of the figure in the corresponding color to the crosses to which this change is applied.

by isolines of  $q_i$  and  $N_i$ . Simultaneously occurring processes, however, hamper the tracing of the signature in the radar variables back to the individual process.

### 5.6.2.2. Forward operated output and observations in the $Z_e$ -DWR space

In this section, the theoretical considerations from the previous section are evaluated by plots of the forward operated model output and observations from the November case in the  $Z_e$ -DWR space. By depicting not only the *P3 control* run, but also the sensitivity runs regarding the pure ice cloud growth processes, the impact of individual growth processes to the  $Z_e$ -DWR space is tested.

In order to ensure, that we only consider completely unrimed or almost completely unrimed particles the investigation is limited to the time range where riming is unimportant (see also Section 5.3). Moreover, only grid points which fulfill the following criteria are taken into account:  $(q_c + q_r) \cdot q_i < 10^{-2}$  and  $F_{rim} < 10^{-2}$ . In this way, the impact of liquid hydrometeors and rimed particles can be neglected in the analysis. Before 10:00 UTC, there are only few grid points where significant  $DWR_{Ka-W}$  is reached. As a result, fall streaks for which the characteristic particles reach the cloud base before 10:00 UTC are not analyzed.

Figure 5.22 shows the  $Z_e$ -DWR plots for the forward operated P3 model runs of the November case. Displayed are the grid points, which belong to the fall streaks (see Section 5.2). In the *P3 control* run (see Figure 5.22a), we see an increase of  $Z_e$  with  $\text{DWR}_{Ka-W}$  in the time range from 10:15 UTC to 11:30 UTC, which is almost parallel to the isolines of  $N_i$ . This supports the hypothesis of Section 5.3, that depositional growth is the most important growth mechanism here. After this positive slope of  $Z_e$  with  $\text{DWR}_{Ka-W}$ , a decrease of  $Z_e$  with increasing  $\text{DWR}_{Ka-W}$  follows. This is most likely due to the superposition of the process rates of sublimation and sedimentation, as discussed in Section 5.6.2.1. In the *P3 nisub0* run (see Figure 5.22b), the fall streaks in this time range do not show a negative slope of  $Z_e$  with  $\text{DWR}_{Ka-W}$ , but a return to low values of  $\text{DWR}_{Ka-W}$  on a similar path as the increase (which becomes visible if the evolution of the height is additionally indicated in the plot, which is not the case here to provide a clearer representation). This difference between the *P3 nisub0* and the *P3 control* run emphasizes the sensitivity of the change in  $q_{norm}$  at the cloud base due to the formulation of sublimation.

Besides the *P3 100000timesaggregation* run, all model runs show a non-monotonic increase of  $\text{DWR}_{Ka-W}$  at low values of  $\text{DWR}_{Ka-W}$  for the time range after 11:45 UTC. This non-monotony is also visible in Figure 5.9 and can only be explained by advection of inhomogeneities in the  $N_i$  field. In the *P3 100000timesaggregation* run  $Z_e$  increases nearly with the same slope with  $\text{DWR}_{Ka-W}$  as the isolines of  $q_i$ . This coincidence of the slopes is an obvious consequence of the dominance of aggregation for the particle growth at the mean particle range, where  $\text{DWR}_{Ka-W}$  also exhibits high sensitivity. One notable feature of Figure 5.22c is, that only the fall streaks, in which the particles reach the cloud base at 12:45 UTC, include grid points where  $N_i$  takes values larger than  $10^4 \text{ kg}^{-1}$ . The *P3 noaggregation* run (see Figure 5.22d) shows very few deviations from the *P3 control* run, which once again demonstrates the minimal impact of aggregation, as formulated in the P3-scheme, to the increase of mean particle size.

Figure 5.23 displays vertical profiles of the observations of the November case in the  $Z_e$ -DWR-space. This vertical profiles should not deviate much from the fall streaks (which can not be derived for the observations as explained in Section 5.2). The vertical profiles are just shown from 10:15 UTC to 11:45 UTC in an interval of 15 minutes, because at other time steps either the spectral width is too high (indicating the presence of liquid hydrometeors) or  $\text{DWR}_{Ka-W}$  is very low. In order to reduce the noise of  $\text{DWR}_{Ka-W}$ , the radar data is averaged over 5 minutes temporally and 150 m vertically. Nevertheless, there are bigger gaps between adjacent data-points. The fall streaks show a slope which is closer to the isolines of  $q_i$ , than those of  $N_i$ . If the relevant assumptions of the P3-scheme are satisfied for this case and time range, this slope indicates that aggregation is more dominant as a growth processes than the P3-scheme predicts. As a second point, the relatively good match of the overall distribution of the fall streaks in the  $Z_e$ -DWR space between the observations and the forward operated observables should be highlighted here. Finally, it should be noted, that the negative slope of  $Z_e$  with  $\text{DWR}_{Ka-W}$  does not appear in the observations in this time range. However, as this analysis relies on a few fall streaks, this is no robust evidence that the implementation of the sublimation, as done in the P3-scheme, is

## 5. Results and discussion

unrealistic (keep in mind that the CFADs in Figure 5.13 indicated a more realistic slope of  $Z_e$  near the cloudbase when sublimation decreases the number concentration in the microphysics schemes).

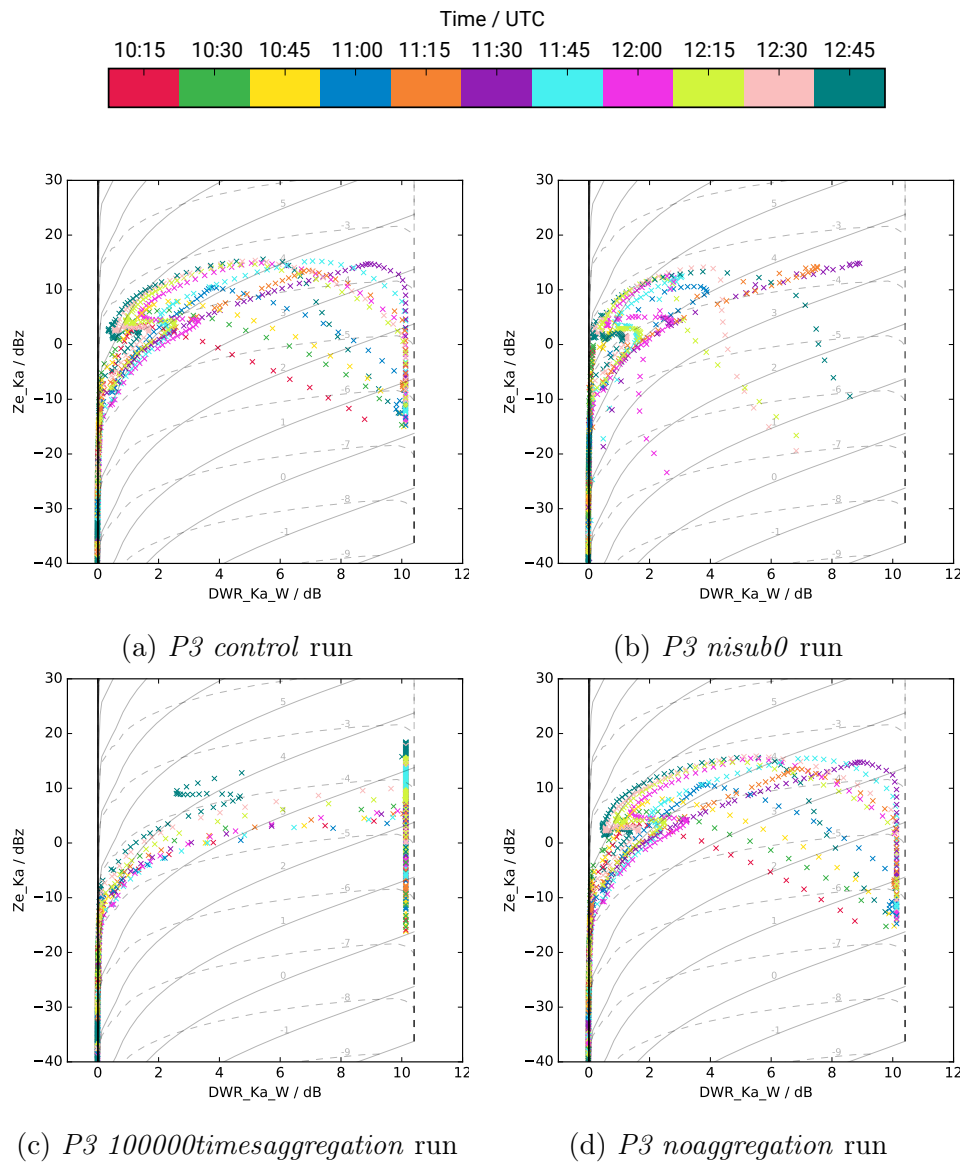


Figure 5.22.: P3 November case in the  $Z_e$ -DWR space. Displayed are the position of the grid points in the  $Z_e$ -DWR space, which belong to the fall streaks (see Section 5.2). The colorbar at the top denotes the time where the particle population reaches the cloud base. The underlying isolines depict the same quantities as in Figure 5.21.

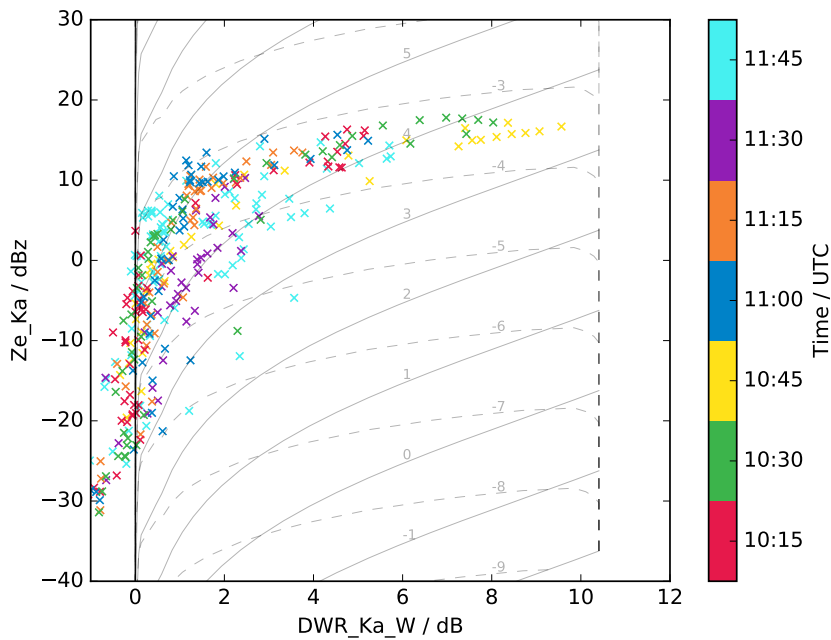


Figure 5.23.: Observations of the November case in the  $Z_e$ -DWR space. Displayed are vertical profiles in a 15 min interval. The underlaid isolines depict the same quantities as in Figure 5.21.

In this section, a first application of the isolines of prognostic variables, as a support for the interpretation of growth processes, in the  $Z_e$ -DWR space is shown. By comparing the slope of  $Z_e$  with  $Z_e$ -DWR with the isolines, we were able to make suppositions about the relative importance of growth processes, which indicate that depositional growth is the main growth mechanism in the *P3 control* run, but the observations show the dominance of aggregation over other processes. However, this application relies on a very limited database. With the restriction to the pure ice cloud, a single case study and an interval of four fall streaks per hour, we were limited to six fall streaks for the observations and eleven fall streaks for the forward operated output. Therefore, only the possibilities of this depiction of multi-frequency radar measurements in combination with forward operated output could be demonstrated here, but no final conclusion of the frequency of occurrence of the processes can be drawn. These possibilities become apparent, when comparing the sensitivity runs with the control run in the  $Z_e$ -DWR space, which allows, to some extent, a reconstruction of the individual impact of the process formulation. In a higher dimensional space (e.g. combining the triple-frequency space with  $Z_e$  of one frequency), a similar approach could also be employed for analyzing processes including riming.



## 6. Conclusion/Outlook

In the course of this thesis an adaption of PAMTRA to the P3-scheme has been developed. This adaption uses only the four prognostic variables of the P3-scheme (in addition to the atmospheric variables). The formulation in the extended PAMTRA exhibits reasonable dependencies of  $Z_e$  and  $DWR_{Ka-W}$  on the prognostic variables (as shown in Chapter 3) and has been applied in two case studies (see Section 5.1). An application to other case studies is desirable and could yield a more comprehensive evaluation of the P3-scheme in terms of vertical hydrometeor distribution. With a few modifications, the adaption can be extended towards the multi-category P3-scheme (Milbrandt et al., 2015), which is currently not available as a part of ICON-LEM.

The above mentioned case studies (simulating the atmosphere on a domain of 220 km on the days of the 24th April 2013 and the 24th November 2015) represent days, where the cloud features are largely influenced by the large-scale synoptic situation, including frontal passages. On the one hand, despite this stratiform nature of the cloud system, the clouds exhibit inhomogeneities in their properties which hamper the analysis of the growth processes (Sections 5.3 and 5.6). Therefore, an application of this analysis to more stratiform cases would be beneficial. On the other hand, the main conceptual differences between the P3- and the SB-scheme lie in the representation of rimed particles and riming processes. Therefore, also case studies with strong convective elements could provide more insights into the performance of the P3-scheme.

A good performance of ICON-LEM with both schemes and both case studies has been observed in terms of the cloud structure (see Section 5.1). This was expected for the April case in combination with the SB-scheme, because the similar setup in Heinze et al. (2016) also showed a good match in terms of the cloud structure. In addition, the deficiencies in the vertical profile of the forward operated  $Z_e$ , which consist mainly in an overestimation of  $Z_e$  at heights of about 4 km as seen in Heinze et al. (2016), have been confirmed by the small domain runs of this work. As the main difference between the schemes turned out to be related to aggregation, this process seems to be too efficient in the SB-scheme for this case. However, better agreement between the forward operated  $Z_e$  and observations could be achieved in the April case when replacing the SB-scheme by the P3-scheme. Conversely, the November case showed different biases, in favour of the SB-scheme, between the forward operated  $Z_e$  and observations. While the SB-scheme exhibited a large mismatch to the observations only in the morning hours, the P3-scheme revealed an underestimation of  $Z_e$  over the whole day. The performance of the SB-scheme was even more improved by formulating sublimation as in the P3-scheme. Further, more comprehensive, studies

could address the topic if sublimation should be treated in the same way as in the P3-scheme, per default. A robust result of these studies could yield advantages e.g. in cloud base investigations. The underestimation of  $Z_e$  by the P3-scheme results to a great extent from too inefficient aggregation. This has been shown in two ways: Firstly, when turning off the self-collection of snow, also the SB-scheme shows an underestimation of  $Z_e$ . Secondly, by scaling the process rates of aggregation within the P3-scheme the underestimation of  $Z_e$  could be reduced. Aggregation is expected to be stronger in the multi-category P3-scheme due to strong aggregation between modes with sufficient different mean size. Considering both case studies, the findings seem inconsistent at a first glance. However, aggregation is formulated merely as a function of temperature (without regarding a maximum at near  $-15^\circ\text{C}$ ; see Section 2.3.3) and bulk hydrometeor properties in both schemes (see Section 2.3.3). Other influences on aggregation (like turbulence or crystal shape), which could differ between the two case studies are not considered. As a hypothesis one can assume, that aggregation takes place less effectively in the April case than in the November case in increasing the mean size, due to weaker turbulence. Although the increase of collision efficiency with stronger turbulence and its impact on ice-ice and water-ice collision has already been emphasized in Pinsky and Khain (1998), the influence of turbulence on the collection processes is regarded as constant in the SB-scheme and not considered at all in the P3-scheme. A coupling of the collection rates (including aggregation) to the subgrid scale turbulence as predicted in ICON-LEM (Dipankar et al., 2015), could result in a better representation of the collection processes.

The 312 m resolution runs exhibited no significant advantage over the runs with 624 m resolution (see Figures 5.3 and 5.6). As the differences between the schemes are much larger than between these different resolutions, we can expect small potential in improving the predictive skills of the model by running even higher resolution runs. In order to improve e.g. the prediction of precipitation events, further developments on the representation of microphysics seem more promising.

Despite the good match in the vertical cloud structure, the structure of the precipitation field is weakly reproduced by the model runs (see Section 5.5). The large differences between the precipitation field of the model runs with the P3-scheme and saturation adjustment, the P3-scheme with enhanced aggregation and the control run of the P3-scheme suggest large potential in improving the predictive skill in regard to precipitation. This improvement could be gained by modifications of the formulation of aggregation and saturation within the microphysics scheme. Furthermore, it was shown, that the treatment of supersaturation in the model has a significant impact on the precipitation simulated by ICON-LEM. An investigation of the role of saturation adjustment vs. explicit treatment of saturation in ICON-LEM would benefit from using the piggy-backing method (Grabowski, 2014), in order to distinguish between direct and indirect (by feedbacks to the dynamics) impacts on the precipitation field.

The second goal of this study was, beyond the detection of shortcomings and deficiencies of the microphysics schemes, to point out the potential and the limits

---

of new approaches, by which vertically-pointing non-polarimetric cloud radars can be used for improvements in bulk microphysics schemes. As described in Section 2.4.2, the P3-scheme allows a continuous representation of particle properties with different degrees of riming and rime densities by two prognostic variables ( $F_{rim}$  and  $\rho_{rim}$ ), which are not predicted by classical two-moment schemes like the SB-scheme. Whereas changes in  $F_{rim}$  showed only limited effect in the triple-frequency space, a continuous shift of characteristic curves in the triple-frequency space could be found for changes in  $\rho_{rim}$ . These shifts, in turn, do not fit well with the findings in field campaigns described in existing literature (e.g. Kneifel et al. (2015)). The lack of a predicted quantity, which indicates if the particles can be regarded as pristine crystals or rather as aggregates composed of multiple pristine crystals, impedes an analysis of pure ice-cloud processes and the differentiability between e.g. depositional growth and aggregation by using the triple-frequency space. This problem could be overcome by adding such a predicted quantity, e.g. by a similar approach as in Brdar and Seifert (2018), in which the number of primary ice crystals, of which a particle is composed, is predicted. Gergely et al. (2017) described the dependency of  $\sigma_b$  on the surface-area-to-volume ratio and linked this to the number of spheres, which can represent an ice particle by the surface-area-to-volume ratio. They offered a physical interpretation of previously considered snowfall triple-frequency measurements. Combining a microphysics scheme, which can predict the number of primary ice crystals and an approach to calculate the scattering properties, similar to Gergely et al. (2017), could enable deeper insights into aggregation processes and constitute a valuable testbed for bulk schemes.

In the last section, a new way of analyzing the conservation of bulk properties in microphysics schemes in radar observables has been proposed by depicting isolines of  $q_i$  and  $N_i$  from the P3-scheme in the  $Z_e$ -DWR space. This connection between the bulk properties and the radar observables has been established via the forward operator PAMTRA. In this way processes, which occur in pure ice clouds, can be distinguished. If the sensitivity to the  $m$ - $D$  relationship parameters and scattering routines turns out to be small, this analysis could yield a simple way of analyzing microphysical processes in pure ice clouds and how they should be formulated in bulk schemes. Similar approaches, that combine at least three different radar frequencies can result in analyzing also changes in other bulk properties (like  $F_{rim}$  or  $\rho_{rim}$ ). The restriction of this analysis to relatively large mean sizes of the particle populations could be reduced by the use of shorter wavelengths (as proposed in Battaglia et al. (2014)) or a replacement of DWR by the temporal averaged  $v_{Doppler}$ . In this study, no attempt was made to detect processes directly within the cloud radar measurements. This detection is, however, crucial for using the combined view of forward operated quantities and radar measurements as a testbed for new parametrizations of individual microphysical processes. Approaches to execute this detection have been proposed by analyzing the full Doppler spectra of  $Z_e$  and  $ZDR$  (Pfitzenmaier et al., 2018) or a variety of polarimetric variables (Ryzhkov et al., 2016).



# Bibliography

- Battaglia, A. et al. (2014). “G band atmospheric radars: new frontiers in cloud physics”. In: *Atmospheric Measurement Techniques* 7, pp. 1527–1546.
- Bauer, P. et al. (2015). “The quiet revolution of numerical weather prediction”. In: *Nature* 525.7567, p. 47.
- Boucher, O. et al. (2013). “Clouds and aerosols”. In: *Climate Change 2013: The Physical Science Basis. Contribution of Working Group I to the Fifth Assessment Report of the Intergovernmental Panel on Climate Change*. Ed. by T. F. Stocker et al. Cambridge, UK: Cambridge University Press, pp. 571–657. DOI: [10.1017/CB09781107415324.016](https://doi.org/10.1017/CB09781107415324.016).
- Brandes, E. A. et al. (2007). “A statistical and physical description of hydrometeor distributions in Colorado snowstorms using a video disdrometer”. In: *Journal of applied meteorology and climatology* 46.5, pp. 634–650.
- Brdar, S. and A. Seifert (2018). “McSnow: A Monte-Carlo Particle Model for Riming and Aggregation of Ice Particles in a Multidimensional Microphysical Phase Space”. In: *Journal of Advances in Modeling Earth Systems* 10.1, pp. 187–206.
- Casati, B. et al. (2004). “A new intensity-scale approach for the verification of spatial precipitation forecasts”. In: *Meteorological Applications* 11.2, pp. 141–154. DOI: [10.1017/S1350482704001239](https://doi.org/10.1017/S1350482704001239).
- Cober, S. G. and R. List (1993). “Measurements of the heat and mass transfer parameters characterizing conical graupel growth”. In: *Journal of the atmospheric sciences* 50.11, pp. 1591–1609.
- Dietlicher, R. et al. (2018). “Prognostic parameterization of cloud ice with a single category in the aerosol-climate model ECHAM(v6.3.0)-HAM(v2.3)”. In: *Geoscientific Model Development* 11.4, pp. 1557–1576. DOI: [10.5194/gmd-11-1557-2018](https://doi.org/10.5194/gmd-11-1557-2018). URL: <https://www.geosci-model-dev.net/11/1557/2018/>.
- Dipankar, A. et al. (2015). “Large eddy simulation using the general circulation model ICON”. In: *Journal of Advances in Modeling Earth Systems* 7.3, pp. 963–986.
- Gergely, M. et al. (2017). “Using snowflake surface-area-to-volume ratio to model and interpret snowfall triple-frequency radar signatures”. In: *Atmospheric Chemistry and Physics* 17.19, pp. 12011–12030.
- Grabowski, W. W. (2014). “Extracting microphysical impacts in large-eddy simulations of shallow convection”. In: *Journal of the Atmospheric Sciences* 71.12, pp. 4493–4499.
- Grabowski, W. W. and H. Morrison (2017). “Modeling condensation in deep convection”. In: *Journal of the Atmospheric Sciences* 74.7, pp. 2247–2267.
- Hande, L. and C. Hoose (2017). “Partitioning the primary ice formation modes in large eddy simulations of mixed-phase clouds”. In: *Atmospheric Chemistry and Physics* 17.22, pp. 14105–14118.

- Hande, L. et al. (2015). “Seasonal variability of Saharan desert dust and ice nucleating particles over Europe”. In: *Atmospheric Chemistry and Physics* 15.8, pp. 4389–4397.
- Hande, L. et al. (2016). “Parameterizing cloud condensation nuclei concentrations during HOPE”. In: *Atmospheric Chemistry and Physics* 16.18, pp. 12059–12079.
- Heinze, R. et al. (2016). “Large-eddy simulations over Germany using ICON: A comprehensive evaluation”. In: *Quarterly Journal of the Royal Meteorological Society*.
- Heymsfield, A. J. (1982). “A comparative study of the rates of development of potential graupel and hail embryos in High Plains storms”. In: *Journal of the Atmospheric Sciences* 39.12, pp. 2867–2897.
- (2003). “Properties of tropical and midlatitude ice cloud particle ensembles. Part II: Applications for mesoscale and climate models”. In: *Journal of the atmospheric sciences* 60.21, pp. 2592–2611.
- Heymsfield, A. J. et al. (2013). “Ice cloud particle size distributions and pressure-dependent terminal velocities from in situ observations at temperatures from 0° to 86° C”. In: *Journal of the Atmospheric Sciences* 70.12, pp. 4123–4154.
- Hobbs, P. V. et al. (1974). “The dimensions and aggregation of ice crystals in natural clouds”. In: *Journal of geophysical Research* 79.15, pp. 2199–2206.
- Hogan, R. J. and C. D. Westbrook (2014). “Equation for the microwave backscatter cross section of aggregate snowflakes using the self-similar Rayleigh–Gans approximation”. In: *Journal of the Atmospheric Sciences* 71.9, pp. 3292–3301.
- Hogan, R. J. et al. (2012). “Radar scattering from ice aggregates using the horizontally aligned oblate spheroid approximation”. In: *Journal of Applied Meteorology and Climatology* 51.3, pp. 655–671.
- Hoose, C. and O. Möhler (2012). *Heterogeneous ice nucleation on atmospheric aerosols: a review of results from laboratory experiments, Atmo-30 spheric Chemistry and Physics*, 12, 9817–9854.
- Hulst, H. C. and H. C. van de Hulst (1957). *Light scattering by small particles*. Courier Corporation.
- Illingworth, A. J. et al. (2015). “The EarthCARE satellite: The next step forward in global measurements of clouds, aerosols, precipitation, and radiation”. In: *Bulletin of the American Meteorological Society* 96.8, pp. 1311–1332.
- Kalesse, H. et al. (2013). “On using the relationship between Doppler velocity and radar reflectivity to identify microphysical processes in midlatitudinal ice clouds”. In: *Journal of Geophysical Research: Atmospheres* 118.21.
- Khain, A. et al. (2015). “Representation of microphysical processes in cloud-resolving models: Spectral (bin) microphysics versus bulk parameterization”. In: *Reviews of Geophysics* 53.2, pp. 247–322.
- Khairoutdinov, M. and Y. Kogan (2000). “A new cloud physics parameterization in a large-eddy simulation model of marine stratocumulus”. In: *Monthly weather review* 128.1, pp. 229–243.
- Kneifel, S. et al. (2011). “A triple-frequency approach to retrieve microphysical snowfall parameters”. In: *Journal of Geophysical Research: Atmospheres* 116.D11.
- Kneifel, S. et al. (2015). “Observed relations between snowfall microphysics and triple-frequency radar measurements”. In: *Journal of Geophysical Research: Atmospheres* 120.12, pp. 6034–6055.

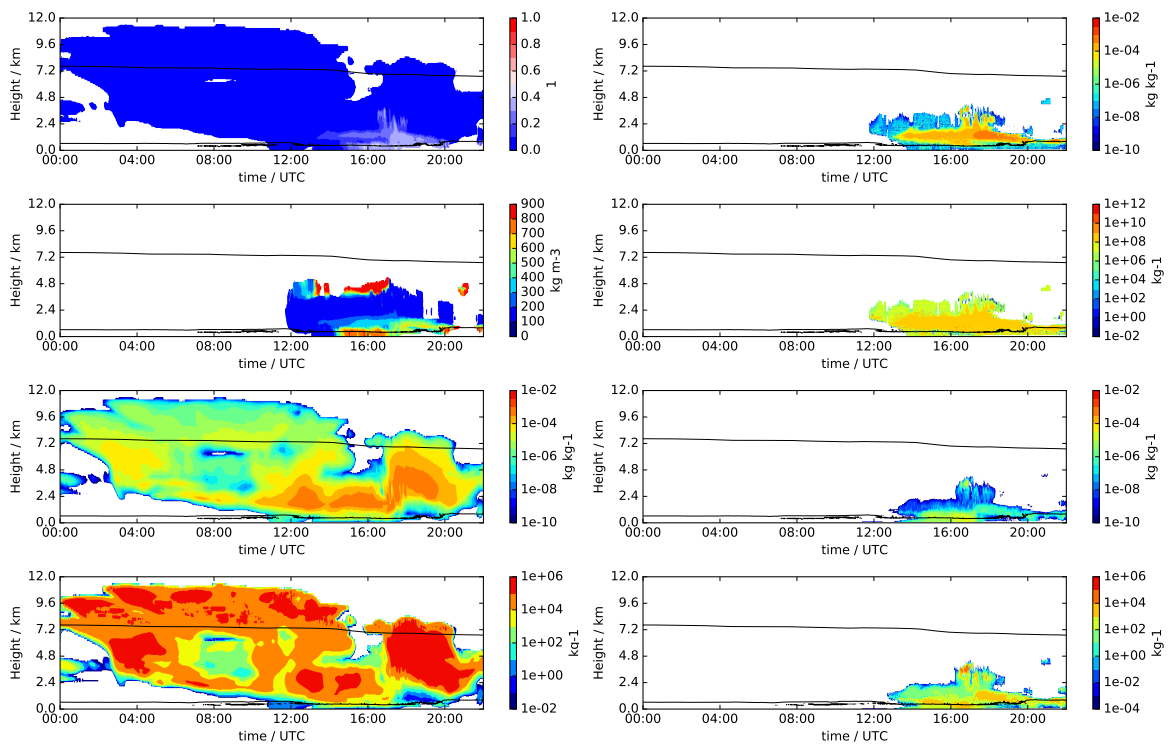
- Kollias, P. et al. (2011). “Cloud radar Doppler spectra in drizzling stratiform clouds: 1. Forward modeling and remote sensing applications”. In: *Journal of Geophysical Research: Atmospheres* 116.D13.
- Kumjian, M. R. and A. Ryzhkov (2012). “The impact of size sorting on the polarimetric radar variables”. In: *Journal of the Atmospheric Sciences* 69.6, pp. 2042–2060.
- Lamb, D. and J. Verlinde (2011). *Physics and chemistry of clouds*. Cambridge University Press.
- Leinonen, J. et al. (2011). “Mapping radar reflectivity values of snowfall between frequency bands”. In: *IEEE Transactions on Geoscience and Remote Sensing* 49.8, pp. 3047–3058.
- Leinonen, J. et al. (2017). “Evaluation of the Rayleigh–Gans Approximation for Microwave Scattering by Rimed Snowflakes”. In: *Quarterly Journal of the Royal Meteorological Society*.
- Leuenberger, D. et al. (2010). “A generalization of the SLEVE vertical coordinate”. In: *Monthly weather review* 138.9, pp. 3683–3689.
- Maahn, M. (2015). “Exploiting vertically pointing Doppler radar for advancing snow and ice cloud observations”. PhD thesis. Universitaet zu Koeln.
- Macke, A. et al. (2017). “The HD (CP) 2 Observational Prototype Experiment (HOPE)—an overview”. In: *Atmospheric Chemistry and Physics* 17.7, pp. 4887–4914.
- Marshall, J. S. (1953). “Precipitation trajectories and patterns”. In: *Journal of Meteorology* 10.1, pp. 25–29.
- Matrosov, S. Y. (1992). “Radar reflectivity in snowfall”. In: *IEEE transactions on geoscience and remote sensing* 30.3, pp. 454–461.
- (1998). “A dual-wavelength radar method to measure snowfall rate”. In: *Journal of Applied Meteorology* 37.11, pp. 1510–1521.
- Mie, G. (1908). “Beiträge zur Optik trüber Medien, speziell kolloidaler Metallösungen”. In: *Annalen der physik* 330.3, pp. 377–445.
- Milbrandt, J. and H. Morrison (2013). “Prediction of graupel density in a bulk microphysics scheme”. In: *Journal of the Atmospheric Sciences* 70.2, pp. 410–429.
- (2016). “Parameterization of cloud microphysics based on the prediction of bulk ice particle properties. Part III: Introduction of multiple free categories”. In: *Journal of the Atmospheric Sciences* 73.3, pp. 975–995.
- Milbrandt, J. and M. Yau (2005). “A multimoment bulk microphysics parameterization. Part I: Analysis of the role of the spectral shape parameter”. In: *Journal of the atmospheric sciences* 62.9, pp. 3051–3064.
- Milbrandt, J. et al. (2015). “Parameterization of cloud microphysics based on the prediction of bulk ice particle properties. Part II: Case study comparisons with observations and other schemes”. In: *J. Atmos. Sci* 72, pp. 312–339.
- Mitchell, D. L. (1996). “Use of mass-and area-dimensional power laws for determining precipitation particle terminal velocities”. In: *Journal of the atmospheric sciences* 53.12, pp. 1710–1723.
- Morrison, H. and W. W. Grabowski (2008). “A novel approach for representing ice microphysics in models: Description and tests using a kinematic framework”. In: *Journal of the Atmospheric Sciences* 65.5, pp. 1528–1548.

- Morrison, H. and J. Milbrandt (2015). “Parameterization of cloud microphysics based on the prediction of bulk ice particle properties. Part I: Scheme description and idealized tests”. In: *Journal of the Atmospheric Sciences* 72.1, pp. 287–311.
- Mossop, S. (1976). “Production of secondary ice particles during the growth of graupel by riming”. In: *Quarterly Journal of the Royal Meteorological Society* 102.431, pp. 45–57.
- Mülmenstädt, J. et al. (2015). “Frequency of occurrence of rain from liquid-, mixed-, and ice-phase clouds derived from A-Train satellite retrievals”. In: *Geophysical Research Letters* 42.15, pp. 6502–6509.
- Musil, D. J. (1970). “Computer modeling of hailstone growth in feeder clouds”. In: *Journal of the Atmospheric Sciences* 27.3, pp. 474–482.
- Peichang, Z. and D. T. Du Bingyu (2001). *Radar Meteorology*.
- Petty, G. W. and W. Huang (2011). “The modified gamma size distribution applied to inhomogeneous and nonspherical particles: Key relationships and conversions”. In: *Journal of the Atmospheric Sciences* 68.7, pp. 1460–1473.
- Pfizenmaier, L. et al. (2017). “Retrieving Fall Streaks within Cloud Systems Using Doppler Radar”. In: *Journal of Atmospheric and Oceanic Technology* 34.4, pp. 905–920.
- Pfizenmaier, L. et al. (2018). “Observing ice particle growth along fall streaks in mixed-phase clouds using spectral polarimetric radar data”. In: *Atmospheric Chemistry and Physics Discussions* 2018, pp. 1–31. DOI: 10.5194/acp-2017-1032. URL: <https://www.atmos-chem-phys-discuss.net/acp-2017-1032/>.
- Pinsky, M. and A. Khain (1998). “Some effects of cloud turbulence on water–ice and ice–ice collisions”. In: *Atmospheric research* 47, pp. 69–86.
- Pruppacher, H. R. et al. (1998). *Microphysics of clouds and precipitation*.
- Roeckner, E. et al. (2003). “The atmospheric general circulation model ECHAM 5. PART I: Model description”. In:
- Ryzhkov, A. et al. (2016). “Quasi-vertical profiles—A new way to look at polarimetric radar data”. In: *Journal of Atmospheric and Oceanic Technology* 33.3, pp. 551–562.
- Seifert, A. and K. D. Beheng (2006a). “A two-moment cloud microphysics parameterization for mixed-phase clouds. Part 1: Model description”. In: *Meteorology and atmospheric physics* 92.1, pp. 45–66.
- (2001). “A double-moment parameterization for simulating autoconversion, accretion and selfcollection”. In: *Atmospheric research* 59, pp. 265–281.
- Stephens, G. L. (1994). *Remote sensing of the lower atmosphere*. Vol. 1994. Oxford University Press New York.
- Tyynelä, J. et al. (2011). “Radar backscattering from snowflakes: Comparison of fractal, aggregate, and soft spheroid models”. In: *Journal of Atmospheric and Oceanic Technology* 28.11, pp. 1365–1372.
- Zängl, G. et al. (2015). “The ICON (ICOsahedral Non-hydrostatic) modelling framework of DWD and MPI-M: Description of the non-hydrostatic dynamical core”. In: *Quarterly Journal of the Royal Meteorological Society* 141.687, pp. 563–579.
- Zeng, Y. et al. (2016). “An efficient modular volume-scanning radar forward operator for NWP models: description and coupling to the COSMO model”. In: *Quarterly Journal of the Royal Meteorological Society* 142.701, pp. 3234–3256.

# A. Appendix

## A.1. PAMTRA input variables

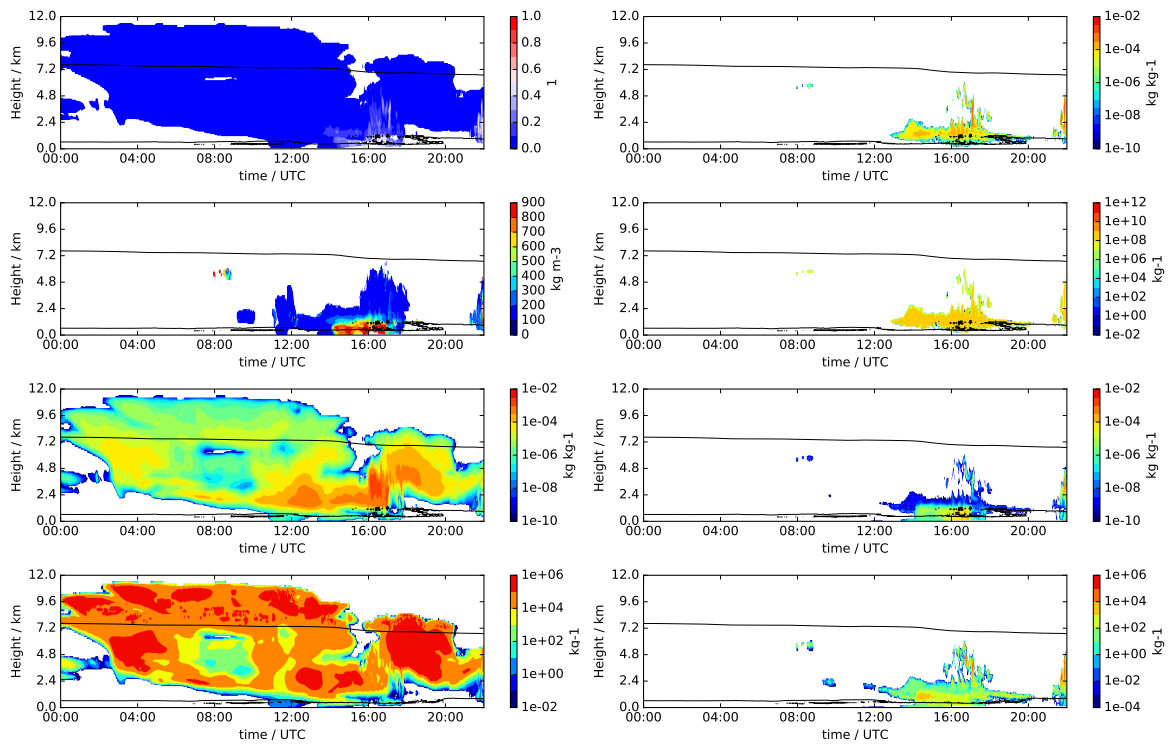
### A.1.1. 24th November 2015



(a) Cold phase variables:  $F_{rim}$ ,  $\rho_{rim}$ ,  $q_i$  and  $N_i$  (from top to bottom)      (b) Warm phase variables:  $q_c$ ,  $q_{nc}$ ,  $q_r$  and  $q_{nr}$  (from top to bottom)

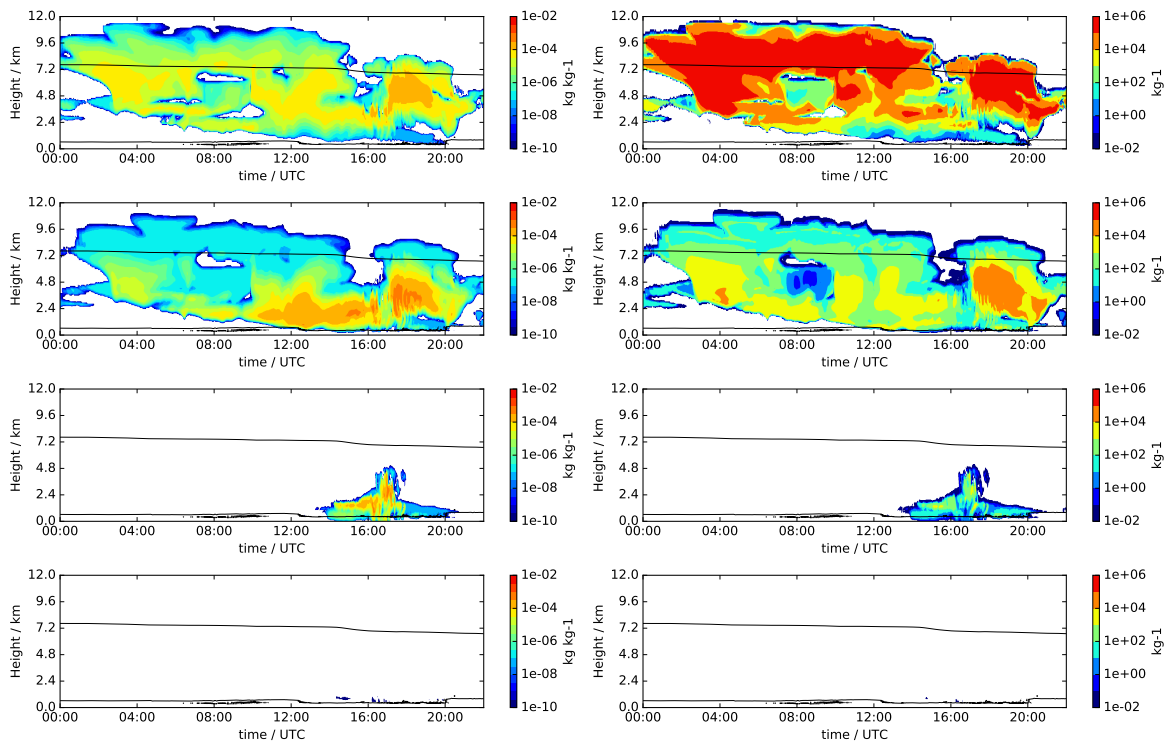
Figure A.1.: Prognostic variables of the *Nov. P3 control* run and variables calculated from them, which are relevant for the PAMTRA run for the November case.

## A. Appendix

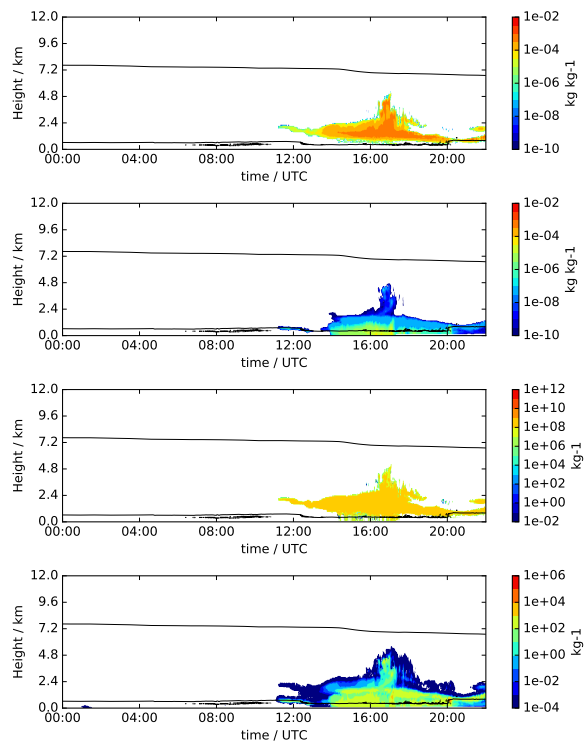


(a) Cold phase variables:  $F_{rim}$ ,  $\rho_{rim}$ ,  $q_i$  and  $N_i$  (from top to bottom) (b) Warm phase variables:  $q_c$ ,  $q_{nc}$ ,  $q_r$  and  $q_{nr}$  (from top to bottom)

Figure A.2.: Prognostic variables of the *Nov. P3 satad* run and variables calculated from them, which are relevant for the PAMTRA run for the November case.



(a)  $q$  of cloud ice, snow, graupel and hail (from top to bottom) (b)  $N$  of cloud ice, snow, graupel and hail (from top to bottom)



(c) From top to bottom:  $q$  of cloud water and rain,  $N$  of cloud water and rain

Figure A.3.: Prognostic variables of the SB-scheme for the November case.

## A.2. Inhomogeneities in the hydrometeor fields

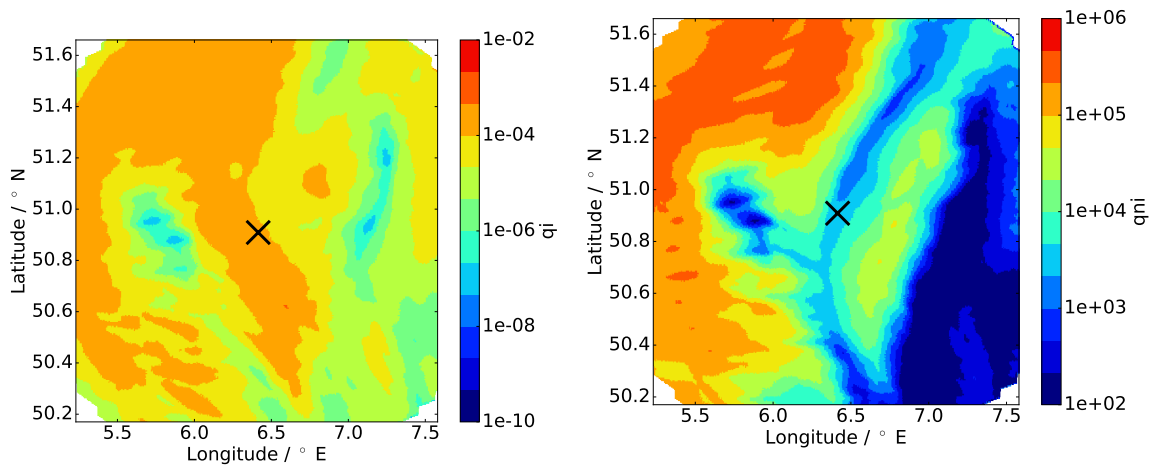


Figure A.4.: Vertical slice of the three-dimensional field of  $q_i$  (left) and  $N_i$  (right) of the *Nov. P3 control run DOM1* at a height of 2470 m at 11:30 UTC

## A.3. Contribution of the unrimed SB ice categories to $Z_e$ in the November case

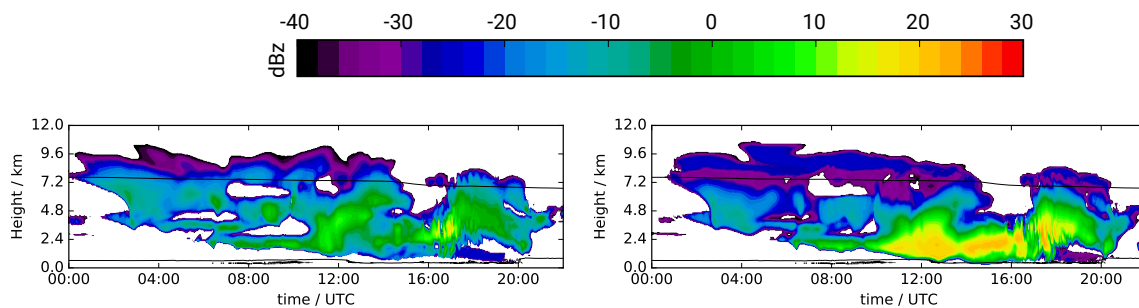
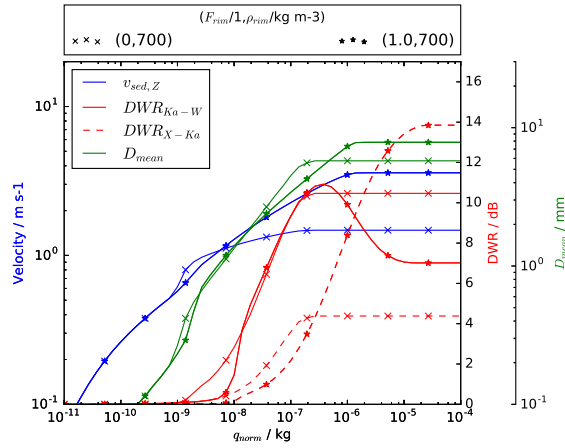
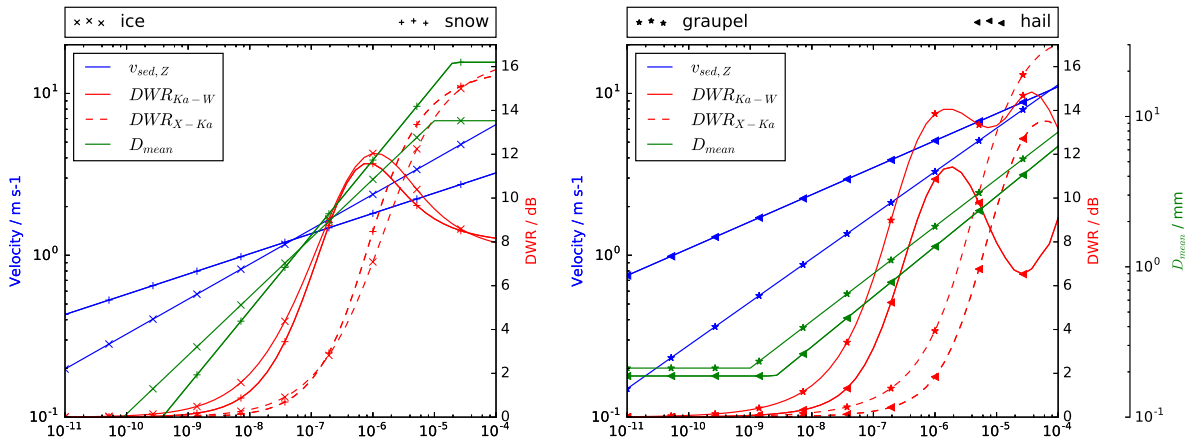


Figure A.5.: Contribution to  $Z_e$  by the SB ice category (left) and the SB snow category (right) in the November case

### A.4. $v_{sed,Z}$ , $D_{mean}$ and DWR as a function of the normalized mixing ratio $q_{norm}$



(a) P3 ice category



(b) SB unrimed categories

(c) SB rimed categories

Figure A.6.: Reflectivity weighted sedimentation velocity  $v_{sed,Z}$  (blue), mean diameter  $D_{mean}$  (green) and the dual-wavelength ratio between X- and Ka-Band ( $DWR_{X-Ka}$ ; red dashed) as well as between Ka- and W-Band ( $DWR_{Ka-W}$ ; red solid) as a function of the normalized mixing ratio  $q_{norm}$ .

## A.5. List of Symbols and Acronyms

Table A.1.: List of Symbols

symbol	description
$\alpha$	parameter of the area-diameter (A-D) relationship (P3)
$\beta$	parameter of the area-diameter (A-D) relationship (P3)
$\beta_{fit}$	fit parameter to the power spectra of the internal structure of aggregates (within the SSRG-theory)
$\gamma_{fit}$	fit parameter to the power spectra of the internal structure of aggregates (within the SSRG-theory)
$\gamma$	size distribution parameter in a four parameter gamma distribution
$\zeta$	vertical vorticity component
$\Theta_v$	virtual potential temperature
$\kappa_{fit}$	kurtosis parameter of the experimentally derived $A(s)$ function for an ensemble of aggregates (within the SSRG-theory)
$\lambda$	slope parameter of the gamma-distribution
$\lambda_c$	slope parameter of the gamma-distribution for the cloud droplet category (P3)
$\lambda_i$	slope parameter of the gamma-distribution for the ice category (P3)
$\lambda_r$	slope parameter of the gamma-distribution for the rain drop category (P3)
$\lambda_w$	wavelength of the radar beam
$\mu$	shape parameter of the gamma-distribution
$\mu_c$	shape parameter of the gamma-distribution for the cloud droplet category (P3)
$\mu_i$	shape parameter of the gamma-distribution for the ice category (P3)
$\mu_r$	shape parameter of the gamma-distribution for the rain drop category (P3)
$\Pi$	Exner function
$\rho_i$	bulk ice density
$\rho_d$	density of the unrimed part of the particle (P3)
$\rho_g$	graupel density (P3)
$\rho_{rim}$	rime density (P3)
$\rho_w$	water density
$\sigma_b$	backscatter cross section
$\overline{\sigma_b}$	mean backscatter cross section of an ensemble of particle
$A$	projected area of a particle
$A(s)$	area of a particle at the range $s$
$a_{mD}$	parameter in mass-diameter (m-D) relationship (P3)
$b_{mD}$	parameter in mass-diameter (m-D) relationship (P3)
$B_{rim}$	(bulk) rime volume (P3)
$c_{pd}$	specific heat capacity of dry air at constant pressure
$c_{vd}$	specific heat capacity of dry air at constant volume

$C$	capacitance of an ice particle
$C_{rad}$	radar constant
$D$	maximum particle dimension
$D_{mean}$	mean diameter of a size distribution
$D_{crit}$	threshold separating different $m$ - $D$ relationship regions (P3)
$DWR$	dual wavelength ratio
$E_i$	sticking efficiency
$E_c$	collision efficiency
$f$	Coriolis parameter
$f(D)$	size distribution
$F_{rim}$	(bulk) rime fraction (P3)
$F(v_n)$	source term for horizontal momentum
$g$	gravitational acceleration
$G$	Gibbs free energy
$G_i$	factor in growth law taking state of surrounding atmosphere into account
$IWC$	ice water content
$k$	wavenumber
$K(i, j)$	collection kernels
$K_h$	horizontal part of the kinetic energy
$K_w$	dielectric factor of water
$LWC$	liquid water content
$m$	mass of an individual particle
$m_{refr}$	refractive index
$M(D)$	mass concentration
$M(k)$	$k$ -th moment of the size distribution
$N_0$	intercept parameter of the gamma-distribution (P3)
$N(D)$	number distribution
$N$	number concentration
$nisub$	reduction of the number concentration through sublimation (P3)
$nimlt$	reduction of the number concentration through melting (P3)
$N_c$	total number concentration of the cloud droplet category (P3 and SB)
$N_i$	total number concentration of the ice category (P3 and SB)
$N_r$	total number concentration of the rain drop category (P3 and SB)
$N_g$	total number concentration of the graupel category (SB)
$N_h$	total number concentration of the hail category (SB)
$N_s$	total number concentration of the snow category (SB)
$P_r$	Backscattered power detected by the radar antenna
$p$	air pressure
$Q$	diabatic heat source terms
$q$	mixing ratio
$qccol$	increase in the mixing ratio through the collection of cloud droplets (P3)
$qrcol$	increase in the mixing ratio through the collection of rain drops (P3)

$qchetc$	increase in the mixing ratio through immersion freezing of cloud droplets (P3)
$qchetr$	increase in the mixing ratio through immersion freezing of rain drops (P3)
$qidep$	increase in the mixing ratio through depositional growth (P3)
$qinuc$	increase in the mixing ratio through deposition and condensation freezing (P3)
$qisub$	reduction in the mixing ratio through sublimation (P3)
$qimelt$	reduction in the mixing ratio through melting (P3)
$q_c$	mixing ratio of the cloud droplet category (P3 and SB)
$q_r$	mixing ratio of the rain drop category (P3 and SB)
$q_i$	mixing ratio of the ice category (P3 and SB)
$q_{rim}$	rime mass mixing ratio (P3)
$q_g$	mixing ratio of the graupel category (SB)
$q_h$	mixing ratio of the hail category (SB)
$q_s$	mixing ratio of the snow category (SB)
$q_{norm}$	normalized mixing ratio
$q_{norm,i}$	normalized mixing ratio of the ice category
$q_{norm,s}$	normalized mixing ratio of the snow category
$RR$	rain rate
$R_d$	gas constant of dry air
$s_i$	supersaturation over ice
$T$	air temperature
$V$	Volume of solid ice of the aggregate (within the SSRG-theory)
$V_k$	$k$ -th moment weighted fall speed
$v_{doppler}$	Doppler velocity
$v_n$	horizontal wind speed normal to the triangle edge
$v_{sed,N}$	mean number weighted sedimentation velocity
$v_{sed,m}$	mean mass weighted sedimentation velocity
$v_{sed,Z}$	mean reflectivity weighted sedimentation velocity
$v_t$	horizontal wind speed tangential to the triangle edge
$ZDR$	differential reflectivity
$Z_e$	radar reflectivity
$x$	size parameter
$x_i$	prognostic variables within ICON

---

Table A.2.: List of Acronyms

acronym	description
CFAD	Contoured Frequency by Altitude Diagram
COSMO	Consortium for Small-scale Modeling
DWD	German Weather Service
DWR	Dual wavelength ratio
EarthCARE	Earth Clouds, Aerosols and Radiation Explorer
ECHAM	European Centre for Medium-Range Weather Forecasts - Hamburg
ECMWF	European Centre for Medium-Range Weather Forecasts
EMVORADO	Efficient Modular Volume RADar Operator
HD(CP) <sup>2</sup>	High Definition Clouds and Precipitation for advancing Climate Prediction
ICON	ICOsahedral Nonhydrostatic model
ICON-LEM	ICON large eddy mode
ICON-NWP	ICON numerical weather prediction
IFS	Integrated Forecasting System
IN	ice nuclei
LEM	large eddy mode
LES	large eddy simulations
MPI-M	Max Planck Institute for Meteorology
NWP	numerical weather prediction
P3	Predicted particle properties
PAMTRA	Passive and Active Microwave TRAnsfer model
RADAR	RAdio Detection And Ranging
RADOLAN	radar online calibration
SB	Seifert and Beheng
SCE	stochastic collection equation
SLEVE	Smooth LEvel VERTical
TRIPEX	TRIPLE-frequency and Polarimetric radar Experiment for improving process observation of winter precipitation
TROPOS	Leibniz-Institute for Tropospheric Research

## Acknowledgements

At first, I want to thank Corinna Hoose for not only providing this exciting topic, but also for the passionate and professional mentoring during the last years including my Bachelor's thesis, a student assistant job and this Master's thesis. I also appreciate the opportunities she gave me to gain insights into the scientific community, by letting me participate in several interesting workshops and meetings. Thanks to the whole HD(CP)<sup>2</sup> community and especially the S1-group for welcoming me during those meetings. Also many thanks to Aiko Voigt for accepting the co-supervision of this thesis, his interest in this work and the helpful suggestions.

Thanks to Juha Tonttila for the help with ICON and P3, even from the deep north. I want to express my deepest thanks to Andrew Barrett for spending a lot of time reading my thesis draft and sharing his scientific and writing expertise. Thanks to the whole working group for welcoming me and providing a nice atmosphere.

Special thanks go also to Stefan Kneifel, Davide Ori and Mario Mech for introducing me to PAMTRA and the many helpful suggestions they gave me in a lot of aspects of this thesis during the whole year. Thanks to Vera Schemann for the extensive help to set up the November case. She made me aware of a lot of details and the importance of setting up a model run carefully. Thanks, José Dias Neto, for providing and explaining the radar data. Those five colleagues from Cologne made a great contribution to this work.

I also want to thank Akio Hansen, for the advice to use PAMTRA and providing the script for running PAMTRA with the model output of ICON with the SB-scheme.

Most cordial thanks to my friends, fellow students and my family for always being there for me. A very special thanks to my parents for all the support and believing in me, without them all that would not have been possible. Last but not least, warm thanks to Corinna Kipke, for all her love and support.